

Nanoindentation of Gold Single Crystals

Martha Mary McCann



Virginia Polytechnic Institute and State University

**Doctor of Philosophy
Materials Science and Engineering**

Chair: Dr. Sean G. Corcoran

Dr. Alex O. Aning

Dr. Diana Farkas

Dr. Stephen L. Kampe

Dr. William T. Reynolds

March 29, 2004

Blacksburg, Virginia

Keywords: Nanoindentation, Gold, Hardness Variability, Yield Variability, Surface Structure, Electrochemical Modification

© 2004 by Martha M. McCann

Nanoindentation of Gold Single Crystals

Martha M. McCann

ABSTRACT

Nanoindentation is an increasingly used tool to investigate the mechanical properties of very small volumes of material. Gold single crystals were chosen as a model system for surface modification studies, because of the electrochemical advantages and the simple structure of the material. Experiments on these samples displayed a spectrum of residual deformation, with measured hardness values on the same surface differing by over a factor of two. The yield point also exhibited considerable variation, but the depth of penetration was independent of this elastic-plastic transition. The onset of plastic deformation in these tests is observed at stress levels on the order of the theoretical yield strength. There are a limited number of defects in a single crystal specimen of gold, especially on the length scale required to influence nearly every indentation experiment. A test matrix was designed to change the concentrations of possible defects in a sample (dislocations, vacancies, and structural features), by altering some of the surface preparation parameters. The results of these experiments were extremely consistent. Observed trends within the matrix, combined with the observations of reduced hardness and earlier plasticity when compared to the preliminary testing, indicate a decline in the structural continuity of the sample. This is surprising considering the extensive material removal and thermal history of some of these surfaces. There is no indication of a cause for the dramatic inconsistencies in mechanical properties observed in preliminary testing, but a consistent surface enables the study of intentional modifications. Changes in contact area that were undetectable in preliminary results now demonstrate predictable shifts in hardness values. The deposition of a single monolayer of gold oxide raised the average load at yield by a factor of three and increased the hardness by over 26%. Attributing this change to the oxide is corroborated by the reduction of hardness when the oxide is stripped. Similar behavior is observed when a lead monolayer is deposited and tested ex-situ. It is surprising that layers <0.5 nm in thickness would have such a dramatic influence on indentation tests at least 35 nm deep. This indicates that no surface layer can be ignored at this scale. These experiments demonstrate that there is still much to be learned about nanoscale deformation mechanisms.

TABLE OF CONTENTS

ABSTRACT	<i>ii</i>
ACKNOWLEDGEMENTS	<i>v</i>
LIST OF FIGURES	<i>vii</i>
LIST OF TABLES	<i>xvi</i>
SYMBOLS AND ACRONYMS	<i>xvii</i>
CHAPTER 1: INTRODUCTION	1
CHAPTER 2: BACKGROUND INFORMATION	4
2.1 Nanoindentation	4
2.1.1 Contact Mechanics	5
2.1.2 Depth Sensing Indentation	13
2.1.3 Instrumentation	19
2.1.3a Hysitron	19
2.1.3 b Tips	22
2.2 Potential sources of data distortion	26
2.2.1 Contact Area Changes	26
2.2.1a Pile-up and Sink-in	27
2.2.1b Roughness	29
2.2.1c Adhesion	31
2.2.2 Time Dependent Properties	34
2.2.2 a Creep	34
2.2.2 b Time dependent plasticity	34
2.2.2 c Impact Velocity	36
2.3 Related Research	37
2.3.1 Gold Indentation	37
2.3.2 Gold Electrochemistry	43
2.3.2 a Gold Oxidation	43
2.3.2 b Under-potential deposition	45

CHAPTER 3: EXPERIMENTAL	50
3.1 Surface Preparation	50
3.2 Nanoindentation	53
3.3 Electrochemistry	53
CHAPTER 4: RESULTS AND DISCUSSION	55
4.1 Initial Testing	55
4.1.1 Preliminary Results	55
4.1.2 Potential Defects	65
4.1.2 a Dislocations	65
4.1.2 b Surface Structure	67
4.1.2 c Vacancies	67
4.1.2 d Impurities	69
4.2 Test Matrix	71
4.2.1 Test Matrix Definition	71
4.2.2 Experimental Results	75
4.3 Influence of Surface Inconsistencies	88
4.3.1 Surface Structure	88
4.3.2 Surface Scratching	93
4.4 Ex-Situ Electrochemical Modification	101
4.4.1 Air Exposure	101
4.4.2 Indentation of Gold-Oxide	104
4.4.3 Indentation of Lead UPD Layer	110
CHAPTER 5: SUMMARY AND CONCLUSIONS	116
REFERENCES	122
VITA	126

ACKNOWLEDGEMENTS

I would like to thank my advisor Sean G. Corcoran for all his support over the years. He has been an incredible intellectual resource. I would like to acknowledge my committee members for their time and helpful discussions. I would especially like to recognize Dr. Bill Reynolds for all the work he does as an instructor, an advisor and graduate program coordinator. The Materials Science Department has been a wonderful place to call home. This is due in part to the tremendous contributions of two individuals who have made my time here run much more smoothly. Dave Berry has been a tremendous resource for equipment and practical knowledge; thank you Dave for all of your help. Susette Sowers has been of great help as office administrator and graduate program assistant, but more importantly she has been a great friend; thank you Susette for all your support.

I also need to acknowledge my fellow graduate students for lending their expertise. Thanks to Doug Crowson for his countless hours of help on the Hysitron and my golf game. Thanks to Todd Heil for his sharing of his TEM experience, it is a shame we couldn't have gotten further. Thanks to Feming Bai for sharing your lab and running some x-ray diffraction on my samples.

I would like to thank my parents Mary and John McCann, for their constant guidance and support. As a young child they provided a home that was ever vigilant to the wonders of science and nature around us. As an adult, they have been an incredible technical and philosophical resource. My mother's patience with my spelling and grammar has been commendable. The reader of this work probably appreciates my father's constant battle for clarity and succinctness. I thank my grandmother Gertrude McCann for keeping me on the straight and narrow my whole life. I especially appreciate the decades of the Rosary, dedicated to help me persevere in these last few months. Special thanks go to my sister Sarah Herlihey and her family Jay, Linda and Jake. They have brought so much joy to my life and have always given me such understanding and loving support. I also need to thank my future in-laws Floyd, Ann, Nonni, Garrett, Dean, and Carrie. I am very lucky to be marrying into a family so full of love; their blessing over the past few years has been a wonderful gift. This brings me to my fiancé Brad. He sacrificed a great deal to join me in Virginia. His loving support and care have made it all possible. Blacksburg will always be a special place in our hearts because it has been such a special time in our relationship. I do not know if I can articulate the importance of my relationship with my best friend Karen Ryan. She has helped to keep me sane when all others had lost all hope. She has been a sounding board when I need it most. She has reminded me of who I am when I no longer remember. She has been the definition of a true friend.

Numerous other friends and family have helped along the way. There have been so many individuals that through their friendship have made this experience so wonderful. To Dan Esterly, Doug Crowson, Jaquie Burks, Marybeth Miceli, Emmett O'Brian, Derek Klindinst, Kelly Hales, Amanda and Jason Jones, R. Lee Williams and wife Sita, thank you for being such amazing people and wonderful friends. A special thanks to Erik Scribber for his open door and powerful gadgets; I would have been lost

without my karmic reward. Thanks to Derek Klindinst and the rest of the poker enthusiasts for distracting my fiancé at least once a week. Thanks to Amanda Harris Jones for taking me in out of the cold when I needed a new home. Thank you to my tailgating friends for making Saturday a day of fun. Thanks to Tara Eskalome and Andrea Larocce for allowing us to share a little bit of the back woods with them. Thanks Shayn Pierce for showing me the way it's done. Thanks to everyone who has made this journey unforgettable.

LIST OF FIGURES

- Figure 2- 1 Schematic of the interaction between a rigid spherical indenter (with radius = R) and a flat surface. The radius of contact (a) is also indicated. The total displacement of the surface is h_t , which consists of the distance from the free surface to the radius of contact (h_e), and the distance from the radius of contact to the total depth (h_p). Page 5
- Figure 2- 2 Schematic of contact between a conical indenter (with half angle α) and a flat surface. The radius of contact (a) is also indicated. The total displacement of the surface is h_t , which consists of the distance from the free surface to the radius of contact (h_e), and the distance from the radius of contact to the total depth (h_p). Page 9
- Figure 2- 3 Schematic of the theoretical shear stress, the force required to slide one row of atoms over another, to a location of perfect registry. Page 10
- Figure 2- 4 Schematic of the expanding cavity model. The contacting area between the sample and indenter is the hydrostatic core of radius a_c . The core is surrounded by a plastic zone of radius c , which is constrained by a region of elastic deformation. As the tip is further indexed into the surface (dh), the core grows in size (da), by the radial movement of material ($du(r)$) to accommodate the added volume, also increasing the plastic zone (dc). Page 12
- Figure 2- 5 a) Loading profile for typical indentation test. The transducer drift is observed in the first 5 seconds, followed by loading from 5 to 20 seconds, then a hold at maximum load for 10 seconds, and finally gradual unloading over the final 15 seconds of the experiment. b) Load-displacement curve on mechanically polished gold, subjected to testing profile in (a). (Initial drift check not pictured) Page 14
- Figure 2- 6 Representative load-displacement data demonstrating differences in elasticity a) Completely elastic material b) elastoplastic material c) ideally plastic material. Page 15
- Figure 2-7 a) Schematic of an indenter at maximum load (P_{max}), with an associated total depth of h_{max} . The contact between the indenter and the surface at maximum load is defined by depth h_c , with a corresponding projected area of contact A_c . The sample profile after the load has been removed is indicated by the dashed line, with a final depth of h_f . b) Corresponding load-displacement curve, indicating the final depth (h_f), the intercept depth (h_i), the contact depth (h_c), and the maximum depth. The slope of the tangent at maximum load is the dashed line. The stiffness (S) is the slope of this line. Page 18

Figure 2-8	Schematic of the indentation system which consists of two instruments, the Triboscope and a Scanning Probe Microscope (SPM). The SPM contributes the imaging software and displacement control. The indentation system consists of the transducer, controller, and a separate data acquisition system.	Page 20
Figure 2-9	Schematic of a three plate capacitor force-displacement transducer of the Hysitron Triboscope. Voltage applied to the drive plates creates an electrostatic force with the pick-up electrode. The displacement is monitored by changes in capacitance.	Page 21
Figure 2-10	Schematics of a Berkovich indenter with dimensions a) Top view b) Cross Section c) Equations for dimensions of tip indicated in schematics.	Page 23
Figure 2-11	a) Indentation tests on fused silica, done at numerous loads on different days of testing. b) Surface image of fused quartz, done by indentation probe after testing, showing indents of a variety of sizes. Tests like these are used to create a tip area function.	Page 24
Figure 2-12	Plot of the calculated projected area of contact as a function of penetration depth of the Berkovich indenter used for experimentation. The curve fit is the projected area of contact as a function of contact depth.	Page 25
Figure 2-13	Indentation contact profiles for a material that a) experience pile-up around the indenter, increasing contact area from the calculated value. b) experience sink-in or reduced contact area.	Page 28
Figure 2-14	Schematic of the non-uniform contact between a indentation tip and a rough surface. The over estimate in contact area compared to that assumed based on displacement will lead to increased localized stress, generating greater deformation, resulting in an underestimate of hardness.	Page 29
Figure 2-15	Load displacement curve demonstrating adhesion between the probe tip and the sample, evident by the large negative load required to separate them.	Page 31
Figure 2-16	Schematic of the contact between two elastic solids with an external load P . The Hertzian contact model predicts a radius of contact a_0 , with a pressure distribution of p . The addition of adhesion between the two bodies in the JKR model will increase the contact radius to a_1 . The apparent pressure distribution p_1 is the combination of the contact pressure (p) and the adhesion pressure (p_A).	Page 32

- Figure 2-17 Load-displacement data for a tungsten probe on a gold (111) surface. In gold displacement jumps indicate the onset of plastic deformation. These indentation tests show a wide variety of yield behavior. One of the indents deforms elastically, never experiencing a yield point. One of the indentation tests yields during the loading portion of the test, another during the hold at maximum load, and another during the unloading of the surface. This demonstrates that the onset of plastic deformation can be time dependent in the appropriate load range. Page 36
- Figure 2-18 a) Load-displacement data on gold surface, exhibiting elastic deformation indicated by the unloading tracing the loading curve. b) Image taken after indentation test pictured in (a). No residual deformation confirms that the displacement was elastic in nature. c) Load-displacement data on same gold surface. Higher load has initiated plastic deformation, initially indicated by a jump in displacement. d) Image taken after indentation test pictured in (c), confirming plastic deformation. Page 38
- Figure 2-19 Cyclic Voltammogram of gold (111) surface in 0.1M HClO₄, scanned from -0.4 to 1.05 V versus a platinum wire counter electrode. The peaks at positive current densities correspond to the deposition of a lead oxide, while the peak at negative current densities corresponds to the stripping of the induced oxide. The hysteresis in voltage is due to the turnover of the MOH dipoles. Page 45
- Figure 2-20 Cyclic Voltammogram of a gold (111) working electrode in a 1.0 mM Pb (ClO₄) + 0.1 M HClO₄ electrolyte, scanned from 0.01 V to 1.85 V vs. a platinum wire counter electrode. Bulk deposition is indicated by the line at zero volts. The peaks at potentials above this line indicate the deposition and stripping of a lead monolayer on the surface. Page 46
- Figure 3-1 Specialized polishing fixture used to maintain crystal orientation. The fixture has tungsten carbide feet to resist wear and maintain a planar surface and a micrometer at the top to monitor the amount of material removed. Page 50
- Figure 3-2 Surface images taken with STM at various stages of surface preparation, all 1 μm x 1 μm. a) Surface that has been polished with 0.5 μm alumina paste b) Surface that has been mechanically polished and electropolished for approximately 45 seconds c) Surface that has been mechanically polished, electropolished and flame annealed for 15 minutes. Page 51
- Figure 3-3 Annealing profile used to reduce the vacancy concentration in the gold single crystal. Anneal was performed in a furnace purged with Argon. The total duration of anneal is 63 hours. Page 52

- Figure 3-4 Electrochemical cell developed for use with Digital Instruments Electrochemical STM. The exposed area is 0.59 mm. The gold crystal is the working electrode, reference electrode is a lead wire and the counter is a platinum wire. The screws hold the electrodes in place and are the leads to connect to the potentiostat. The base of the cell measures approximately 20 mm. Page 54
- Figure 4-1 a) Four load-displacement curves done by a diamond Berkovich indenter on fused quartz taken on two different days, demonstrating the consistency that is anticipated in this form of material testing. b) Four load-displacement curves done by a tungsten tip on the same gold (111) surface under identical conditions, demonstrating considerable variability in the mechanical behavior on what should be a consistent surface. Page 55
- Figure 4-2 Scanning Tunneling Micrograph of a gold (111) surface. The x and y-axis are 2 μm . The total height pictured is 30 nm. Each of the step bunches is approximately 5 nm in height. Page 57
- Figure 4-3 Load-displacement data for a tungsten tip on a gold (111) surface. This demonstrates the tremendous variation measured on a single surface in one day of testing. The final displacement does not seem to correlate to the yield point, surface structure, or extent of creep at hold. Page 58
- Figure 4-4 Load-displacement data for a diamond Berkovich indenter on a gold (111) surface. This demonstrates the tremendous variation measured on a single surface in one day of testing. The final displacement does not seem to correlate to the yield point, surface structure, or extent of creep at hold. Page 60
- Figure 4-5 Load-displacement data demonstrating that the yield load does not correlate to final depth a) two indents with very similar loads at yield with very different depths of penetration b) two indents with very similar depths of penetration that have very different yield points. Page 61
- Figure 4-6 Comparing the two extremes in measured hardness pictured in Figure 4-4. a) Image of the gold surface before indentation test A. b) Image of the gold surface before indentation test L. c) Image of the gold surface after indentation test A. d) Image of the gold surface after indentation test L. e) Cross section of before picture with area of indent A approximated by arrows. f) Cross section of before picture with area of indent L approximated by arrows. g.) Load-displacement data for two pictured indents. Despite their drastically different hardness results, the two surfaces look relatively similar. Page 62
- Figure 4-7 Comparison of indentation tests E, F, and G pictured in Figure 4-4, which display very consistent results. a) Image of the gold surface before indentation test E. b) Image of the gold surface Page 63

before indentation test F. c) Image of the gold surface before indentation test G. d) Image of the gold surface after indentation test E. e) Image of the gold surface after indentation test F. f) Image of the gold surface after indentation test G, with some evidence of slight surface scratching. g) Cross section of before picture with area of indent E approximated by arrows. h) Cross section of before picture with area of Indent F approximated by arrows. i) Cross section of before picture with area of indent G approximated by arrows. j.) Load-displacement data for indents E, F, and G. Indent E is on a step which tends to make a material appear softer. Indent G shows evidence of scratching, which work hardens the surface, making it appear harder. Despite their drastically different surfaces, they result in very similar hardness.

- | | | |
|-------------|---|---------------------|
| Figure 4-8 | Histogram of all the measured hardness values for a diamond indenter on gold (111) surface. This shows no identifiable center to the population. The range for the hardness values is also extremely large for this method of testing. | Page 64 |
| Figure 4-9 | Plot of the resolved shear stress required to operate a Frank Read Source as a function of pin point separation. Resolved Shear Stresses observed in our experiments correlate to separations of 20 nm or less. | Page 66 |
| Figure 4-10 | Scanning Tunneling Micrograph of a gold (111) surface. The height of this image is 10nm, while the x and y-axes each measure 1 micron. The surface is covered with small steps, the result of insufficient flame annealing. | Page 72 |
| Figure 4-11 | Scanning Tunneling Micrograph of a gold (111) surface. The terraces are sufficiently large to place indents on, but show signs of scratches that remain from the mechanical polishing stage of sample preparation. The left image is a measure of the change in height across the imaged area. The image on the right is the change in current in the same region. Current images often highlight edges that are difficult to resolve in the height mode. | Page 73 |
| Figure 4-12 | Load-displacement data for each of the experiments defined by the test matrix. Five indents were selected for each testing condition based upon the images of the location to try and compare like surfaces. Selected indents were placed surfaces that were not scratched and involved the smallest steps possible. Average property values for the selected tests are also given. The selected properties are yield at load, maximum shear stress at the initiation of plasticity, maximum penetration depth and calculated hardness. | Page 76
-Page 78 |
| Figure 4-13 | Histogram showing the range of hardness values for each test in the matrix. These indents were selected as the 5 best under each set of conditions. This means the surfaces were not scratched and involved the smallest steps possible. | Page 78 |

- Figure 4-14 a) Representative surface images from Test 4 Surface b) Representative surface images from Test 5 surface. Test 4 Surface was the hardest of the 9, while Test 5 was the softest. The images on the left are height images with a z-axis of 70 nm in each. The images on the right are both current images. Page 80
- Figure 4-15 a) Representative surface images from Test 2 Surface b) Representative surface images from Test 3 surface. Test 2 Surface had the smallest standard deviation in measured hardness, while Test 3 had the largest. The images on the left are height images with a z axis of 200 nm for Test 2 surface and 20 nm for the Test 3 surface. The images on the right are both current images. Page 81
- Figure 4-16 Plots of the S/N as a function of factor level. a) Flame annealing the surface decreases variability with an increase in duration. b) The number of cycles of electropolishing and flame annealing prior to indentation testing does not have a linear relationship. Variability is increased by too little or too much electropolishing. c) Cooling rate of the crystal indicates that the largest variability occurred in the slowly cooled crystal. This may be explained by the fact that these are the only crystals that do not experience cleaning just prior to testing. Page 83
- Figure 4-17 Plots of Factor interactions a) The interaction of flame annealing and the cooling rate. b) The interaction of the number of cycles and the cooling rate. c) The interaction of the flame annealing duration and the number of cycles. Interaction plots of three level factors are very difficult to interpret, but can indicate directions for future studies. None of these interactions are significant enough to merit further investigation. Page 85
- Figure 4-18 Histogram of hardness values for all indents done on nine surfaces in test matrix. There are some slight shifts in average hardness with in a test. Some testing conditions demonstrate broader population distributions, but over all the test matrix surfaces behave in a very consistent manner. When combined the test matrix results demonstrate a normal population distribution. Page 86
- Figure 4-19 Histogram of the preliminary data plotted with that of the total test matrix (all nine surface preparations). The test matrix data has a bell shaped distribution over a smaller range compared to the scattered distribution of the preliminary tests. Page 87
- Figure 4-20 Comparison of two indents done on the same testing surface, one on a flat terrace, the second on the bottom side of a step bunch. a) Surface image before indentation test on flat surface. b) Surface image of step bunch before indent. c) Surface image post indent on flat surface. d) Surface image of surface post indent on step bunch. e) Image cross section of flat surface, area of indent defined by arrows. f) Image cross section of flat surface, area of indent defined by arrows. g) Image cross section measuring step height, Page 89

dimensions of which are given in the legend. h) Load-Displacement data for two indents pictured. The increase in contact area due to the step decreases the force per unit area, resulting in a calculated increased hardness compared to the test done on a flat surface.

- Figure 4-21 Comparison of two indents done on the same testing surface, one on a flat terrace, the second on the high side of a step bunch. a) Surface image before indentation test on flat surface. b) Surface image of step bunch before indent. c) Surface image post indent on flat surface. d) Surface image of surface post indent on step bunch. e) Image cross section of flat surface, area of indent defined by arrows. f) Image cross section of stepped surface, area of indent defined by arrows. g) Image cross section measuring step height, the dimensions of which are given in the legend h) Load-Displacement data for two indents pictured. The decrease in contact area due to the step increases the force per unit area, resulting in a decreased calculated hardness compared to the test done on a flat surface. Page 90
- Figure 4-22 Histogram showing the influence of different ranges of step height on hardness measurements. Flat surfaces have a normal distribution. As the steps get larger they broaden the distribution. When the steps get large the distribution has no identifiable peak. Scratching in these experiments work hardened the surface, as demonstrated by the increase in hardness measurements. Page 92
- Figure 4-23 a) Load displacement data on a mechanically polished surface. The variability in response to applied load is caused by the fact that the roughness is a significant portion of the overall displacement. If the load is increased, the variability will be reduced if the depth is beyond the scale of the roughness (as shown by measurements on same surface in b). b) Load displacement data for three different crystals. Two of the crystals were mechanically polished prior to testing. The third sample is electropolished and flame annealed after the mechanical polishing. The mechanically polished surfaces have nearly twice the measured hardness compared to the electropolished and flame annealed sample. Page 94
- Figure 4-24 Surface image, $6\mu\text{m} \times 6\mu\text{m}$, taken by Berkovich indenter during nanoindentation testing. Previous images, $3\mu\text{m} \times 3\mu\text{m}$ in dimension, have caused surface damage due to a drift in applied imaging load. The scratching results in the destruction of small surface features such as step bunches, an increase in roughness, and piles of excess material at the edges of the imaged region. Page 95
- Figure 4-25 Load displacement data taken during preliminary testing with a sharp Berkovich indenter. The majority of the tests occurred on surfaces that had been roughened by scratching of the probe tip. One indent demonstrates significant elastic loading prior to deformation. The surface is most likely undamaged prior to Page 96

testing.

- Figure 4-26 Surface images taken by indenter probe a) before indent on undamaged surface b) before indent on scratched surface c) after indent on undamaged d) after indent on scratched surface e) surface height and current images after indentation of undamaged surface f) height and current images after indentation on scratched surface. Page 98
- Figure 4-27 Roughness determination from a) before image of unscratched surface b) before image of scratched surface c) after image of unscratched surface in zoom region d) after image of scratched surface in zoom region e) outside the zoom region on unscratched surface f) outside zoom region on scratched surface. Page 99
- Figure 4-28 a) Load-displacement data for surface preparation defined by test 5 from the test matrix b) Load-displacement data for the same surface after being exposed to the air for six days. c) Load displacement data for the same surface after it has been flame annealed (cleaned). The exposure to air significantly changes the initial yield strength of the sample. Page 102
- Figure 4-29 a) Histogram comparing the yield load of surfaces: Test 5 from the test matrix, the same surface after 6 days exposed to air, and the same surface with an additional 15 minute flame anneal to clean the surface. Air exposure increased the measured yield load of a surface. Page 104
- Figure 4-30 Freshly cleaned gold (111) surface: a) Image before indentation testing b) Image after indentation testing c) Load displacement data for pictured indents d) average important property values for indentation tests. Page 105
- Figure 4-31 Cyclic Voltamogram of oxide deposition on gold (111) surface in 1.0 mM Pb (ClO₄) + 0.1 M HClO₄. The voltage is cycled between 0.05 V and 1.80 V versus a platinum wire counter electrode. The cell is disconnected at a voltage of 1.75 V, leaving the oxide monolayer on the surface. Page 106
- Figure 4-32 Oxidized gold surface: a) Image before indentation testing b) Image after indentation testing c) Load displacement data for pictured indents d) average important property values for indentation tests. Page 107
- Figure 4-33 Gold (111) surface stripped of oxide: a) Image before indentation testing b) Image after indentation testing c) Load displacement data for pictured indents d) average important property values for indentation tests. Page 108
- Figure 4-34 a) Average indentation curve for plain gold surface, gold oxide surface, and plain gold surface after oxide stripped. b) Histogram Page 109

of hardness values measured under each of these conditions. c)
Histogram of yield loads measured under each of these conditions.

- Figure 4-35 Freshly cleaned gold (111) surface: a) Image before indentation testing b) Image after indentation testing c) Load displacement data for pictured indents d) average important property values for indentation tests. Page 110
- Figure 4-36 Cyclic Voltamogram of lead deposition on gold (111) surface in 1.0 mM Pb (ClO₄) + 0.1 M HClO₄. The voltage is cycled between 0.05 V and 1.75 V versus a platinum wire counter electrode. The cell is disconnected at a voltage of 0.05 V, leaving the lead monolayer on the surface. Page 111
- Figure 4-37 Gold surface with a monolayer of lead on the surface that has been oxidized: a) Image before indentation testing b) Image after indentation testing c) Load displacement data for pictured indents d) average important property values for indentation tests. Page 112
- Figure 4-38 a) Average indentation curve for plain gold surface, lead oxide surface. b) Histogram of hardness values measured under each of these conditions. c) Histogram of yield loads measured under each of these conditions. Page 113
- Figure 4-39 42 a) Average indentation curve for all electrochemical testing. b) Histogram of hardness values measured under each condition. c) Histogram of yield loads measured under each of these conditions. Page 114

LIST OF TABLES

Table 4-1	Important values for indentation tests shown in Figure 4-3. Yield load is the point at which plastic deformation begins, indicated by a displacement jump or change in loading slope. The maximum shear stress (τ_{\max}) is shear stress necessary to initiate plastic deformation at the location of the indent. It is calculated from the yield load. The maximum depth of penetration (h_{\max}) is the displacement at the end of the hold at maximum load. The maximum depth is used in hardness calculation. Due to the fact that this was a tungsten tip, we were unable to get an accurate tip area function and therefore have not reported hardness values.	Page 59
Table 4-2	Important values for the indentation tests shown in Figure 4-4. Yield load is the point at which plastic deformation begins, indicated by a displacement jump or change in loading slope. The maximum shear stress (τ_{\max}) is shear stress necessary to initiate plastic deformation at the location of the indent. It is calculated from the yield load. The maximum depth of penetration (h_{\max}) is the displacement at the end of the hold at maximum load. The maximum depth is used in hardness calculation. Hardness is a common property measurement used to compare materials resistance to deformation.	Page 60
Table 4-3	Taguchi L-9 Array for three parameters at three levels. The first parameter is the duration of flame annealing which was varied from 5 min to 25 minutes. The second factor was the number of times the crystal was electropolished and flame annealed before it was tested. This was varied from a single electropolish and flame anneal to eight such surface treatments prior to testing. The third parameter is the cooling rate which was varied from a rapid quench to a 63 hour stepped anneal.	Page 75
Table 4-4	Average values for the property measurements from the indentation tests shown in Figure 4-29	Page 103

SYMBOLS AND ACRONYMS

a	= radius of contact
α	= curve fitting parameter; semi-angle of conical indenter
A_c	= projected area of contact
a_c	= radius of hydrostatic core
Ag	= silver
a_o	= contact at zero load due to adhesion
a_{pb}	= activity of the bulk metal
$a_{pb^{2+}}$	= activity of the electrolyte
$A_{residual}$	= The residual impression
Au	= gold
b	= atom spacing in the direction of applied shear stress; length of face of Berkovich indenter
β	= Angle of inclination of the indenter with the specimen surface
C	= Constraint factor
c	= radius of plastic zone
C_o	= the initial vacancy concentration
C_m	= machine (load frame) compliance
$C_{Me^{n+}}$	= concentration of metal (Me)
C_t	= total compliance of the system
C_T	= the equilibrium or surface concentration at the annealing temperature
C_V	= the concentration of vacancies
d	= row spacing
D_o	= self-diffusion rate of gold
D_T	= diffusion rate of vacancies
ε	= constant based on indenter geometry
E^*	= Reduced Modulus
E_a	= metal interaction potential
E_i	= Young's Modulus of indenter material

E_m	= Young's Modulus of sample material
E_o	= standard Nernst reversible potential
E_r	= Reversible Nernst potential
F	= Faraday's constant
F_{applied}	= force applied
F_{el}	= electrostatic force
f_{Me}	= Activity coefficient of the monolayer
f_{Men^+}	= Activity coefficient of the metal ion
G	= Shear modulus
γ	= energy per unit of contact for two surfaces
h	= displacement; depth of Berkovich indenter
H	= Hardness
h_c	= contact depth
H_c	= contact hardness
h_e	= depth of circle of contact measured from the free surface
h_f	= final depth
H_f	= enthalpy of formation per mole of vacancy
h_i	= intercept depth
H_{macro}	= Harness on macroscopic scale
h_{max}	= maximum indentation depth
h_p	= depth of circle of contact measured from the maximum depth (plastic depth)
h_t	= total indentation depth measured from the free surface of the specimen
I	= indentation modulus
k_e	= electrostatic force constant
k_s	= spring force constant
l	= cross sectional distance from face to edge of Berkovich indenter
m	= curve fitting parameter
n	= number of data points in RMS calculation; valence state of the ion
n	= valence state of the ion

v_i	= Poisson ratio of the indenter material
v_m	= Poisson ratio of sample material
P	= load
p	= pressure within the hydrostatic core
P_1	= apparent load
p_a	= pressure distribution due to adhesion
P_a	= force due to adhesion
P_{applied}	= applied load
P_b	= lead
P_C	= pull off force
P_{max}	= maximum load
p_{mean}	= mean contact pressure
p_o	= normal pressure at the center of contact, also the maximum pressure in the case of a spherical indenter
P_o	= adhesive force at zero load
Θ	= fraction of coverage
Q	= the activation energy per mole of diffusing species
R	= Radius of Indenter; ideal gas constant
r	= radial distance from the center of symmetry
R_q	= roughness, the height distribution about the mean
S	= measured stiffness
s	= length from edge to edge of Berkovich indenter
σ_θ	= angular stress
σ_r	= stress in the radial direction
σ_z	= stress in the direction normal to contact
τ	= applied shear stress
T	= absolute temperature
t	= time in seconds
τ_{max}	= maximum shear stress
τ_{rz}	= shear stress
τ_{th}	= theoretical shear stress
U_E	= stored elastic energy

U_s	= loss in surface energy
V	= applied voltage
W	= tungsten
x	= shear translation of sliding atoms
Y	= Yield or Flow Stress
y	= mean height of the surface
y_i	= relative vertical heights
\bar{y}	= average value for relative height
z	= length from face to center of Berkovich indenter
AFM	= Atomic Force Microscopy
CG	= Conjugate Gradient
DSI	= Depth Sensing Indentation
EAM	= Embedded Atom Method
IFM	= Interfacial Force Microscopy
MD	= Molecular Dynamic
rms	= root mean square (roughness)
SEM	= Scanning Electron Microscopy
SPM	= Scanning Probe Microscopy
STM	= Scanning Tunneling Microscopy
TEM	= Transmission Electron Microscopy

CHAPTER 1: INTRODUCTION

In many aspects of technology, there is a drive for smaller and smaller components. As the volumes of material decrease, the response of the material to characterization techniques may be different from their bulk form. One explanation for the change in behavior is the increased role of the surface. On the macro-scale the surface is such a small portion of the overall subject, it is often ignored. When the volume is reduced sufficiently the surface becomes a large fraction of the overall quantity of material. Defects are another aspect of a material that is ignored at macro-scale, for properties are measured over large volumes of material, encompassing many defects and therefore are not sensitive to individual discontinuities or their interactions. Nanoindentation tests approach the length scale of these discontinuities, giving them far greater influence over testing parameters.

In the early 1980's researchers were interested in quantifying the mechanical properties of thin films. They found that with existing technology the dimensions of the film made it impossible to isolate its properties from the influence of the substrate material, even at the lowest possible loads. The limits of optical microscopy were met and scanning electron microscopy's vacuum requirements added considerable inconvenience to the test. One of the most important attributes of hardness testing is the speed and ease of the measurement, which remains crucial even at the nano-scale.

Depth sensing indentation (DSI) was developed for the measurement of mechanical properties at a size scale beyond optical capabilities. DSI is a method that records the displacement of the indenter probe as a known load is applied and then removed. The probe tip has a very well defined area function based on penetration depth, enabling calculation of the area of contact based on displacement. With this new measurement technique, loads as small as tenths of micronewtons and depths as small as fractions of nanometers, are measurable. Researchers can test thin films, surface layers and other small volumes of material. This technique measures both the elastic and plastic response of materials. Chapter 2 starts with a discussion of nanoindentation, the theory behind it, the properties derived from it and the instrumentation used to perform the tests. Section 2.1.1 is an introduction to contact mechanics, starting with elastic deformation and some basic plasticity. Mechanical property values such as modulus and hardness are calculated from idealized elastic contact theory and load-displacement data. Section 2.1.2 presents the specifics of DSI, how a test is performed and the calculations necessary to determine property values. Section 2.1.3 describes the instrumentation we use to perform these tests, along with details about indentation probes and calibration methods.

Nanoindentation is slightly different than macroscale hardness tests and requires a number of significant assumptions. In some circumstances these assumptions can lead to significant sources of error. In order to understand why our data might be inaccurate, we must first understand how the data can be distorted. Some of the common material aspects that need to be corrected for are discussed in the second part of Chapter 2. The contact area is a crucial parameter in hardness testing, and it is assumed based upon the displacement of the tip. If the surface is not ideally flat, the actual contact area can differ significantly from the predicted value. The material and the preparation can influence

how a sample will react to applied load. The contact area can be changed by pile-up around the indenter, surface roughness, and adhesion between the tip and the sample. All of these contact area changes are discussed in Section 2.2.1. Section 2.2.2 is concerned with time dependent influences on mechanical properties. Some materials experience creep, which is continued deformation at a static load. The rate a tip comes into contact with the sample has also been shown to dramatically alter the mechanical response of material. Some materials even experience time dependent initial plasticity under certain conditions. Time can be an important aspect of hardness testing depending upon the material system.

Chapter 3 discusses some research that is directly related to the experiments we have performed. Section 2.3.1 concerns previous experiments that involve small scale indentation tests on gold. Gold is one of a few systems that displays “staircase loading,” elastic loading with instantaneous bursts of plastic deformation. The role of surface features such as orientation and atomic steps and their influence on gold deformation behavior have also been investigated in the literature. Gold has some interesting electrochemical properties. It does not have a natural oxide, but one can be induced at a sufficiently high applied potential. When combined with certain other elements, gold experiences underpotential deposition, the deposition of a monolayer of the second element on the gold surface at an applied potential above the point where bulk deposition occurs. The electrochemistry of gold, the stages of formation (specifically oxide formation and underpotential deposition), and relevant literature are discussed in Section 2.3.2.

All of the experimental procedures are presented in Chapter 3. The stages of surface preparation will be discussed in detail. Any of the additional instrumentation aspects of the microscope and indentation systems will also be presented. The specifics of the electrochemical experiments are also explained.

Chapter 4 contains the results and discussion. Section 4.1 presents some of our preliminary results on gold (111), which were extraordinarily sporadic for experiments performed on the same surface and during the same day of testing. Variation in mechanical response is typically attributed to significant surface differences such as crystal orientation, oxide thickness and contamination layers. Not only is our observed variability larger, none of the previously explored reasons for variation are applicable to the surfaces in these tests. The defect controlling deformation must have spacing on the order of the tip radius, because it influences nearly every test. In a gold single crystal there are a limited number of possible defects. We identified four aspects of the crystal that can be of the appropriate spacing and might influence the displacement behavior: residual dislocation density, surface topography, vacancy concentration and stacking fault tetrahedra, and impurity concentrations.

A test matrix was constructed to isolate the influence of some of these defects on the mechanical property measurements, by changing the surface preparation parameters. Sample preparation is one of the main differences between our surfaces and those of previous investigators. Each of the three main steps to the surface preparation procedure (mechanical polishing, electropolishing, and flame annealing) follow the same general guidelines utilized by other research groups, but are inherently operator dependent. Section 4.2 discusses the reasons we chose different factors to study in our designed experiment, and the experimental results. We selected a Taguchi L-9 array to investigate

three factors at three different levels. All of the experiments in the test array had very similar results. There were some minor differences that highlight some trends that can influence variation in material behavior.

The consistency of measurements achieved with the experiments in the Taguchi array enabled us to investigate the role of surface features such as steps and surface scratching on the mechanical properties. These experiments are described in Section 4.3. Our previous attempts to look at surface steps as a cause of changes in mechanical properties were inconclusive. Previously the presence of steps did not appear to influence the indentation depth despite huge changes in the contact area from the estimated values. The test matrix provided a repeatable base line that enabled clear assessment of the influence of steps. One of the advantages of the Hysitron system is its ability to image the surface, but in some cases the tip can actually damage the surface while indexing to a new spot or imaging. Induced roughness or surface scratching can also significantly influence the hardness measurements of gold. Changes in indentation data due to interactions with the tip prior to testing can give valuable information about the original surface.

When a gold single crystal was exposed to air for a few days the mechanical properties, specifically the load needed to initiate deformation, increased significantly. If a deposit from the air can change the mechanical properties of gold, so might a controlled addition to the surface. Electrochemistry enables the surface to be discretely modified. We used gold oxide and a deposited lead monolayer to change the surface in a controlled manner. The influences of deposited monolayers on the mechanical properties are discussed in Section 4.4. All of the work is summarized in Chapter 5.

Nanoindentation has given insight into material characteristics such as hardness, elastic modulus, creep, strain hardening, energy adsorption, cracking, and phase transformations. The scale of the experiments is the cause of much of the inherent complexity of the measurements, for the tests are on the order of material features such as dislocations and grain boundaries. The mechanical behavior of small volumes of materials is not well understood. We have theories about an idealistic atomic scale and have simplified models to explain bulk behavior, but the nanometer regime is currently between these two worlds of understanding. Nanoindentation tests are small enough that there may be influences that would be masked on a larger scale. It is also more complex than an idealized atom sized mechanism. Monitoring of the displacement in a material as a load is applied tells a great deal about the surface, the stress state, and defect presence. Understanding the contribution of surface on mechanical response can eventually enable tailoring of material for specific property requirements.

CHAPTER 2: BACKGROUND INFORMATION

2.1: Nanoindentation

Hardness measurements are one of the most common ways to test the mechanical properties of materials. These tests are quick and easy, repeatable and inexpensive. Since the early 1800's, when Friedrich Mohs [1] first introduced scratch testing, relative hardness has been used to characterize mechanical properties. Almost a century later Johan Brinell [2] introduced a test in which a hard sphere was pressed into a specimen. The ratio of the force applied and the surface area of contact was defined as the hardness, a definition still used today. Many people such as Knoop, Vickers, and Rockwell [3] have all modified this test, but the principle has remained the same.

In today's drive for smaller and smaller parts, we need to understand the mechanical properties of reduced volumes of material. The reduction in scale may potentially change a material's behavior from that of its bulk form. Nanoindentation is a means of characterizing local properties of small volumes and investigating internal stresses of thin films. In the nanometer regime, atomic scale heterogeneities can have a dramatic effect on hardness tests. Factors such as location of the indent, surface preparation, surface orientation, the radius of the indenter and even the tip material play important role in the information gathered [4-8]. The mechanical response of small volumes of material is more sensitive to often-overlooked characteristics such as the surface energy and dislocation density [9-11]. Also oxides, absorbed species, compositional changes and even exposure to the environment can have significant local influence on mechanical properties [12-15]. At small enough scales, a single crystal of metal has a structure that can be thought of as a perfect lattice. This means that theoretical property values, based upon idealized atomic interactions, may be attainable. The response to point contacts on the nano-scale may differ greatly from what we observe on a macro scale due to faultless configurations or the isolated influence of a specific defect.

Very low load indents are beyond the resolution of optical techniques, and other imaging apparatus such as SEM make the tests no longer convenient. One way to maintain the ease of testing is to use a procedure called depth-sensing indentation or nanoindentation. A probe forms the indent while recording the force applied and the corresponding displacement. These displacement measurements are on the order of nanometers (nm), and the applied force is usually on the order of micro-Newtons (μN). This technique has one significant difference from traditional methods. The whole material response is recorded, both the elastic and the plastic deformation. The measurements are no longer just a measure of residual deformation. Another hundred years after Brinell, the way in which we evaluate the hardness of a material is again redefined.

2.1.1 Contact Mechanics

Indentation is the act of bringing two bodies into contact; one being a probe, extremely stiff and minimally altered by the interaction, the second is the specimen whose properties we are interested in quantifying. It is the response to this applied load that provides an indication of the mechanical properties. In order to understand and interpret what is measured during indentation testing, we must start with the theories that describe the influence of force on materials. Since nanoindentation records the displacement due to the elastic as well as the plastic deformation we must understand some of the basics of the theories of elasticity and plasticity.

Figure 2-1 is a cross-section of a flat surface and a rigid spherical indenter. The indenter radius is R , the radius of contact is a , and h_t is the total depth of penetration. The other two depths indicated are the distance from the free surface to the radius of contact (h_e), and the distance from the radius of contact to the total depth (h_p).

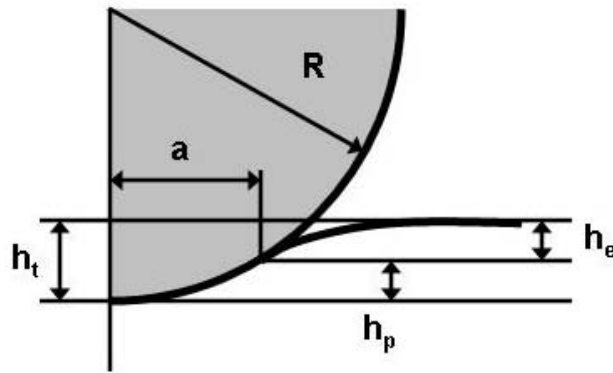


Figure 2- 1 Schematic of the interaction between a rigid spherical indenter (with radius = R) and a flat surface. The radius of contact (a) is also indicated. The total displacement of the surface is h_t , which consists of the distance from the free surface to the radius of contact (h_e), and the distance from the radius of contact to the total depth (h_p).

Hertz first theorized about idealized material contact when working with distortion due to contacting lenses in 1882 [16]. The contact distorted the lenses and caused fringes to be formed in the transmitted light. In order to understand the non-permanent change in the lens shape he began to investigate elasticity. His theory of elasticity can also be applied to the initial portion of point contact loading. He demonstrated that the radius of contact (a) is related to the combined radius of the objects (R), the load applied (P), and the materials' elastic properties (E^*) in the following manner [17]:

$$a^3 = \frac{3 \cdot P \cdot R}{4 \cdot E^*} \quad (2.1)$$

The combined radius is determined by the following expression:

$$\frac{1}{R} = \frac{1}{R_1} + \frac{1}{R_2} \quad (2.2)$$

Where R_1 and R_2 are the radii of the two contacting bodies. In the case of a rigid indentation, the sample surface is usually very flat compared to that of the indenter; therefore the radius of the indenter alone is used. The term E^* is the reduced modulus. It is a composite modulus property used to account for the non-rigid tip interaction, or the elastic interactions of the tip and the surface. An efficient method of combining the two moduli is to assume that the two materials behave as springs in series. The reduced modulus can be expressed:

$$\frac{1}{E^*} = \frac{(1 - \nu_m^2)}{E_m} + \frac{(1 - \nu_i^2)}{E_i} \quad (2.3)$$

Where E_m and E_i are the Young's Moduli for the sample material and the indenter respectively; ν_m and ν_i are the materials' Poisson's ratios. The Hertzian representation is only concerned with the local distortions at contact, not the bulk mechanics of support of two contacting bodies. The elastic contact is small compared to the overall size of the specimen and the indenter. The displacements of the points on the surface within the area of contact are given by the following expression, in respect to the origin of the specimen free surface:

$$h = \frac{1}{E^*} \frac{3}{2} \frac{P}{4a} \left(2 - \frac{r^2}{a^2} \right) \quad r \leq a \quad (2.4)$$

In this equation r is the radial distance from the axis of symmetry. This equation helps to define that of the total elastic displacement pictured in **Figure 2-1**.

Hertz was also concerned with the distribution of pressure between these two contacting bodies. The area of the sample in contact with the indenter is important because it determines the load distribution on the material. Some of the basic assumptions are that the two bodies are elastic, semi-infinite, half-spaces, with no friction between them, and the stress is equal to zero far from the point of contact. An elliptical pressure distribution satisfies all the boundary conditions. For a spherical indenter the surface pressure distribution can be expressed by:

$$\frac{\sigma_z}{p_{mean}} = -\frac{3}{2} \left(1 - \frac{r^2}{a^2} \right)^{1/2} \quad r \leq a \quad (2.5)$$

Where σ_z is the stress in the direction normal to contact, p_{mean} is the mean contact pressure, which is defined by the indenter load divided by the projected area of contact:

$$p_{mean} = \frac{P}{\pi \cdot a^2} \quad (2.6)$$

Substituting **Equation 2.1** in for the pressure leaves an expression that is independent of applied load:

$$p_{mean} = \left(\frac{4 \cdot E^*}{3\pi} \right) \frac{a}{R} \quad (2.7)$$

This mean contact pressure is also referred to as the “indentation stress”. The ratio of the radius of contact over the actual indenter radius is sometimes referred to as the indentation strain. These measures of applied force help to better interpret the material response in familiar terms. This also helps us to think of the data recorded during load application as comparable to the stress-strain data we are used to interpreting.

The normal pressure at the center of contact (p_o) is also the maximum, and in the case of a spherical indenter is equal to $1.5 p_{mean}$. At the edge of the contact area the pressure falls to zero. The pressure within the area of contact for a spherical indenter is defined as [2]:

$$p = p_o \left(1 - \frac{r^2}{a^2} \right)^{1/2} \quad (2.8)$$

Outside the area of contact it is a free surface and therefore the normal pressure is zero. The maximum pressure (p_o) is related to the total load by the expression [16]:

$$p_o = \frac{3P}{2\pi \cdot a^2} \quad (2.9)$$

During indentation, the radius of contact is a function of the material properties, the depth of the indent and therefore the radius of the indenter (R). Using **Equation 2.1** and substituting for these known values we derive the expression for maximum pressure independent of contact area:

$$p_o = \left(\frac{6 \cdot P \cdot E^{*2}}{\pi^3 R^2} \right)^{1/3} \quad (2.10)$$

Hertz did not calculate internal stress fields, but did indicate that these could be calculated by interpolating surface solutions along the axis of symmetry. As early as 1885 a comprehensive solution for the stress distribution within a solid for point contact loading was established by Boussinesq [18]. He utilized the principle of superposition to determine the stress distribution below the surface. Any shaped point contact can be represented by an appropriate distribution of varying intensity of point loads at the specimen surface. The internal stress field is then given by the superposition of each of

the point-loaded indentation stress fields. This theory has been further developed and given polar coordinates by Timoshenko and Goodier [19]. The stresses within a solid, beneath a point load can be calculated from the following functions:

$$\begin{aligned}
 \sigma_r &= \frac{P}{2\pi} \left[(1-2\nu) \left[\frac{1}{r^2} - \frac{z}{r^2(r^2+z^2)^{1/2}} \right] - \frac{3r^2z}{(r^2+z^2)^{5/2}} \right] \\
 \sigma_\theta &= \frac{P}{2\pi} (1-2\nu) \left[-\frac{1}{r^2} + \frac{z}{r^2(r^2+z^2)^{1/2}} - \frac{z}{(r^2+z^2)^{3/2}} \right] \\
 \sigma_z &= \frac{3P}{2\pi} \frac{z^3}{(r^2+z^2)^{5/2}} \\
 \tau_{rz} &= -\frac{3P}{2\pi} \frac{rz^2}{(r^2+z^2)^{5/2}}
 \end{aligned} \tag{2.11}$$

The surface stresses $\sigma_z, \tau_{yz}, \tau_{zx} = 0$, except at the origin. The direct and shear stress are both independent of Poisson's ratio, due to the fact that they act on planes within the solid that are parallel to the free surface. All of these stresses are compressive, except at the very edge of contact where they are tensile. In many brittle glasses a ring is formed at the edge of contact, caused by the localized tensile stress.

When Tresca or the Huber-Mises criterion is applied to the stresses in a metal, based on a Hertzian pressure distribution, the initial condition for plasticity is reached below the surface [2]. The principle shear stress ($\tau_1 = 1/2 |\sigma_z - \sigma_\theta|$) is higher at this subsurface depth than at the point of origin of the tip or the edge of contact. The maximum shear stress is:

$$\tau_{\max} = 0.31 \cdot p_o = 0.47 \cdot p_{\text{mean}} \tag{2.12}$$

The maximum pressure is reached at a depth of $0.48 a$, when the Poisson's ratio is equal to 0.3 [16]. The pressure is equal to $0.47 p_{\text{mean}}$, which is equivalent to $1/2 Y$ where Y is the yield stress. This results in a relation of $p_{\text{mean}} = 1.1 Y$ [2]. If the mean pressure is below this level, all deformation is elastic, after which plastic deformation begins.

Indenter geometry has a considerable influence on the pressure distribution during indentation. So far all of the equations of displacement and pressure distribution are for spherical indenters. A large number of experimentalists utilize pyramidal or conical indenters, which alter some of the previous equations. The reasons why we choose different indenters and some of the specifics of their geometry will be discussed in Section 2.1.3. Pyramidal indenters are often approximated by a cone, with a half angle (α) resulting in the same area to height ratio. For a conical indenter, the equation that defines the radius of contact between the tip and sample becomes [20]:

$$a = h_p \tan \alpha \tag{2.13}$$

Where h_p is the depth of contact as shown in **Figure 2-2**.

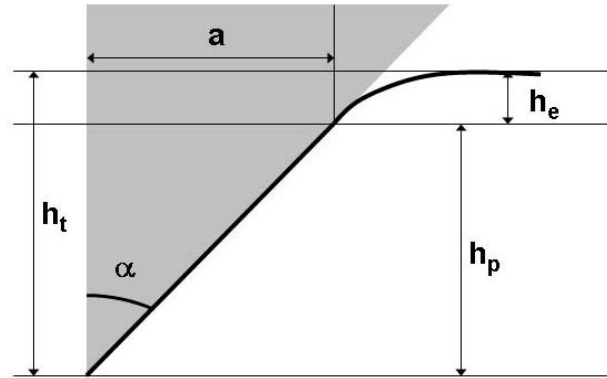


Figure 2- 2 Schematic of contact between a conical indenter (with half angle α) and a flat surface. The radius of contact (a) is also indicated. The total displacement of the surface is h_t , which consists of the distance from the free surface to the radius of contact (h_e), and the distance from the radius of contact to the total depth (h_p).

The semi-angle of the cone is α . If the apex of the cone were ideally sharp, the pressure at this point would be infinite. This would eliminate any elastic deformation even at the lowest of loads. Most conical or pyramidal indenters have an initial radius of curvature at their point. The equation for load for a conical indenter with a blunt tip is defined by [21]:

$$P = \frac{\pi \cdot a}{2} E^* \cdot a \cdot \cot \alpha \quad (2.14)$$

Where the $a \cot \alpha$ is equal to the depth of penetration (h_p) at the radius of contact. The deflection of the surface equation is also different [20]:

$$h = \left(\frac{\pi}{2} - \frac{r}{a} \right) \cdot a \cdot \cot \alpha \quad r \leq a \quad (2.15)$$

The change in geometry also changes the mean pressure at which the material begins to plastically deform. For a conical indenter the mean pressure is $0.5Y$. The maximum shear stress is [2]:

$$\tau_{\max} = \frac{E^*}{\pi} \cdot \cot \alpha \quad (2.16)$$

The pressure distribution for the Hertzian model, where a rigid sphere is elastically loaded onto a flat surface is well defined. When the indenter shape is changed to conical, the pressure distribution changes, as does the area to depth ratio. In the case of a spherical indenter the radius of contact increases much faster than the depth as load

is applied. For conical indenters the radius of contact and the depth of penetration have a constant ratio, independent of load. Conical indenters are geometrically similar. This results in a constant strain within the material during loading. Increasing the load on a spherical indenter is comparable to decreasing the semi-angle of a conical indenter.

The mechanical properties of materials, the way in which they respond to applied load, can ultimately be correlated to the strength of its bonds. At long range, atoms tend to attract, while at very close range they repel. Metals tend to form lattices that optimize their separation. Elasticity can be thought of as the material's ability to deform without breaking its bonds. Therefore plasticity is the movement of atoms relative to one another, caused by an applied load. The force required to slide one row of atoms from its initial low energy state, over another row of atoms, to an equivalent position of perfect registry is called the theoretical shear stress. This situation is represented schematically in **Figure 2-3**.

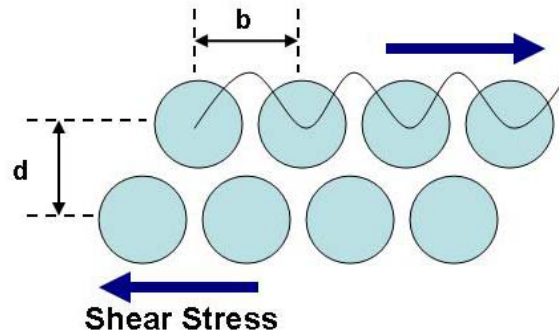


Figure 2- 3 Schematic of the theoretical shear stress, the force required to slide one row of atoms over another, to a location of perfect registry.

Frenkel first calculated this theoretical value for load necessary to initiate plastic deformation in 1926 [22]. As evident by the illustration, the atom movement is periodic in b and can be approximated as sinusoidal, because the high and low energy locations have the same repeat units. The applied shear stress (τ) is given by the expression

$$\tau = \frac{Gb}{2\pi d} \sin \frac{2\pi x}{b} \quad (2.17)$$

where G is the shear modulus of the material, b is the spacing of the atoms in the direction of applied shear stress, d is the spacing of the rows of atoms, and x is the shear translation of the two rows of atoms away from their initial low-energy equilibrium position. The maximum value for τ is the theoretical shear stress, and can be expressed as follows:

$$\tau_{th} = \frac{Gb}{2\pi d} \quad (2.18)$$

Since b is comparable in size to d , the theoretical shear stress is often considered a fraction of the shear modulus. Numerous researchers have used different mathematical treatments that have resulted in theoretical shear strengths that range from $G/5$ to $G/30$. The approximation of $G/5$ is most likely an over estimate because the attractive forces between atoms fall off more quickly than is predicted by the sinusoidal model [22]. This model also fails to take into account other low energy configurations such as twins. The low end approximation of $G/30$ was calculated by Mackenzie [23] using central forces for close packed metal. This is most likely an underestimate because it ignores thermal stresses and directional forces. All of these estimates result in theoretical shear stresses on the order of gigapascals for most metals. Experimentally measured values (depending upon experimental parameters) are usually lower by one to four orders of magnitude. The difference is often explained by the abundance of material defects such as dislocations. With improvements in instrumentation, single crystal growth techniques, and computational capacity, we have been able to measure and simulate values that are in the same range as these theoretical values [5, 24, 65]. The similarity demonstrates the validity of the predicted range of theoretical strengths of materials, unfortunately without giving us a definitive equation. This model also helps us to visualize the stresses required on an atomic scale for plastic deformation.

There are three regions of the elastic-plastic response of material. The first region is the elastic deformation, defined by $p_{mean} < 1.1Y$ for spherical indenters and $p_{mean} < 0.5Y$ for conical, where no permanent damage is done to the surface once the load is removed. As previously stated the maximum shear stress under a spherical indenter for completely elastic behavior is approximately $0.47 p_{mean}$, and occurs at a depth of half of the radius of contact ($0.5a$), below the sample surface. Employing either von Mises' or Tresca's criteria for maximum shear stress required for the onset of yield, we define when plasticity begins. von Mises indicates an initial yield at $p_{mean} = 1.0Y$ and Tresca a similar $p_{mean} = 1.1Y$. This occurs at $\tau_{max} = 0.5 Y$. The next region of response is the onset of plastic deformation. It begins below the surface, when the mean pressure is between $1.1Y < p_{mean} < CY$ for a spherical indenter and $0.5Y < p_{mean} < CY$. Where C is a constant defined by the material and the indenter geometry. It is very difficult to know the size, shape and evolution of this deformation, for it is all subsurface. Eventually the plasticity reaches the free surface of the material. This third stage is continued plastic deformation, where the mean contact pressure remains relatively constant despite increases in the applied load, $p_{mean} = CY$. The increase in contact area is proportional to the increase in load, such that the mean pressure remains the same, assuming there is no work hardening.

There is a point at which the mean contact pressure does not change despite increasing load. The mean contact pressure at this limiting condition is the measured hardness (H) of the material for analysis techniques that utilize projected area of contact. The mean pressure between the sample and the indenter is directly proportional to the material's yield or flow stress (Y) in compression.

$$H \approx C \cdot Y \quad (2.19)$$

Where C is the "constraint factor" for it represents the job done by the surrounding material that creates a hydrostatic component. It is the surrounding material that causes the mean contact pressure of an indentation test to be higher than the required load to

initiate deformation in a uniaxial compression test. The shear component is the part that initiates plastic flow. This constraint factor is dependent upon the experimental parameters such as the sample material and tip geometry. Both experimentation and theory have determined a range for C , between 1.5 and 3 [2]. For metals with a large E/Y value, C is closer to 3.

As soon as the tip penetrates the surface its volume must be accommodated. In some material/tip combinations, this happens by plastic flow. In others it is local elastic strain. One way to conceptualize the changes required by the addition of a loaded probe is the “expanding cavity” model, where the volume under the indenter is represented by a hemispherical core subjected to an internal pressure which is directly related to the mean contact pressure [2]. **Figure 2-4** is a schematic of the expanding cavity model.

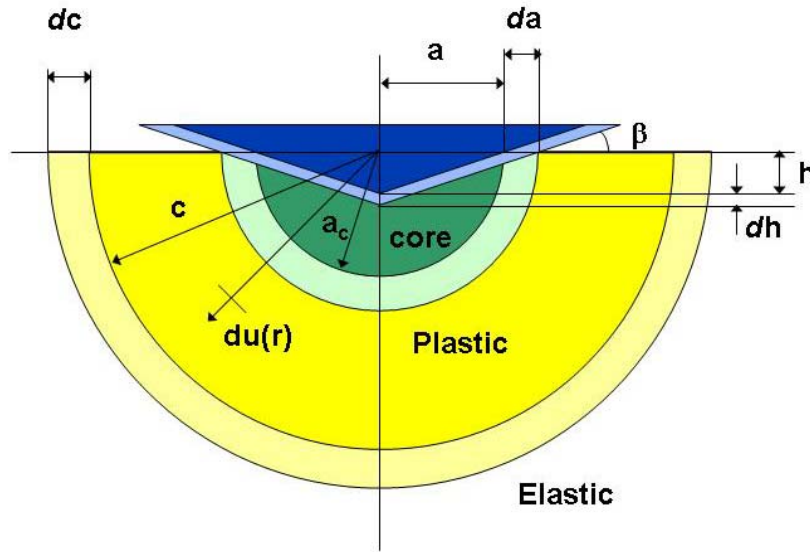


Figure 2- 4 Schematic of the expanding cavity model. The contacting area between the sample and indenter is the hydrostatic core of radius a_c . The core is surrounded by a plastic zone of radius c , which is constrained by a region of elastic deformation. As the tip is further indexed into the surface (dh), the core grows in size (da), by the radial movement of material ($du(r)$) to accommodate the added volume, also increasing the plastic zone (dc).

The contacting surface between the indenter and the sample define the incompressible hemispherical hydrostatic “core,” with a radius a_c . The core is surrounded by a deformable plastic zone of radius c . As the indenter is indexed into the surface amount dh , the core radius expands da , and the plastic zone expands dc . It is the added volume of the indenter, which is accommodated by radial movement of the atoms (du), which causes the expansion of the plastic zone. For geometrically similar tips, such as conical indenters, the core and the plastic zone grow at the same rate, $da/dc = a/c$. Johnson utilized this relation to calculate the pressure in the core as follows [16]:

$$\frac{p}{Y} = \frac{2}{3} \left[1 + \ln \left(\frac{(E/Y) \tan \beta + 4(1-2\nu)}{6(1-\nu^2)} \right) \right] \quad (2.20)$$

Where p is the pressure within the core and β is the angle of inclination of the indenter with the surface. For spherical indenters with small β , $\tan \beta$ can be replaced by the indentation strain a/R . This leads to an expression for the mean contact pressure (p_{mean}) in terms of the yield strength:

$$p_{mean} = p + \frac{2}{3}Y \quad (2.21)$$

At some point the free surface will begin to influence the shape of the plastic zone. When the plastic region is no longer elastically constrained, and the free surface has a considerable role in the shape of the plastic zone, the volume occupied by the indenter starts to be accommodated in a different way. The material begins to flow, piling up around the indenter. At this point the material behaves as a plastic solid, for the elastic deformation is considerably smaller than the plastic flow. The plastic yield is related to the critical shear stress, as dictated by the Von Mises or Tresca failure criteria. This model has been demonstrated to be a good fit, especially for materials with high E/Y ratios. This model also helps us to understand the different observed stages of deformation during indentation.

2.1.2 Depth Sensing Indentation

The value most commonly sought in indentation tests is a material's hardness. Hardness tests started as a way of comparing materials, testing their quality, and quantifying their properties. While traditional hardness tests and nanoindentation measure slightly different things, the purpose remains the same. In macroscopic testing a load is applied and the residual imprint left by that load is optically measured to determine the contact area. The ratio of applied load ($P_{applied}$) to residual contact area ($A_{residual}$) gives the hardness (H_{macro}):

$$H_{macro} = \frac{P_{applied}}{A_{residual}} \quad (2.22)$$

This hardness value is the plastic response of the material to applied load. The measurements of the residual contact area are only as good as the resolution of the imaging technique. There becomes a size scale beyond the capabilities of optical microscopy, where Scanning Electron Microscopy (SEM) or Scanning Probe Microscopy (SPM) would be necessary to image the indent. On the nanometer scale it is no longer convenient or time efficient to make measurements in this manner with either of these techniques.

One of the reasons nanoindentation was developed was to test the mechanical properties of thin films. Microindentation available in the early 1980's did not allow for loads low enough to isolate the properties of the film. The guideline within the field is

that indentation depth should only be about 10% of the total film thickness to ensure that only the film is tested without influence from the substrate. An optical technique at this scale is not viable. It is difficult to accurately apply such small loads and the uncertainty in the measured area is too high. For a $1\mu\text{m}$ indent this uncertainty could be as high as 100% [20].

New methods of testing that accurately apply loads and measure the displacement meant that visual inspection of the indented area was no longer necessary. With the old analysis techniques only the residual plasticity was measured. Now the initial elasticity as well as the elastic recovery that occurs during unloading are recorded. In order to determine the desired material properties such as hardness, new analysis techniques must be developed. The results from these tests are very sensitive to the details of the analytical approach.

Nanoindentation utilizes continuous measurement of the displacement as the load is applied and then removed. These measurements must have a displacement resolution of at least 0.1 nm and a force resolution of $0.1\ \mu\text{N}$ [25]. **Figure 2-5** is a typical loading profile and the corresponding load displacement curve for nanoindenters operating on an AFM (Hysitron, Inc.) as discussed further in Section 2.1.3. Before the indentation test begins the imaging gains are removed and no load is applied to the tip, in order to measure any drift in the transducer. The displacement is measured as a function of time, and the remainder of the test is corrected by this measured drift rate. The indentation test will only begin if the probe drift is below a specified level (typically $<0.1\text{nm/s}$). The loading portion of the curve measures the material's resistance to penetration. The loading slope is primarily dependent upon the sample material and the shape and size of the indenter. The hold segment at maximum load is used to determine if there is time dependent plasticity or creep in the material. Time dependent plasticity will be discussed further in Section 2.3.2. The extent of recovery in the depth of the material upon unloading is directly related to the degree of plasticity and recovered elastic deformation.

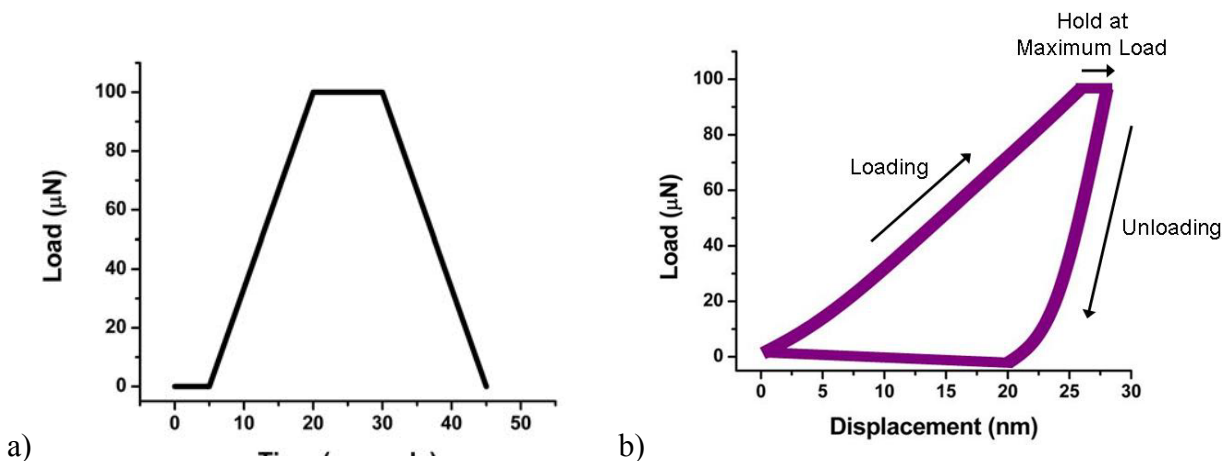


Figure 2- 5 a) Loading profile for typical indentation test. The transducer drift is observed in the first 5 seconds, followed by loading from 5 to 20 seconds, then a hold at maximum load for 10 seconds, and finally gradual unloading over the final 15 seconds of the experiment. **b)** Load-displacement curve on mechanically polished gold, subjected to testing profile in (a). (Initial drift check not pictured)

An elastically deformed material will retrace the loading curve upon unloading (**Figure 2-6 (a)**). An elastoplastic material response is shown in **Figure 2-6 (b)**, the material displays a mixture of elastic and plastic behavior. A primarily plastically deformed material will have almost no elastic recovery (**Figure 2-6 (c)**). A material that behaves in an entirely elastic manner, rubber for example, will have an indeterminate hardness using traditional indentation methods, because there would be no residual impression. Depth sensing indentation on the other hand will provide valuable information on the elastic properties of the material. Measuring the entire response of the material gives a more complete picture, which is necessary at the nano-scale.

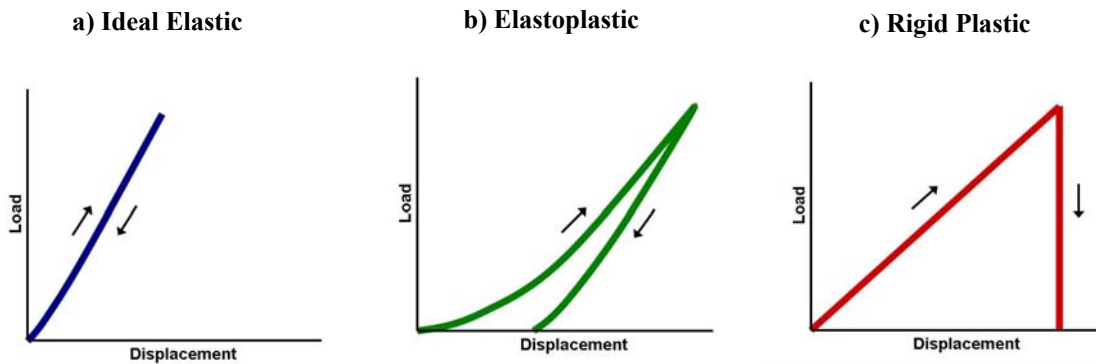


Figure 2- 6 Representative load-displacement data demonstrating differences in elasticity a) Completely elastic material b) elastoplastic material c) ideally plastic material.

Different analysis techniques have been developed for each segment of the loading profile. The loading portion requires models that include both elasticity and plasticity. The hold portion is commonly used to investigate creep behavior. The unloading portion of the curve can be treated as the elastic recovery of the material. In practice, analysis of the loading and holding portions of the curve require numerous assumptions about the relationship between plasticity and contact area. The most common analysis techniques utilize the unloading portion of the indentation data, primarily because they are the least model dependent.

Nanoindentation analysis is based upon the assumptions that the radius of curvature of the indenter is small compared to that of the specimen's surface and the dimensions of these objects are large compared to the contact area. By establishing that the size of the indent is small compared to the whole system, we can isolate the stresses and strains caused by indentation from those of the specimen, such as attachment of the sample, surface constraints (boundaries), and geometry. We also assume that the contacting bodies are frictionless, that only the normal force is transmitted to the sample.

Over the years numerous research groups have investigated how best to interpret the load-displacement data that is collected during indentation testing. The investigation of the role of elasticity in material deformation began well before the reduction in component scale demanded a new testing method. In 1961 Stillwell and Tabor were looking at elastic recovery of conical indentations and how they related to mechanical properties [26]. Armstrong and Robinson were measuring materials' combined elastic and plastic deformation during indentation testing in 1974 [27]. In 1981 Lawn and

Howes utilized elastic recovery in hardness measurements [28]. The first researchers to utilize the unloading portion of the load-displacement curve as a means of determining the contact area were Bulychev, Alekhin, Shorshorov, and Ternovskii in 1975 [29]. Doerner and Nix [30] were the first to use this technique in the millinewton load range, where the indents become too small to measure accurately by optical means. Oliver and Pharr slightly modified this technique in 1992. A similar analysis technique was developed by Field and Swain that concentrated on spherical indenters [31]. In 1993 these last two techniques were shown to be equivalent [32].

All these techniques start by examining the idealized elastic contact of a rigid sphere and a flat surface. In 1965 Sneddon [33] published the derivation of an expression for the contact between a rigid indenter of various geometries and an isotropic elastic half space. He defined the contact stiffness (S) as the increment of load (δP), divided by the increment of displacement (δh):

$$S \equiv \left. \frac{\delta P}{\delta h} \right|_{\text{elastic}} \quad (2.23)$$

This ratio can be related to the initial unloading portion of the force displacement curve, with the assumption that the initial unloading is entirely elastic. Although most materials deform in both an elastic and plastic manner, most recovery upon unloading is thought to be elastic in nature. The residual deformation is the plastic response, related to the final depth (h_f). The tip is also assumed to be ideally rigid; any elastic response is accounted for in the reduced modulus (E^*). The contact stiffness can be written as a function of modulus and projected contact area (A_c) at maximum load [33]:

$$S = \frac{2}{\sqrt{\pi}} E^* \sqrt{A_c} \quad (2.24)$$

This relationship is called the conical Sneddon stiffness equation. The area of contact is based upon the tip shape. Every tip has a well-defined area function dependent upon the depth of penetration. From this equation we see that the unloading slope is directly related to the modulus of the material and the square root of the area of contact.

Doerner and Nix [30] were the first to establish a commonly used method for determining hardness and modulus from force displacement curves on the nanometer scale based on these principles. They assumed that the initial unloading was linear, and the intercept depth (h_i) was found by extrapolating the tangent at P_{max} to zero load. Hardness measurements based upon this linear extrapolation more closely correlated to experimental data and finite element analysis for materials of well-known hardness, as compared to values attained using the depth at peak load (h_{max}) or the final depth (h_f). Although this was a better approximation, there were still some problems with the interpretation. Oliver and Pharr [34] found that the initial unloading more closely resembled the behavior of the power law, and not necessarily linear unloading. They fit the initial portion of the unloading curve with the relation:

$$P = \alpha(h - h_f)^m \quad (2.25)$$

Where α and m are curve fitting parameters. In the Hysitron software, this equation is fit to the unloading curve in the region of 95-40% of the maximum load [35]. The derivative of this power law relation with respect to h , is taken at the maximum load ($P = P_{max}$), the resulting slope is equal to the contact stiffness ($dP/dh=S$) of the material.

Sneddon's analysis for elastic displacement outside the contact perimeter gives the following relation:

$$h_{max} - h_c = \varepsilon \frac{P_{max}}{S} \quad (2.26)$$

Where h_{max} is the maximum indentation depth, h_c is the contact depth, and ε is a constant that depends on the shape of the indenter. For a spherical indenter $\varepsilon = 0.75$. Pharr and King [36, King, 1987 #95] have both shown that this relationship holds for a number of geometries: any that can be described with a function of revolution, with pyramidal shaped indenters having a very small error. Therefore, when using a three-sided pyramidal Berkovich indenter, a spherical indenter is a sufficient approximation.

The maximum load over the stiffness term in **Equation 2.26** can be rewritten in terms of displacement:

$$h_c = h_{max} - \varepsilon \cdot (h_{max} - h_i) \quad (2.27)$$

Where h_i is the intercept depth, determined by extrapolating the initial unloading slope to $P = 0$. The intercept depth is an underestimate for the contact depth. **Figure 2-7 (a)** is a schematic of the indenter and material cross-section and **Figure 2-7 (b)** is the corresponding load displacement image.

In order to make these calculations, a very accurate description of the tip's projected area of contact, as a function of depth, is necessary. The tip area function is experimentally determined. The particulars of these measurements will be discussed in the next section (Section 2.1.3). The projected area of contact for each indent is the solution to the area function at $h=h_c$. Using the power law relationship for unloading and a well-defined function for the tip area, the hardness of the material can be defined as:

$$H_c = \frac{P_{max}}{A_c} \quad (2.28)$$

Where H_c is the hardness, P_{max} is the maximum indentation load, and A_c is the projected area of contact at depth h_c . It is evident from this definition that any inaccuracies in determining the depth of contact might dramatically influence the calculated hardness value. Miscalculations in the area of contact influence the applied stress, and can therefore dramatically change the calculated hardness. Section 2.2.1 discusses some of the ways in which the contact area can be misinterpreted.

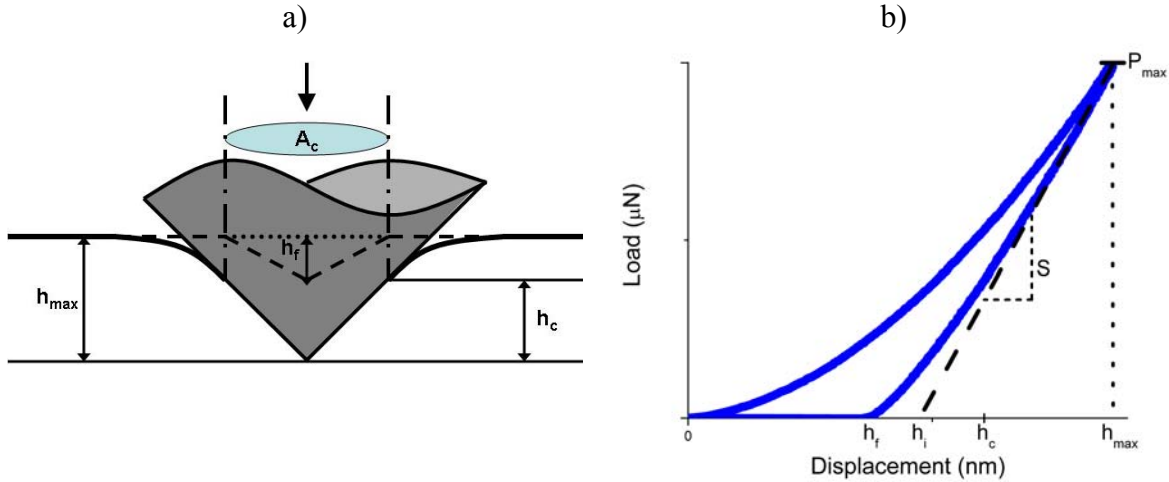


Figure 2- 7 a) Schematic of an indenter at maximum load (P_{max}), with an associated total depth of h_{max} . The contact between the indenter and the surface at maximum load is defined by depth h_c , with a corresponding projected area of contact A_c . The dashed line, with a final depth of h_f , indicates the sample profile after the load has been removed. **b)** Corresponding load-displacement curve, indicating the final depth (h_f), the intercept depth (h_i), the contact depth (h_c), and the maximum depth. The slope of the tangent at maximum load is the dashed line. The stiffness (S) is the slope of this line.

The other material property often sought in indentation testing is the modulus of the material. There is one major assumption in the calculation of the indentation modulus: that it remains constant over all depths. The reduced modulus is calculated using the area of contact and the stiffness:

$$E^* = \frac{\sqrt{\pi}}{2\sqrt{A_c}} S \quad (2.29)$$

From here the modulus of the material can be calculated using **Equation 2.3** and accepted values for the Young's Modulus and Poisson's ratio of the indenter. In the case of a diamond indenter these values are 1140 GPa and 0.07 respectively [35]. The resulting value is the Indentation Modulus, which is defined as:

$$I = \frac{E_m}{1 - \nu_m^2} \quad (2.30)$$

During indentation testing, at all scales, materials demonstrate widely varied responses to the same load, characteristic of the materials and their preparation. Small quantities of materials can behave strangely due to the unique microstructures of the size regime. Grain size, film thickness, and epitaxial stresses are a few of the scale specific features that can influence hardness testing. The size scale of nanoindentation changes some of the ways to interpret load-displacement data. A fundamental understanding of the mechanical response of a material to point contacts is necessary for further advancement of nanotechnology.

2.1.3 Instrumentation

Over the past 20 years a number of systems have been developed to monitor displacements of fractions of nanometers as a load is applied, held, and released. Commercially available systems are purchased by universities, research labs, and an increasing number of corporate product development labs. Most systems are load controlled. This means that there is no specified minimum depth for most instruments, for the depth of penetration is material dependent. The force and displacement resolution are also important, but they can not be controlled. They are dependent upon the instrument and the location of that instrument. The resonant frequency of a building, the ability to control the temperature, even air quality can influence the consistence of measurements.

The term nanoindentation is often applied to three slightly different size scales, based upon the instrument capabilities. Starting with the largest, there are indentation tests that apply loads of milliNewtons, causing displacements on the order of hundreds to thousands of nanometers. This is just beyond the low end of what is referred to as micro indentation. The next range, which is the group our instrument belongs to, applies loads in the range of 10's to 1000's of microNewtons, measuring total displacements up to 100's of nanometers. There is an even smaller scale method of indentation testing that utilizes a specialized Atomic Force Microscope cantilever as its probe tip. This final scale is sometimes referred to as interfacial force microscopy, but falls under the family of nanoindentation because it is making mechanical property measurements on the nanometer scale. This entire category of indentation that is displacement controlled. Each of these different scales of testing has their own specific applications and instrumentation. The measurements investigate slightly different aspects of a material's mechanical response, primarily determined by the scale. There are surface features, assumptions in calculation, and other possible distortions unique to each size regime. Together they bridge the gap from microindentation to nearly the scale of atomic simulations.

2.1.3.a Hysitron Triboscope

The Hysitron Triboscope is a unique and powerful instrument because it is a quantitative nanoindentation system and it has the ability to image the surface before and after indentation. It does not utilize the piezo feedback nor the Atomic Force Microscope (AFM) cantilever to perform its tests. The nanoindenter is an attachment (accessory) to a scanning probe microscope. The whole system is shown schematically in **Figure 2-8**. The Triboscope itself has three main parts: the transducer, the transducer controller and a separate data acquisition system [35]. The Scanning Probe Microscope (SPM) software is used to interpret the voltage signal from the transducer, and the microscope piezos enable displacement control when imaging. The transducer holds the indenter tip which doubles as a probe for imaging. The resolution of the image is not as good as those

obtained with an AFM or STM tips due to the bluntness of the indenter. It does give sufficient resolution to identify desired surface features and to choose optimal areas to indent. The system has a depth resolution of 0.2 nm and can apply indentation loads as high as 13.0 mN with a resolution of 0.1 μ N[35].

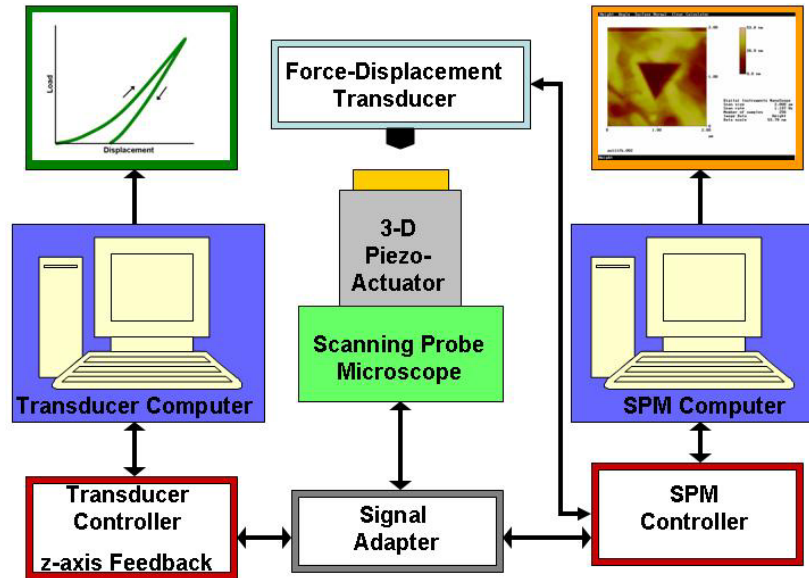


Figure 2- 8 Schematic of the indentation system which consists of two instruments, the Triboscope and a Scanning Probe Microscope (SPM). The SPM contributes the imaging software and displacement control. The indentation system consists of the transducer, controller, and a separate data acquisition system.

The Triboscope uses a simple three-plate capacitor system for its force-displacement transducer [35]. **Figure 2-9** is a sketch of the transducer configuration. The two outer plates (the drive plates) are fixed and the middle plate is spring mounted, and therefore free to move. This middle plate has a screw, which is where the tip attaches. To perform an indentation an electrostatic force is generated between a drive plate and the pick up electrode. The electrostatic force (F_{el}) is proportional to the square of the Voltage (V) applied to the drive plate:

$$F_{el} = k_e \cdot V^2 \quad (2.31)$$

Where k_e is an electrostatic force constant (determined by the manufacturer and supplied with the transducer). The area of the plates and the distance between them determines this electrostatic force constant. Once calibrated the instrument determines the appropriate voltage profile to apply the required force profile for the specified indentation test. For displacement sensing, the two outer electrodes are driven by AC voltage that is 180° out of phase. This results in an electrostatic field whose potential varies linearly with lateral displacement, due to the close proximity of the plates. In the center this field is zero, because the two fields cancel each other out. At the location of either plate the field is proportional to the voltage applied. The middle plate or pick-up electrode

assumes the potential of the position relative to the drive plates. The displacements are measured by changes in the capacitance of the stack of plates. This enables the displacement and applied load to be measured simultaneously.

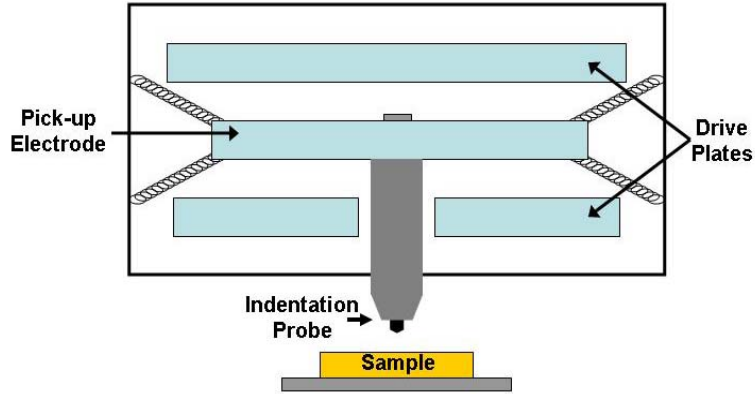


Figure 2- 9 Schematic of a three plate capacitor force-displacement transducer of the Hysitron Triboscope. Voltage applied to the drive plates creates an electrostatic force with the pick-up electrode. The displacement is monitored by changes in capacitance.

In order to use the force displacement data, there are a few corrections that must be made. The electrostatic force consists of both the force applied to the surface and the force required to move the indenter further into the surface. In order to determine the applied force the spring displacement must be subtracted from the total electrostatic force.

$$F_{\text{applied}} = F_{el} - k_s \cdot h \quad (2.32)$$

The spring constant is k_s and h is the displacement of the middle plate. This spring constant can be determined simply by doing an indent in air, where the force on the sample is equal to zero.

Every instrument has a certain amount of inherent deflection occurring during testing that is directly proportional to the load. It is measured as penetration into the surface and must be corrected for. The compliance of the machine (C_m) consists of deflection due to the load frame, the indenter shaft and the specimen mount. At large loads for materials with a high modulus, this can account for a large portion of the displacement. The total compliance of the system (C_t) is the machine compliance plus that of the indented material, which is equal to one over the material stiffness [34]:

$$C_t = \frac{dh}{dP} = C_m + \frac{1}{S} = C_m + \frac{\sqrt{\pi}}{2E_r \sqrt{A}} \quad (2.33)$$

This expression demonstrates that the total compliance can be considered as springs in series, simply adding the separate components. The total compliance varies linearly with

the reciprocal of the contact area squared ($A^{-1/2}$). If this relationship is plotted, the machine compliance is the intercept with the y-axis.

In order to determine this value a number of indents are made in an aluminum crystal. Aluminum is chosen for its almost perfectly plastic behavior. The indents are imaged after testing in order to measure the area of the indent. The total compliance is determined from the inverse of the unloading slope for each indentation (dh/dp). The compliance is plotted versus the reciprocal of the measured indentation area. The machine compliance is the y-intercept. Once this value is determined it is entered into the software and used to correct raw data accordingly.

2.1.3.b Tips

The probe tip is a very important part of indentation testing. The geometry and the material it is made from can dramatically influence the raw data. The material is important because of how the stiffness influences the reduced modulus and because of local adhesion that might occur between the sample and the tip. Adhesion will be addressed specifically in Section 2.2.1.c. The most common shapes of indenters are spheres, flat punches, cones, and pyramids. Each of these has its own pressure distributions, and therefore different load requirements for deformation.

At the macro scale there are numerous methods for hardness determination, many that employ different shaped indenters. The Brinell method utilizes a spherical indenter, while the Rockwell Test is done with a conical indenter, and the Vicker's method utilizes a four-sided pyramidal probe. Each of these has their own analysis technique that results in a unique hardness number. As indentation tests became smaller the Knoop tip was developed. This four sided pyramidal diamond probe has two different face angles. The length of the longer diagonal is much easier to accurately measure when using traditional visual inspection for very hard materials and shallow depths of penetration. The Knoop tip is also very useful for looking at anisotropic properties of a surface. As hardness testing became even smaller, many of the same principles were applied

Probe tips are even more important in nanoindentation, for the material properties are calculated based upon their dimensions. Tips of the same geometry as macroscopic testing are used at this scale: spheres, flat punches, cones, and pyramids. Spherical tips are not self-similar; therefore the induced strain increases with indentation depth. This leads to scaling of the hardness with indentation depth in materials that strain harden. Pyramidal and conical indenters are self-similar; the ratio of radius to depth is constant. Theoretically materials that have homogeneous hardness should have the same result independent of depth of indentation. It is common for hardness to change with indentation load or depth, even in the case of self similar tips. There is one significant difference in the pyramidal indenters used in nanoindentation. They are three sided as opposed to four sided. Four sided objects often result in a line at the junction. Three sided objects always meet at a point. This being said, no point is perfect. The radius of the apex is critical because it dictates the contact area. Tips are usually categorized as sharp and blunt. This is primarily a relative term with no rigorous criteria, very dependent upon context. For example, a tip that is extremely sharp may reach critical stresses at very low loads, acting as a knife cutting through the material creating new surfaces with little elastic deformation. This would mask important information such as

initial yield strength. With blunt tips elasticity plays a more important role. The larger contact area means that higher loads must be used to initiate plasticity. This would also mean that the tip is not as sensitive to surface anomalies. Depending on the properties being studied there may be an optimal tip radius.

The majority of our research has been done with a Berkovich indenter. **Figure 2-10** is a sketch of the three sided pyramidal indenter. The Berkovich indenter has a face angle of 65.3° , which results in an equivalent cone angle of 70.32° . The face angle was chosen to give the same projected area to depth ratio of a Vickers indenter. A typical Berkovich indenter has a radius on the order of 50-300 nm [20].

For Depth Sensing Indentation accurate knowledge of the area of contact is crucial. No tip is perfect, which is why we experimentally determine the area of contact as a function of depth. The first step is the idealized function relating the projected area of contact to the contact depth, based on the equivalent cone angle. For a Berkovich indenter this is:

$$A = 24.5 \cdot h_c^2 \quad (2.34)$$

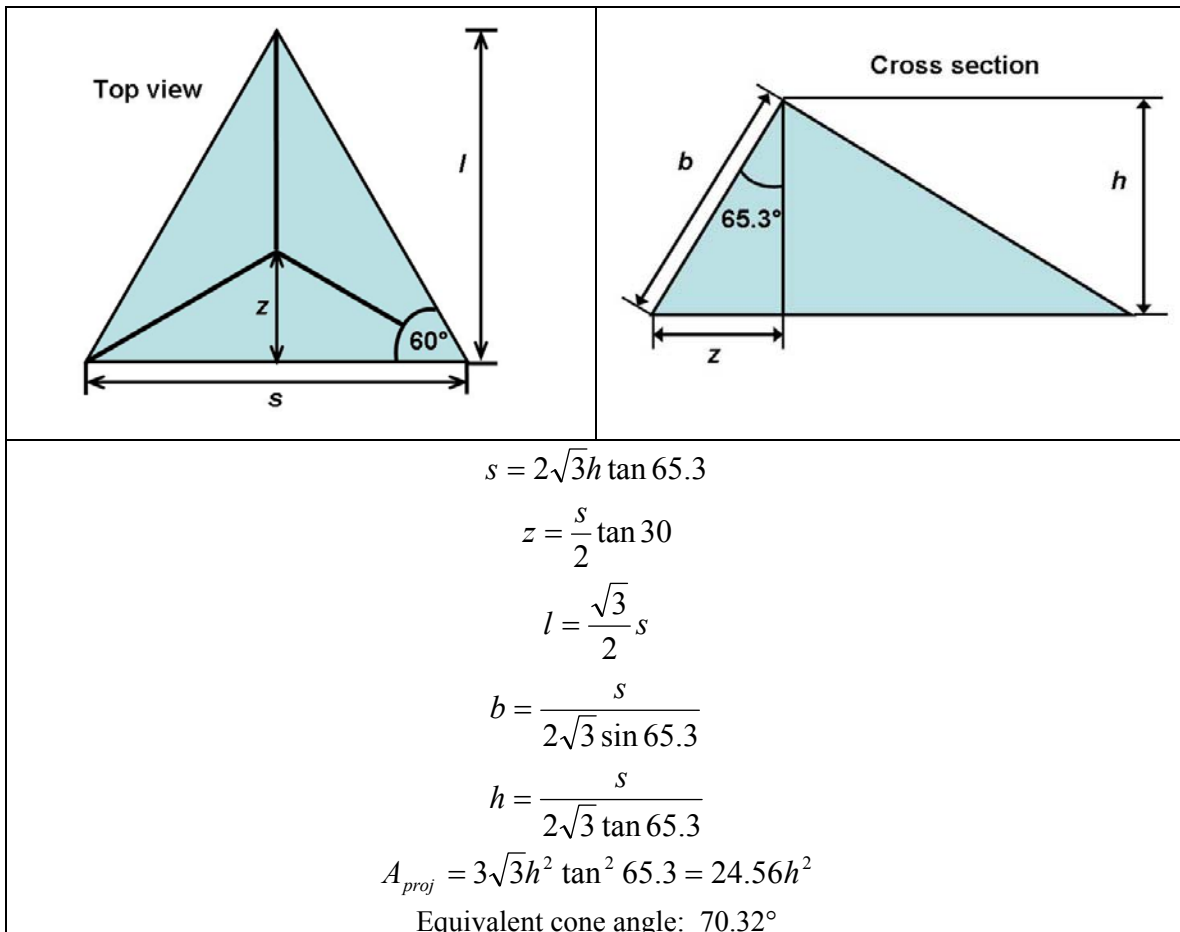


Figure 2- 10 Schematics of a Berkovich indenter with dimensions a) Top view b) Cross Section c) Equations for dimensions of tip indicated in schematics.

The area of contact is related to the material contact stiffness. **Equation 2.24** can be rewritten as:

$$A_c = \frac{\pi}{4} \left(\frac{S}{E^*} \right)^2 \quad (2.35)$$

This enables the contact area to be determined based upon measured stiffness of a material with a known reduced modulus. Fused quartz is the sample material used in tip calibrations. It is used because it has an extremely consistent measured modulus of 72 GPa. The reduced modulus for a diamond indenter and fused quartz is 69.6 GPa. Its amorphous structure enables the consistent deformation behavior of the material. Fused quartz does not display some of the discrepancies between the actual and the calculated contact area, sometimes displayed in metals. For example it does not experience distortion in the contact area that is caused by piling-up or sinking-in. **Figure 2-11 (a)** shows numerous load-displacement plots done on fused silica, and **Figure 2-11 (b)** is an image of a typical fused quartz surface after indentation testing. **Figure 2-11 (a)** demonstrates the load displacement behavior of this well behaved material. There are numerous indents made at each load (2000, 1000, and 500 μN). Some of the tests were even run on different days. The material is extremely repeatable; the loading behavior is identical in every trial and the depth of penetration is consistent for a given load. This demonstrates the consistent nature crucial for accurate tip shape calibration.

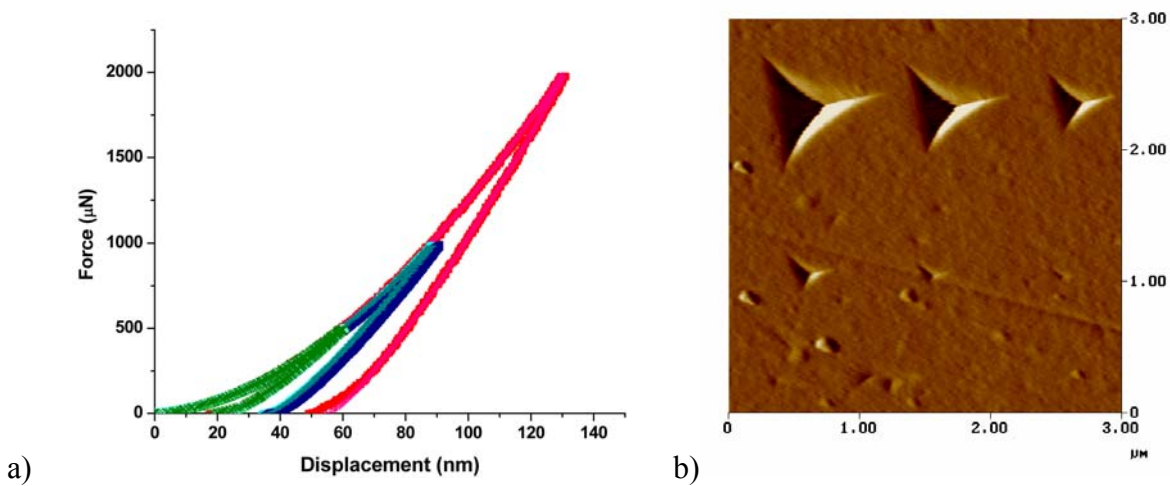


Figure 2- 11 a) Indentation tests on fused silica, done at numerous loads on different days of testing. b) Surface image of fused quartz, done by indentation probe after testing, showing indents of a variety of sizes. Tests like these are used to create a tip area function.

Indentation tests are done over the desired range of contact depth. The stiffness is taken from each of these indents and a corresponding projected area of contact is calculated using **Equation 2.33**. The computed projected area of contact is plotted as a

function of contact depth. The points are then fit to a fifth order polynomial given by the following equation:

$$A = C_0 h_c^2 + C_1 h_c + C_2 h_c^{1/2} + C_3 h_c^{1/4} + C_4 h_c^{1/8} + C_5 h_c^{1/16} \quad (2.36)$$

Where C_0 is equal to 24.5, and the rest are curve fitting parameters. **Figure 2-12** is a plot of the calculated projected area of contact as a function of contact depth for the Berkovich indenter used in all of our experiments. This results in the following tip area function:

$$A = 24.5 h_c^2 + 6.46 \cdot 10^3 h_c - 1.63 \cdot 10^5 h_c^{1/2} + 9.31 \cdot 10^5 h_c^{1/4} - 1.54 \cdot 10^6 h_c^{1/8} + 7.42 \cdot 10^5 h_c^{1/16}$$

Which is represented by the red line in the image. All of the calculations for hardness seen throughout the rest of this document utilized this tip area function in the calculations.

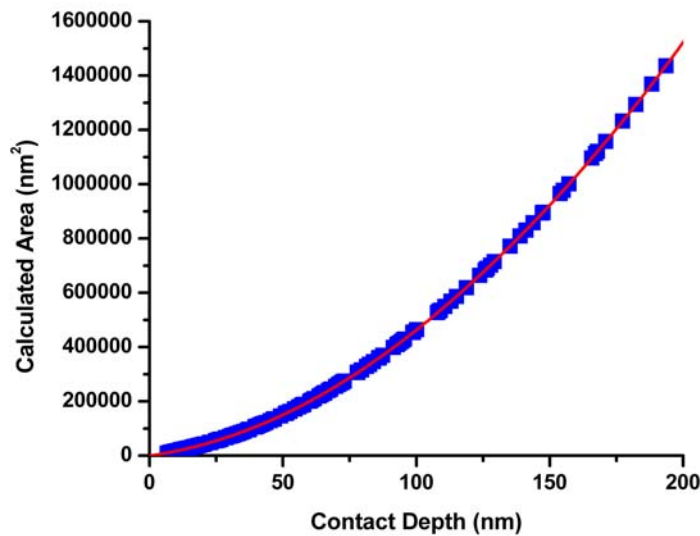


Figure 2- 12 Plot of the calculated projected area of contact as a function of penetration depth of the Berkovich indenter used for experimentation. The curve fit is the projected area of contact as a function of contact depth.

2.2: Potential sources of data distortion

In the previous section we have discussed idealized elastic and plastic behavior and the analysis methods used to calculate material properties from the displacement that occurs as a load is applied. A description of the tools necessary to make these measurements has also been given. There are some aspects associated with these tools such as load frame compliance and tip shape anomalies that must be accounted for. There are other sources of error for depth sensing indentation measurements that are caused by the material and the testing parameters. Unlike those associated with the apparatus, these distortions are material specific and therefore much harder to identify and correct.

Accurate knowledge of the contact area is crucial in determining a truly representative hardness number. Some materials exhibit deformation behavior that can lead to significant miscalculations in the contact area. Under certain loading conditions some materials pile-up around the indenter increasing the contact area. Other materials experience sink-in, seeming to collapse from the area surrounding the indenter. There are other contact area problems that are introduced due to the scale of testing. Surface anomalies and roughness are not significant issues at the macro-scale but can influence nanoindentation considerably. Depending upon the scale of the roughness it can mean that only a fraction of the indenter tip is truly in contact with the surface. With some material pairs adhesion is also an issue that must be addressed since it can also influence the contact area. Aspects of the material and its preparation may significantly influence the measured mechanical properties. Recognition of behavior that might alter contact area will help us determine the accuracy of measured hardness values.

Certain materials exhibit time dependent deformation. Creep is defined as continued plasticity at a constant load. The continued deformation is often apparent in the hold at maximum load. The rate at which the probe comes in contact with a material can also have a significant influence on the indentation behavior. Materials that demonstrate displacement bursts at the onset of plasticity have shown this property to be time dependent. In the material systems that are subject to time dependent plasticity, the measured mechanical properties may vary depending upon the testing parameters. Identifying when a material is affected by the duration and rate of contact may help us to adjust testing parameters to achieve more repeatable results.

2.2.1 Contact Area Changes

Hardness measurements rely heavily on accurate determination of area, at both the macro- and the nanoscale. Even traditional hardness test have to account for material characteristics that might adversely affect the measured area. Shallowing is a term that refers to the difference in radius of curvature of the indenter as compared to that of the residual impression. For hard materials, the difference in radius can be as large as a factor of three [2]. This is attributed to elastic recovery of the material. It is for this reason that the diameter of the impression is measured and not the depth, for the effect is

much smaller in this direction, usually only a change of a few percent. One of the most significant attributes of nanoindentation is that measurement of the residual deformation is not directly measured to determine the mechanical properties of the material. This method relies on calculated contacts based on idealized material behavior. Anything that distorts the contact area makes the property values inaccurate. In this section we address some of the potential sources for inaccurate estimation of contact area.

2.2.1.a Pile-up and Sink-in

At a particular depth of penetration the contact area is dependent not only upon the tip shape, but also the elastic properties of the material. Materials with limited elasticity accommodate the volume of the indenter by plastic flow of the material, eventually piling-up around the tip. This often happens in materials that are work hardened prior to testing. Elastic materials accommodate the indenter by longer range elastic deformation. In such cases the material appears to sink-in around the tip. Sink-in is often associated with well annealed samples. **Figure 2-13** is a schematic of these two situations shown in cross section and a top view. The left-hand side of the image shows sink-in, or a reduction in contact area, while the right hand side shows pile-up which can significantly increase the contact area. These figures demonstrate that the extent of elastic deformation can dramatically change the contact area from that predicted by the total displacement of the probe. The Oliver and Pharr method produces reasonable mechanical property values for most materials. Since the analysis technique is based on idealized elastic contact, which predicts material to be drawn downward during contact, the Oliver and Pharr method is a good approximation for materials that experience sink-in. The influence of pile-up is more pronounced on property calculations.

Bolshakov and Pharr [37] did extensive finite element analysis on the influence of material properties on the shape of deformation zone during simulated indentation testing. In systems that demonstrated pile-up they measured differences of up to 60% between the calculated contact area and the actual contact area. They found that only materials that did not work-harden (pre-work hardened materials for example) experienced pile-up. In order to quantify the amount of elastic recovery in a system they utilized the ratio of the final depth (h_f) over the maximum depth (h_{max}). For entirely elastic material the ratio would be equal to zero, and for a purely plastic response the ratio would equal one. All materials with a ratio below 0.7 experience sink-in, regardless of their ability to work-harden. Materials with an h_f/h_{max} value above 0.7 experienced pile-up. The amount of pile-up corresponds to the size of the plastic zone, or the load applied.

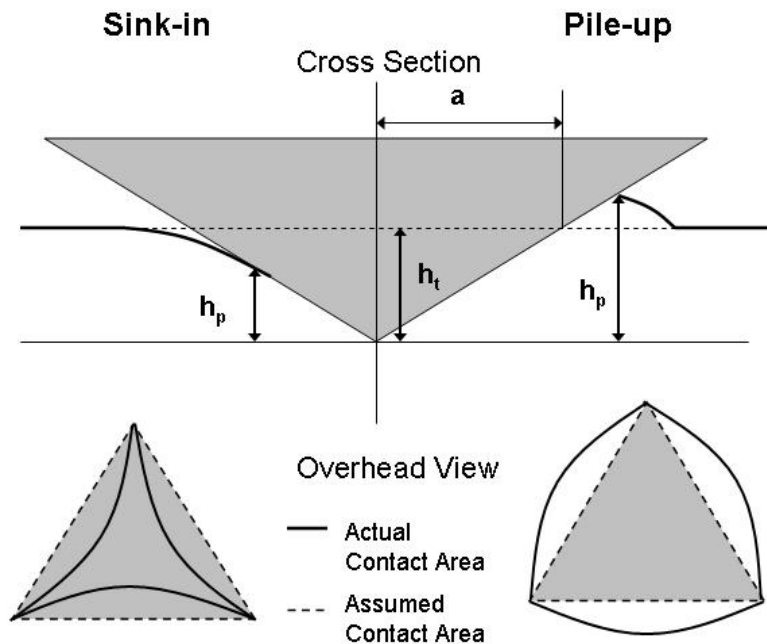


Figure 2-13 Schematic representation of pile-up and sink-in. Top picture is a cross-section of the indenter at maximum load. The radius of the projected area of contact (a) based upon displacement is an overestimate in the case of sink-in and an over estimate for materials that pile-up. This is easily visualized by the overhead view, where the assumed contact area is indicated by dotted lines while the actual contact area is indicated by the solid lines.

Materials that do not experience significant strain hardening, for examples those that have already been strain hardened, have a plastic zone that is hemispherical in shape. The deformation zone is dependent upon the ratio of the elastic modulus to the yield stress (E/σ_y) [20]. When E/σ_y is large the plastic zone often extends beyond the area in direct contact with the tip. When additional plasticity occurs near the indenter, pile-up occurs. When the E/σ_y ratio is small the deformation to accommodate the tip is more localized. In materials that do experience strain hardening, the yield strength changes as a function of deformation. This is why in strain hardening materials the plastic zone extends into the material, and the radius of deformation is reduced. The change in yield strength means that the material at the edge of the plastic zone is softer than that directly under the tip, and the additional volume of the tip can be accommodated without plastic flow.

It is a common misconception that soft metals such as gold and copper experience significant pile-up all of the time. Many soft metals work-harden readily and are often seen to pile-up around an indenter in such cases. Soft FCC metals are also commonly used as a representative soft film for investigation of substrate effects on indentation data [38, 39]. The problem of pile-up is often extreme in situations of a soft film on a hard substrate, for the indents often penetrate well into the substrate. The discontinuity in materials creates an extreme case for plastic flow of the soft film. The dramatic increase in the contact area can cause overestimations in hardness as large as 100%[38]. Pile-up is

not a function of being a soft material, but rather is closely correlated to whether the material is work hardened or annealed.

2.2.1.b Roughness

Real surfaces are never ideally flat. Often there are even a variety of scales to the surface modulations. On a macroscopic scale roughness has little effect on indentation testing, provided the indent is large compared to the asperity size [2]. Traditionally this has meant that the finish of the surface and the indenter have not been a significant concern. In the nanometer regime care must be taken to identify the influence of roughness of different frequencies. Many of the surface modulations are significantly larger than the area of interest; hence locally it can be approximated as flat. But there are often surface features on the same order and even smaller that influence the images or experiments being performed. The contact between two bodies is not only controlled by the material properties (elastic modulus and hardness) but by topographical properties as well. Three parameters of the surface also play an important role in the contact of two engineering samples. These are the surface density of the asperities, the standard deviation of the height distribution, and the mean radius of the asperity [40]. In nanoindentation the roughness can lead to significant error in the calculated contact area.

Depth sensing indentation analysis techniques are based on Sneddon elastic contact model, which states that there is a single point of contact [33]. A machined surface for example, has a significant roughness on the nanoscale. **Figure 2-14** demonstrates how a rough surface can cause numerous points of contact with an indenter. The non-uniform contact increases the localized stress at the points of intersection, deforming the material to a greater depth at relatively low loads. This can result in a greater displacement and lower calculated hardness for a rough surface compared to a smooth one.

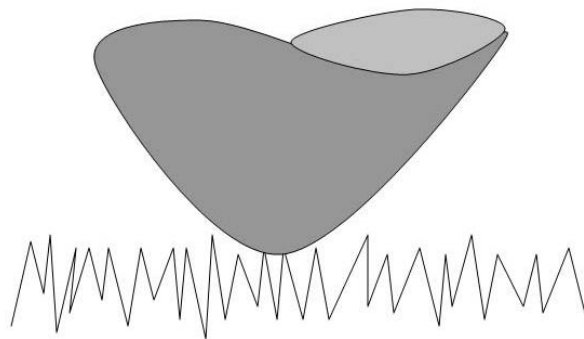


Figure 2- 14 Schematic of the non-uniform contact between an indentation tip and a rough surface. The over estimate in contact area compared to that assumed based on displacement will lead to increased localized stress, generating greater deformation, resulting in an underestimate of hardness.

Bobji and Biswas used finite element analysis to investigate the role of surface roughness on nanoindentation experiments [41, 42]. They found that roughness significantly increases the scatter in hardness, especially at small depths. The extent of scatter and the measured values depended upon the analysis method. They use two approaches for calculating the contact area, an imaging method and a DSI method. The imaging technique uses the mean height, determined over a large area, as the reference plane for deformation. The depth sensing method measured the depth of penetration from the asperity of first contact. The depth sensing method consistently resulted in lower hardness values and increased scatter. They also investigated the influence of changing the yield strength parameter. Experiments with a constant hardness throughout were compared to those whose surface hardness varied with depth. The function for the change in yield strength causes the material to become softer as the volume of the indent increases. This is often seen in experimental indentation studies, the material is measured to be significantly harder at smaller depths; this is often referred to as indentation size effect. While they did look at how differences in the surface mechanical properties might influence indentation, they did not explore work hardening. It would be interesting to investigate how initial asperity deformation in materials that work-harden might influence the indentation results.

One of the most common methods for quantification of surface topography is the root mean square (rms) roughness (R_q). This is a powerful tool due to the simplicity and statistical significance. The term is defined as:

$$R_q = \left[\frac{1}{n} \sum_{i=1}^n (y_i - \bar{y})^2 \right]^{1/2} \quad (2.38)$$

where n is the number of data points, y_i are the relative vertical heights, and \bar{y} is the mean height of the surface. R_q describes the height distribution about the mean value. The mean height of the surface is defined by:

$$\bar{y} = \frac{1}{n} \sum_{i=1}^n y_i \quad (2.39)$$

The most obvious limitation of this method is the lack of information about the width or spacing of the asperities. There is no information about the different roughness frequencies that often coexist.

Scanning probe microscopy is a very powerful tool, in part due to the digital nature of the data. The digital format enables extensive statistical analysis of the surface. Quantification of the surface can be achieved through height distribution analysis and identification of periodic feature wavelengths. Any mathematical method used to calculate hardness will be influenced by imaging artifacts in the data collection [43]. The tip radius is often sighted as a filter for high frequency component of surface topography. There is also usually a planar artifact caused by the fact that the tip and surface are almost never perfectly perpendicular. There are also instrumentation issues such as drift and non-linearity in the motion of the piezoelectric scanner. Kiely and Bonnell [43] have done a comparison of different mathematical treatments that quantify surface topography,

pointing out many of the attributes and limitations, as well as the influence of data collection issues. They suggest many ways to ensure that the calculated roughness values are truly representative. Roughness characterization needs a description of the length scale, the size of the image in relation to the largest feature size, and the processing performed on the image, in order to have a complete picture of what the value means.

2.2.1c Adhesion

All of the analysis techniques at this scale assume that there is no significant adhesion between the probe and the sample. According to these theories when the load goes to zero so does the contact area. This may not always be the case depending upon the materials involved and their surface finish. Some tip/sample pairs experience considerable adhesion. In these cases the probe and sample remain in contact after the load goes to zero, and even require a significant negative force to return the tip to the original displacement. **Figure 2-15** is an indentation test done on a gold surface with a tungsten probe. The load reaches a negative load of over 23 μN before the tip and sample separate. Other researchers have reported that when a tungsten probe is used on a gold surface deformation occurs prematurely (at loads lower than those observed with other probe materials) and some gold is even transferred to the probe surface [44].

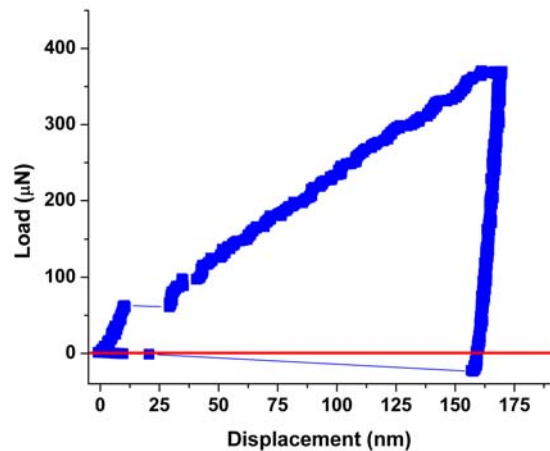


Figure 2- 15 Load displacement curve demonstrating adhesion between the probe tip and the sample, evident by the large negative load required to separate them.

Many researchers have addressed the influence of surface force on deformation behavior [16, 45, 46]. Johnson, Kendal and Roberts [8] expressed the adhesive force as energy balance between the loss of surface energy (U_s) and the increase in stored elastic energy (U_E). The lost surface energy can be expressed as:

$$U_s = -2\pi a^2 \gamma \quad (2.40)$$

Where a is the radius of the projected area of contact and γ is the energy per unit contact area for both surfaces. The energy balance per unit of contact can be written as:

$$\frac{dU_E}{da} = \frac{dU_S}{da} = -4\gamma\pi a \quad (2.41)$$

Equations 2.8 and **2.9** can be combined to rewrite the Hertz pressure distribution as a function of radial distance from the axis of symmetry (r):

$$p(r) = -\frac{3}{2} \frac{P}{\pi a^2} \left(1 - \frac{r^2}{a^2}\right)^{1/2} \quad r \leq a \quad (2.42)$$

The minus sign indicates compression. The pressure due to adhesion can be expressed as:

$$p_A(r) = \frac{P}{2\pi a^2} \left(1 - \frac{r^2}{a^2}\right) \quad (2.43)$$

Using the derivative of the force distribution due to adhesion and equating it to the lost surface energy per unit of contact, the force due to adhesion can be expressed in terms of the mechanical properties of the material and the actual contact radius:

$$P_A = \sqrt{8\pi a^3 \gamma E^*} \quad (2.44)$$

Adhesive forces increase the contact area over that predicted by the Hertz equation. The apparent load (P_1) is the combination of the applied load and the adhesive force ($P_1 = P + P_A$). This is shown schematically in **Figure 2-16**.

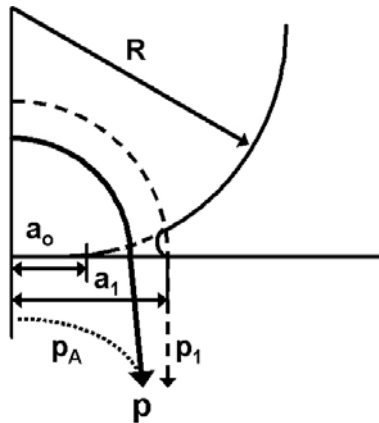


Figure 2- 16 Schematic of the contact between two elastic solids with an external load P . The Hertzian contact model predicts a radius of contact a_0 , with a pressure distribution of p . The addition of adhesion between the two bodies in the JKR model will increase the contact radius to a_1 . The apparent pressure distribution p_1 is the combination of the contact pressure (p) and the adhesion pressure (p_A).

The applied load can be rewritten (using **Equation 2.1**) as:

$$P = P_1 - P_A = \frac{4}{3} \frac{E^* a^3}{R} - \sqrt{8\pi a^3 \gamma E^*} \quad (2.45)$$

This equation indicates that the actual radius is larger than that predicted by the Hertz equation. The actual contact radius can be expressed as:

$$a^3 = \frac{3}{4} \frac{R}{E^*} \left[P + 3\pi R \gamma + \sqrt{6\pi R \gamma P + (3\pi R \gamma)^2} \right] \quad (2.46)$$

If the energy per unit of contact goes to zero, this reduces to the Hertz equation. An interesting point is that even when the load goes to zero the contact radius is still equal to:

$$a_0^3 = \frac{3}{4} \frac{6\pi R^2 \gamma}{E^*} \quad (2.47)$$

with an adhesive force (P_0) acting on the spheres equal to:

$$P_0 = 6\pi R \gamma \quad (2.48)$$

P_0 is not the pull off force, or the critical load required to separate the two surfaces. The pull off force is given by the expression:

$$P_c = -\frac{3}{2} \pi R \gamma \quad (2.49)$$

The pull off force is independent of the elastic modulus, and only depends on the relative radii of curvature and surface energy. The ratio of the actual contact pressure over that due to adhesion is proportional to the indentation strain. This equation enables you to quickly determine the role of the adhesive force based upon the dimensions of contact and the reduced modulus.

$$\frac{P_1}{P_A} = \frac{1}{3} \frac{a}{R} \frac{\sqrt{E^* a}}{\sqrt{\pi \gamma}} \quad (2.50)$$

A material system that has a relatively low reduced modulus would increase the role of the adhesive force. The materials would be compliant and have increased contact even when the indent is large. As the reduced modulus gets larger the scale of the contact, given by the indentation strain, dictates the degree of adhesion. Indicating stiff materials only have increase in contact at very small contacts. The role of adhesion is dependent upon the modulus of the material and the size of the indentation.

2.2.2 Time Dependent Properties

2.2.2.a Creep

Nanoindentation assumes elastic-plastic behavior and does not take into account any time dependent behavior. Some materials have viscoelastic properties that can influence the load displacement data. Creep, or time dependent plasticity, is often observed in indentation testing as continued deformation during the hold at maximum load. Creep is indistinguishable from thermal drift of the transducer, which is also most apparent during a hold at constant load.

There are four primary mechanism of creep deformation. These are dislocation glide, dislocation creep, diffusion creep, and grain boundary sliding. Usually more than one mechanism is happening at a time. Dislocation glide usually occurs at very high stress levels. The rate of creep is correlated to the ease of dislocation motion, in other words the distribution and influence of barriers such as precipitates and other dislocations. Dislocation creep is the glide of dislocation assisted by the presence of vacancies. Diffusion creep is the flow of vacancies and interstitials under applied stress. It is the primary mechanism at low stresses and high temperatures. Grain boundary sliding is not a significant portion of steady state creep, but is important in keeping the material together during the other creep mechanisms. Vacancies play an important part in these creep mechanisms. Because vacancy concentration is exponentially dependent on temperature, it is no surprise that increasing the temperature has a dramatic influence on creep behavior.

Using a hot stage nanoindentation system, researches performed hardness tests on gold at elevated temperatures [47]. They found that the increase in temperature significantly increased the extent of creep during the hold at maximum load. This results in significant reductions in the measured hardness. An interesting aspect of this data was that the increase in creep rate caused by the elevated temperature seemed to dramatically influence the extent of displacement during the loading portion. This reminds us that while creep is most easily recognized during the hold at maximum load, it also occurs during loading and unloading.

The two most commonly reported mechanical property values determined from nanoindentation testing are hardness and modulus. The modulus is correlated to the unloading slope of the material. Changes in the unloading slope caused by material creep can significantly influence the calculated modulus. Gold experiences creep, and therefore the indentation tests will most likely result in inaccurate modulus values.

2.2.2 b Time dependent plasticity

Some materials exhibit instantaneous jumps in displacement, or “pop-ins”, during indentation testing [48-58]. Research groups have recorded such displacements in the loading curves of semiconductors, ceramics, and metals [51-58]. This phenomenon has been shown to exist in both single crystals and polycrystalline materials [49]. Different

materials experience similar phenomenon for very different reasons. For example in Silicon, the displacement excursion indicates a pressure-induced phase transformation [51, 52]. In nickel and aluminum the “pop-in” is due to surface oxide failure [30, 59]. In some cases there is more than one excursion in a single loading curve, often referred to as staircase loading [5]. The presence of repeated excursions indicates that the displacement bursts are not always breakthrough events. “Pop-in” on tungsten and gold is associated with the onset of plasticity. The load at which plasticity begins can vary dramatically. In these systems the hardness of a material can be dependent upon when the load is removed, for very different values can be measured depending upon if an excursion is about to occur or has already happened. Generally, when the yield point is at a relatively high load, the lengths of the displacement are longer, and when yield occurs at a lower load the excursions are smaller and more numerous. If the elastic deformation is thought of in terms of potential energy, the more stored energy the further the dislocations will travel to restore equilibrium. If indentation tests are performed to high enough maximum loads the material will demonstrate repeatable behavior, eventually following a geometrically necessary loading curve dictated by the size and shape of the tip.

Bahr et al. [60] looked at the influence of temperature and time on the elastic deformation observed prior to displacement jumps. They found “pop-in” events are independent of temperature but can be time dependent. Fe-3%Si single crystals also experience displacement excursions as a result of the onset of plastic deformation. The load at which “pop-in” occurs is often called the yield load. They performed indentation tests with extended holds at maximum load. The duration of these hold were as long a 5 minutes and the maximum load at which they were held corresponded to the average value of the load of the first excursion. Under these conditions there were three responses: the material yielded during loading, yielded during the hold, or the material did not yield at all. We have observed the same behavior in gold, with the addition of locations that yielded during the unloading of the material. **Figure 2-17** is the load displacement data for these four responses to the same load on the same sample. When the maximum load on the Fe-3%Si single crystals was increased the material usually yielded during loading portion. In the cases it did not yield prior to the hold, the time required for the initiation of plastic deformation was considerable shorter than those observed at the average value load. If the maximum load at hold was decreased from the average value, the material was less likely to yield during loading. The time required to initiate deformation also increased. Asif and Pethica [61] have stated that it is unlikely that there are any mobile dislocations present prior to the excursions. They used a continuous stiffness method of taking measurements, which superimposes a small amplitude force oscillation at relatively high frequency on to the test force signal. They found that if a load is held before an excursion the stiffness remains the same, indicating the material does not deform. If a load is held after the excursion, the stiffness increases indicating that the material continues to deform. The yield load variability observed in Fe-3%Si single crystals indicates that the onset of plasticity is not only load dependent, it is also influenced by dislocation nucleation rate.

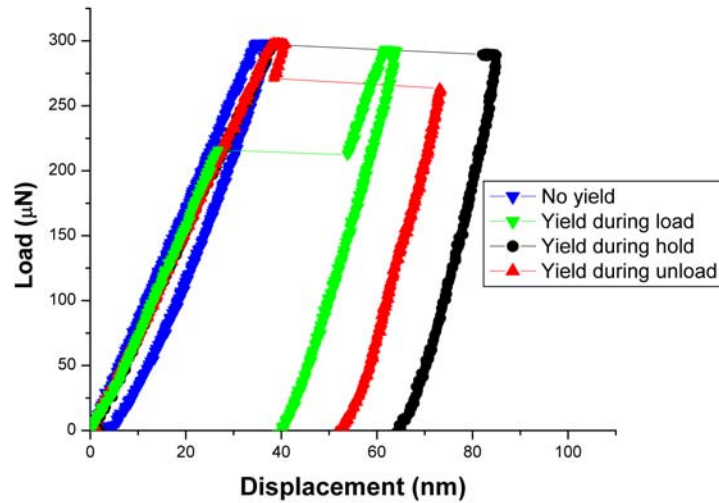


Figure 2- 17 Load-displacement data for a tungsten probe on a gold (111) surface. In gold displacement jumps indicate the onset of plastic deformation. These indentation tests show a wide variety of yield behavior. One of the indents deforms elastically, never experiencing a yield point. One of the indentation tests yields during the loading portion of the test, another during the hold at maximum load, and another during the unloading of the surface. This demonstrates that the onset of plastic deformation can be time dependent in the appropriate load range.

2.2.2 c Impact Velocity

The ability of a material to absorb load by elastic strain has been correlated to surface features such as oxides and orientation, but it may also be a result of the testing parameters. Mann and Pethica suggested that the impact velocity could influence the load at which the material yields [62]. They performed indentation experiments on GaAs varying the rate at which the tip comes into contact with the sample. They found that the impact velocity had a dramatic influence on the remainder of the deformation behavior. When a low impact rate was used there was considerable elastic loading in the sample. Eventually, a very well defined yield point at a repeatable load indicated the onset of plasticity. When the impact rate was high, they observed multiple yield points and even displacement jumps on unloading. The yielding events occurred at relatively low loads and were highly variable. They also found that the initial contact stiffness was very dependent upon impact velocity. The contact stiffness is correlated to the geometry of contact between the tip and the sample. This indicates that the contact area is larger when the impact velocity is higher. They did not find a gradual change in the stiffness, but rather two stiffness levels that appear to correlate to the transition from elastic deformation to the initiation of plastic deformation on contact. These results indicate that the physical response of the surface during the formation of contact can influence subsequent mechanical response to applied load.

2.3: Related Research

2.3.1 Indentation Testing on Gold

The first to document a difference in material response to point loading on the small scale were Gane and Bowden [24] in 1968. Performing hardness tests inside an SEM, they observed that the loads needed for a stylus to penetrate the surface of an Au crystal approached that of the theoretical shear strength. They measured on average a hardness value of 2.9 GPa. This is a considerable increase from the average microindentation result of about 220 MPa. The high loads required to initiate deformation are well within the range associated with the theoretical shear strength of gold, which depending upon the method of calculation, is reported to be in the range of 1-6 GPa.

Tangyunyong et al. [58] were the first to show discontinuous loading in gold, at an applied pressure near gold's theoretical shear strength. They used the precise displacement control of Interfacial Force Microscopy (IFM) in an indentation mode and monitored the load. Previous tests using IFM had significant problems due to the strong adhesion between the gold and the tungsten probe tip. Plastic deformation occurred almost immediately and Au was even transferred onto the tip [63]. To prevent the distorting influence of the metals adhesion, the gold surface was coated in a monolayer of thiol. They use a self-assembled monolayer technique to grow a single layer of molecules to act as a barrier to attraction between the W and the Au. The addition of this passive layer enables Hertzian loading of the sample with no indication of adhesion. It is not a barrier to dislocations or absorbent of significant force. Even after significant plastic deformation the passivating layer remained intact [63].

Gold experiences jumps in displacement during indentation testing (Section 2.2.2 b). Gold does not have an alternative structure to FCC, eliminating the possibility of pressure induced phase transformations. Images taken after indentation have no indication of any surface fracture, demonstrating that the material is not microcracking. The only explanation for these displacement excursions in gold is dislocation nucleation and propagation. Loading in gold is completely elastic until the point of excursion. This is shown by the unloading curve tracing the loading curve almost exactly in **Figure 2-18 (a)**. Images taken after this indentation (**Figure 2-18 (b)**) reveal no damage to the surface. The "pop-in" seems to be an event of plastic deformation, often followed by continued elastic loading as seen in **Figure 2-18 (c)**. The resultant deformation is shown in **Figure 2-18 (d)**. The yield point, or start of the excursion, marks an elastic-plastic transition.

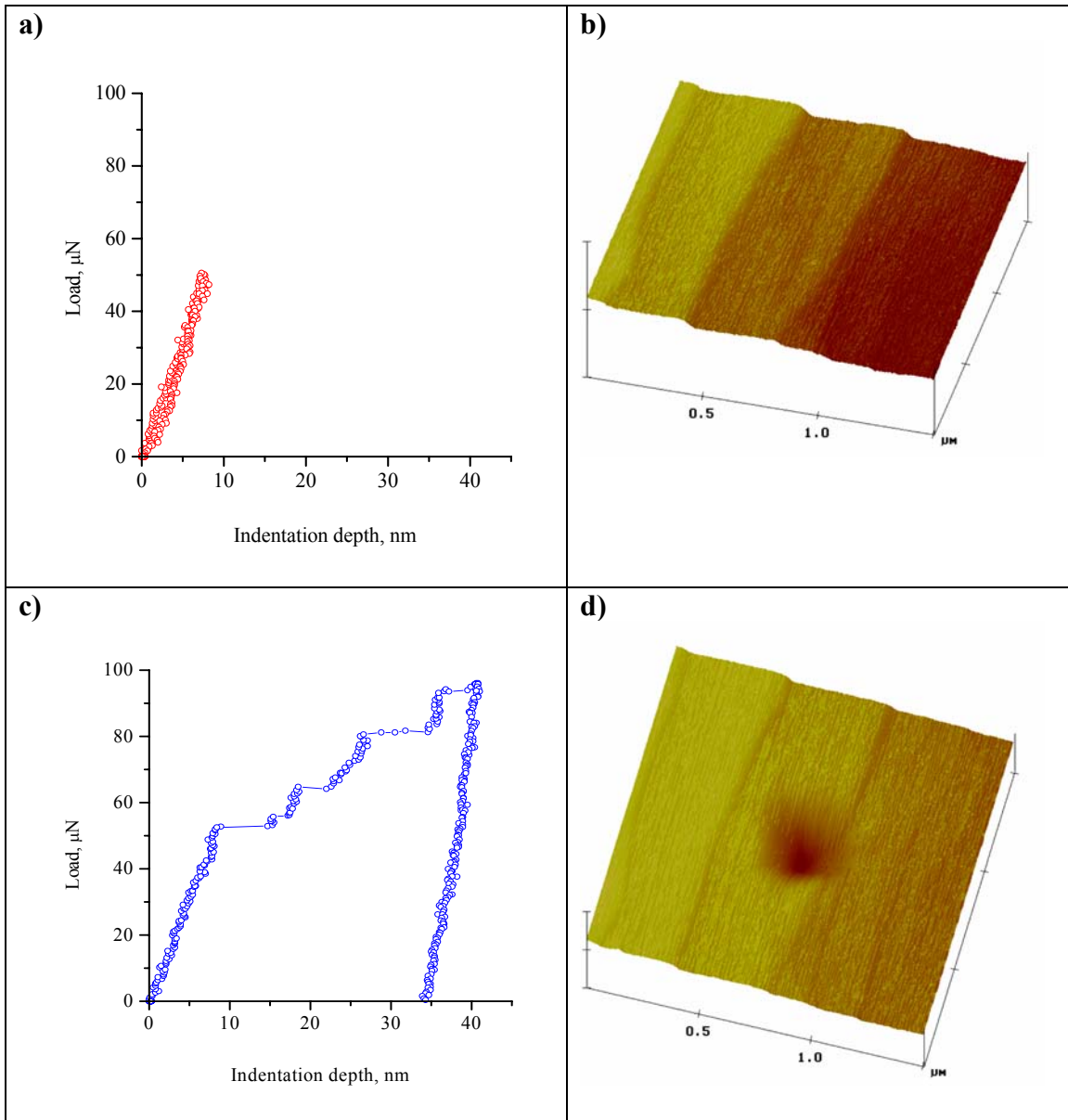


Figure 2- 18 a) Load-displacement data on gold surface, exhibiting elastic deformation indicated by the unloading tracing the loading curve. **b)** Image taken after indentation test pictured in (a). No residual deformation confirms that the displacement was elastic in nature. **c)** Load-displacement data on same gold surface. Higher load has initiated plastic deformation, initially indicated by a jump in displacement. **d)** Image taken after indentation test pictured in (c), confirming plastic deformation.

Corcoran et al. [5] investigated the role of orientation of gold single crystals on the instantaneous yielding phenomenon. They were the first to report staircase loading and correlate it to transitions in deformation character. They found the sum total of displacements is conserved, resulting in consistent depths of penetration despite varied loading behavior. They attributed the repeatability of indents to clean surfaces, less than submicron contamination. When a crystal remained exposed to the environment for a prolonged period of time an organic layer forms on the surface. This contamination layer

made the data very sporadic. During the orientation study, all surfaces were freshly flame-annealed to eliminate this problem. The typical yield for the (111) crystal was at mean pressure close to 3 GPa. For the (001) and (110) it was closer to 8.5 GPa. All resolved shear stresses were on the order of theoretical (1.3-1.5 GPa). They had trouble determining if this orientation effect was real, or caused by differences in surface structure. The (111) surface had a large number of single steps that were spaced approximately every 40 nm. These steps were thought to be a source for dislocations because the yield load decreased with their presence. Later Kiely and Houston [6, 64] did a similar study looking at the role of orientation in Au single crystals. They are part of the group at Sandia National Labs that use the IFM technique and coat their samples with a protective barrier. They found the (111) surface to have a 36% higher modulus than the (100) surface, and only a slight difference was found between the (111) and (110) surfaces (3%). Simulations of indentation also predict (111) having the highest indent modulus and (001) having the lowest [6], the difference being the magnitude of the variation. They also found that the yield point varied between surfaces, but the resolved shear stress was consistently around 1.8 GPa for all surfaces. Another point of note was that dislocations might not nucleate at the critical shear stress below the indenter, but rather nucleate at the surface. This may explain some evidence of dislocation activity before the yield point. The fact that both groups found such similar results indicates that the monolayer addition does not significantly influence the excursions. The repeatability in properties also indicates that at different initiation loads the onset of plastic deformation is relatively consistent.

With the increase in computational capabilities, Embedded Atom Modeling (EAM) has become a wide spread tool for modeling indentation behavior. Many groups have tried to model the onset of plasticity to better understand their experimental behavior. As previously mentioned, some groups coat their surfaces to limit the adhesion between the tip and the surface. In modeling, this interaction must also be accounted for or eliminated. In order to model this passive layer, Kelchner et al. [65] used a repulsive potential to represent the indenter tip. Another interesting tool used by this group is the centrosymmetry parameter to identify the coordination number of an atom. An atom with balancing 12 nearest neighbor vectors will have a coordination vector of 0. This will hold even if a material is elastically deformed. A non-zero value will be obtained for atoms in a stacking fault or a partial dislocation. Similar to the IFM studies they are trying to model, they use displacement controlled indentation. They found a dramatic load drop marks the onset of plasticity. Partial dislocation loops first appear at a depth of about half of the contact radius when modeling an Au (111) surface. The loops appeared on two of the three intersecting $\{111\}$ slip planes (regardless of boundary conditions). The loops very quickly grow and intersect the surface, becoming extremely complex in a very short amount of time (picoseconds) even when the tip is held at the yield point. Contrary to initial predictions the nucleation occurs off the indenter axis. The maximum resolved shear stress for the $\{111\}$ slip planes occurs off the indenter axis due to the 71° angle of intersection with the (111) surface plane. The first yield in their simulation occurred at a resolved shear stress of 7 GPa. This is considerable larger than the 2 GPa critical shear stress calculated for bulk Au using the same EAM potential. This indicates there is a problem with the assumptions and estimations for the applied load necessary for plastic deformation.

Rodriguez de la Fuente et al. [66] are the first to report a correlation of size in experimentation and simulation. They report direct scanning tunneling microscopy observations of emission of dislocation half loops near the point of contact during nanoindentation of a thiol coated (001) Au surface. These loops manifest as hillocks or bump like features made up of two stacking faults on intersecting $\{111\}$ planes, bounded by two Shockley partials or v-shaped half loops. They also did embedded atom simulations and found the same defect structure.

Recently Li et al. [67] demonstrated the ability to tie together a number of different scales of simulation with impressive consistency. Looking at the free energy of a volume subjected to homogeneous deformation at finite strain, they were able to define a stability condition for the representative volume that is a function of a polarization vector and a wavevector. The incredible aspect of this model is that it enables you to not only indicate the atom where a dislocation is formed but the burgers vector as well. Their simulations closely agreed with results from a two dimensional bubble raft model both in the location of the dislocation and the slip direction and plane. They were also able to extend their stability analysis to finite element calculations. This demonstrated unprecedented correspondence between molecular dynamic simulations and finite element analysis, in accordance with atomic scale strain to failure criterion. Their molecular dynamic (MD) simulations gave an accurate prediction of staircase loading seen in many metal systems. When indenting on a (111) Al surface, the initial plasticity is caused by subsurface homogeneous defect nucleation on all three $\{111\}$ planes. A similar study done by Kelchner [65] did not observe the same three-fold symmetry in the initial dislocations formed. The difference in dislocation structure could be caused by differences in the simulation methods (MD as opposed to energy minimization), stacking fault energy, or differences in elastic anisotropy. The MD simulations done by Li et al. predict that subsequent deformation is facilitated by the initial glide loops, which interact creating dislocation sources similar to a Frank-Read source. This is consistent with observed behavior that initial deformation requires stresses on the order of gigapascals, while subsequent deformation only requires megapascal stresses. The near surface heterogeneously nucleated dislocations move through the sample to the substrate. Once backstresses caused by dislocation pile-up become too large, any subsequent deformation must occur by the activation of another secondary source on another plane. They qualified any displacement bursts into two categories, major and minor. Minor events are typically about 2 nm, and correspond to a single slip event, while major events are typically larger than 10 nm and correspond to at least 10 consecutive slip events. This study has presented a self-consistent mechanism based explanation for the onset of plastic deformation, covering numerous scales of observation and simulation.

Lilleodden and Nix [68] have shown that the microstructure of the sample can have a considerable influence on the materials ability to bear load elastically. They found that indentations placed near grain boundaries did not display the “pop-in” behavior observed during the indents placed in the center of grains of the same film. The indents near grain boundaries yielded at much lower loads and often did not demonstrate any jumps in displacement. Plastic deformation was common from the onset of loading. In order to confirm that the immediate plasticity is correlated to the grain boundary as a preferential site for dislocation emission and not the result of a reduction in contact area caused by grooving, they performed EAM simulations [69]. The results confirmed that

the grain boundaries do indeed act as a source for dislocation emission, preventing the elastic loading.

Feichtinger et al. [70] has also done some similar studies investigating the role of grain boundaries in nanocrystalline gold. They used atomistic simulations to look at the role of grain size on deformation behavior. They compared samples that contained 12 nm grains, 5 nm grains, and even single crystal samples. They also used two different simulation methods, conjugate gradient (CG) and MD. They found that the methods of simulation have different strengths. The CG method was better at investigating the elastic effects involved in indentation, while the MD simulations were much better at monitoring the intergranular motion that occurred during indentation of the nanocrystalline samples. The MD simulations had very high noise levels due to temperature effects. The displacement controlled indentation simulations using the CG method had load-displacement behavior very similar to IFM experiments, with significant load drops that correspond to dislocation events. The loads at which the yield point occurs are highest for the single crystal and are reduced with grain size. When the isotropic Hertz model is fit to the elastic region of the indentation tests, it results in similar Young's modulus values for both the single crystal and 12 nm grain samples. The value is significantly reduced for the 5 nm grain samples. The load-displacement curves diverge considerably over the plastic portion of the CG runs, demonstrating the significant influence of microstructure on the plastic deformation behavior. They found that the grain boundaries play an important role in deformation behavior, for they act as a sink for dislocations nucleated near the indenter. Grain boundary sliding is especially prevalent when the contact area is larger than the grain. In cases where the grain is larger than the area of contact, deformation is contained within that grain. The initial slip structure in the single crystal samples, consisting of three stacking faults in a nearly tetrahedral geometry, corresponds to the observations of Li et al. [67]. The triaxial symmetry is lost almost immediately with continued deformation. The dislocation interactions are very complex and quickly lead to dislocation lock structures. Feichtinger et al. [y] indicates that the sample geometry as well as the simulation method may be responsible for the discrepancies between Li and Kelchner's observations of initial dislocation movement [67, 65]. Feichtinger et al. point out that the thickness of the aluminum thin films simulated by Li are similar to their 12 nm grain size samples. The free surface may attract the dislocation in a manner similar to a grain boundary. This indicates that the simulation community is still determining the contributions of their boundary conditions. Feichtinger et al. [70] has identified that grain boundaries act as a significant sink for dislocations, especially in small nanograin structures, which can influence their measured mechanical properties.

Kiely, Hwang and Houston [71] looked at the influence of step bunches in the range of 0.5 –3.0 nm on indentation behavior. These tests also utilize coated gold samples to prevent tip interactions during their IFM testing. They observed that the proximity of the indent to surface steps affected the heterogeneous nucleation of dislocations, and therefore the yield stress of gold. When an indent is done directly on a step, the mean stress is 60-70% of that observed in defect free regions. The effect of the step is not confined to the contact area; rather the discontinuity interacts with the stress field well beyond its physical limits. According to their results an indent must be done at least 150 nm from a step edge to not be influenced by that step [71]. If the distance is

normalized by the contact area of the tip, the indent must be made approximately three times the contact radius away from the step in order not to be affected. The resultant plasticity (pile up) from an indent also appears to be on the order of three times the contact radius, indicating there may be a correlation. Indents done away from any surface anomalies had a 100% reduction in load as a result of the excursion, while those near steps experienced a relaxation of only a few %. Attempted calculations using continuum mechanics resulted in unrealistic predictions of subatomic feature; reiterating that our macroscopic theories do not hold at this scale and it is beyond our current understanding. The most important point from this paper is that inhomogeneities, even if they are never in contact with the tip, can nucleate dislocations before the area under the tip has reached critical shear stress. Stress fields extend beyond the plastically deformed region and yield phenomenon is less localized than previously appreciated.

Zimmerman et al. [72] performed atomic simulations to investigate variation in yield initiation in areas with steps. While the simulations did corroborate the finding that the load necessary to nucleate dislocations was significantly reduced due to the presence of steps, the influence was not as large. This could be attributed to change in scale, for the simulated step is only a single atom high. The radius of the tip is also much smaller and idealized. Due to the three-fold symmetry of the (111) surface they chose to indent, two different step orientations were used, $\langle 110 \rangle \{100\}$ and $\langle 110 \rangle \{111\}$. The orientation did change some of the slip systems and therefore the post nucleation behavior, but maintained approximately the same critical resolved shear stress. According to the EAM potential, the critical resolved shear stress for gold should be 3.66 GPa, which is roughly twice the experimentally measured values [5, 6]. One of the major problems with calculations of resolved shear stress both in experimentation and in simulation is the reduction of actual contact area with the presence of steps. The simulations demonstrated that the footprint of the tip for different distances from the step (negative sign indicating the low side) could vary greatly. When the tip is placed directly over a step, only half of the indenter is initially in contact with the surface. At a position below the step, the load is initially born by just a few atoms on the step edge. The Hertzian expression for contact area is not applicable. The biggest reduction in nucleation load occurs when the ratio of distance from the step edge over contact radius is below 1.5, with the most severe difference being below 1. The step acts as a stress concentration. In the presence of a step the planes of dislocation propagation also change. Simulations indicate the slip occurs in $\langle 112 \rangle$ direction, for $\langle 110 \rangle$ dislocations often split into two $\frac{1}{2} \langle 112 \rangle$ partials. An interesting point was that the slip did not occur in the direction of highest resolved load, but rather in the direction of lowest unstable stacking fault energy. One important difference in the simulations is that the load only dropped 30-40% upon dislocation nucleation compared to the complete relaxation experienced in experimental trials. The model showed the load drop was reduced to 15% in the presence of a step, and on some occasions, dislocation movement was only indicated by a change in slope. This is much less severe than experimental results but does correlate qualitatively. It is apparent that surface structure has a longer-range influence than just on top of a step. Zimmermann calculated that due to the angle of incidence and the step height, the indenter is most likely still hitting the step even at distances that were thought to be out of reach during experimental trials. The surface structures being considered in all of these experiments are all very small, at or below the resolution of the Triboscope system.

2.3.2 Electrochemistry

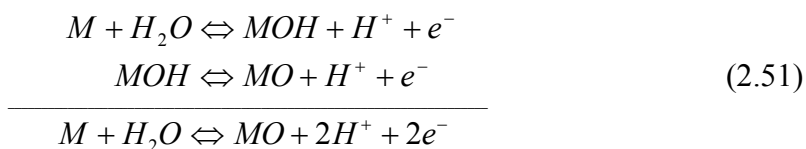
One of the main reasons we chose gold as our sample material was its electrochemical properties. Gold has no natural oxide and therefore no complications due to rupture during indentation testing nor any epitaxial stresses. A stable oxide can be induced under certain conditions, enabling the influence of the oxide to be easily identified. Gold in the presence of ions of silver or lead experiences a phenomenon called underpotential deposition, where a single monolayer of the other element is deposited on the surface. Gold has well known sample preparation techniques, developed for in-situ STM studies of electrochemical growth processes. These techniques enable surfaces with atomically flat terraces on the order of 100's of nanometers in width. The flat surfaces of gold, combined with its stability in acid and its ability to grow very discrete and controlled monolayers made it an ideal system to characterize the role of surface modifications on indentation data.

Linear sweep voltammetry is a common tool in the electrochemical field because it can be very sensitive, enabling characterization and resolution of sub-monolayer processes. This technique has been very valuable in identifying multiple-state absorption reactions. Cycling the voltage allows exploration of reversible reactions, both the deposition and dissolution. The oxidation and underpotential processes discussed in this section will be described in terms of the reactions observed in the cyclic voltamograms. The electrolyte used can influence the reactions that occur. We will be concentrating on perchloric acid, for it is the anion least absorbed on a gold surface.

2.3.2 a Gold Oxidation

Metal oxidation begins with submonolayer processes that are very sensitive to applied voltage. Studies have indicated that oxidation is highly influenced by surface orientation and the electrolyte anion [73]. The surface orientation influences the geometry and density of adsorption sites. The electrolyte is important because the way in which the anion adsorbs on the surface can dramatically influence subsequent reactions.

Typically a two electron oxidation process has two steps:



The parallel orientation of the MOH dipoles experience considerable repulsive interactions. The repulsion causes the surface to reconstruct and form an antiparallel orientation in what is termed a turn over process [74]. This creates a two atom thick ordered precursor layer to bulk oxide growth. The turnover of the anions causes the separated peaks observed on deposition of each sublattice to form one peak during the

reduction process. The change in the MOH state causes a hysteresis in the processes of oxidation and reduction.

The crystal symmetry of a surface can create different energy requirements for the first stage of this electron transfer. This results in the creation of sublattices of the chemisorbed oxide surface dipole (MOH) [75]. The sublattice spacing is dictated by the short range repulsive forces and long range attractive forces through the metal. The anions of the electrolyte also play a crucial role in surface oxidation. Different species (ClO_4^- , SO_4^{2-} , F^-) have different degrees of adsorption. Anion presence on a surface hinders subsequent reactions.

The (111) plane of an FCC metal is a closest packed plane, meaning it has the highest surface atom density and trigonal symmetry. Electrolyte anions, such ClO_4^- , are also tetrahedral. The distance between the centers of gold surface atoms on a (111) plane is 0.288 nm [76], which is very similar to the oxygen spacing of 0.236 nm for ClO_4^- [73]. This results in strong compatibility between the gold atoms and the anions. The number of atoms in 1 cm^2 of ideal surface is 1.39×10^{15} . This is important for it allows us to determine the charge required for one electron transfer per square centimeter. For gold this corresponds to $222 \mu\text{C cm}^{-2}$.

On gold (111) there are three sublattices that equally make up the first monolayer. The different energy requirements enable the separation of each reaction when the voltammetry is linearly increased. Even at low acid concentrations the first two sublattices typically only account for approximately 17% of the surface (compared to the theoretical 67%). This dramatic reduction is caused by the adsorbed ClO_4^- anions on the surface that inhibit OH deposition. Even when the third sublattice is deposited the total coverage is about 73% of a monolayer, or $162 \mu\text{C/cm}^2$ [73]. The fourth peak tends to correspond to the deposition of more than a single monolayer of oxide.

A cyclic-voltamogram is a plot of the changes in current as the potential is cycled. These changes in current indicate reactions occurring within the cell. **Figure 2-19** is a cyclic-voltamogram of a gold (111) surface in a 0.1 M HClO_4 electrolyte. The potential is cycled between -0.4 and 1.05 V vs. a platinum counter electrode at a rate of 10 mV/second. As the voltage is increased an oxide is formed on the gold surface. Observe that there is an indication of multiple peaks in the region of 0.5 to 0.8 V. These correspond to the different sublattices being deposited. Upon changing scan directions the oxide is eventually reduced, as indicated by the peak at 0.28 V. Cyclic-voltametry is very dependent upon scan rate. If the surface were scanned at a faster speed the peaks would sharpen. A faster scan rate might facilitate the separation of each of the three sublattices that make up the first electron transfer. As the voltage is increased a bulk oxide begins to form. This oxide, like any bulk deposition process would proceed indefinitely at a potential above a critical level.

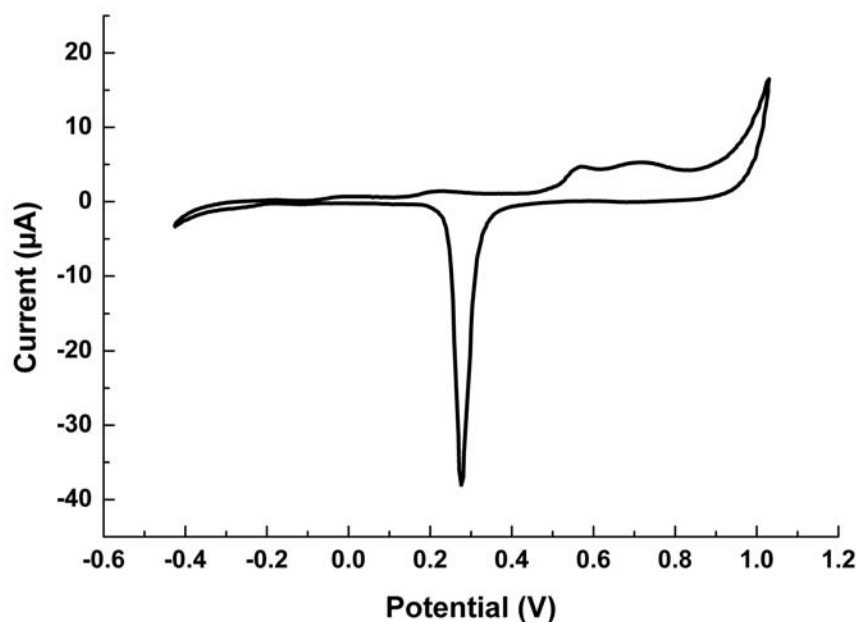


Figure 2- 19 Cyclic Voltammogram of gold (111) surface in 0.1M HClO₄, scanned from -0.4 to 1.05 V versus a platinum wire counter electrode. The peaks at positive current densities correspond to the deposition of a lead oxide, while the peak at negative current densities corresponds to the stripping of the induced oxide. The hysteresis in voltage is due to the turnover of the MOH dipoles.

2.3.2 b Under-potential Deposition

Underpotential Deposition (UPD) is the deposition of submonolayers and monolayers of one metal on the surface of another at potentials higher than that predicted for bulk deposition by the Nernst Equation. This phenomenon only occurs with certain metal pairs. An example is an electrochemical cell with gold as the working electrode and lead ions in solution. A potential value of zero corresponds to the reversible Nernst potential (E_r) for the reaction $\text{Pb} \leftrightarrow \text{Pb}^{2+} + e^-$ defined by:

$$E_r = E_o + \frac{RT}{nF} \ln \left(\frac{a_{\text{Pb}^{2+}}}{a_{\text{Pb}}} \right) \quad (2.52)$$

E_o is the standard Nernst reversible potential, R is the ideal gas constant, T is the absolute temperature, n is the valence state of the ion, F is the Faraday constant, $a_{\text{Pb}^{2+}}$ is the activity in the electrolyte and a_{Pb} is the activity of bulk metal which by definition is equal to one. At potentials negative to E_r , the reduction reaction ($\text{Pb}^{2+} + e^- \rightarrow \text{Pb}$) is favored and bulk deposition occurs. Above E_r the oxidation reaction ($\text{Pb} \rightarrow \text{Pb}^{2+} + e^-$) is favored and any deposited lead will be stripped. Typically, with an “inert electrode,”

there is no reduction reaction above E_r . This is not the case in underpotential deposition, where due to a strong attraction between the ions in the electrolyte and the working electrode, monolayer quantities of deposition occur at positive potentials to the Nernst potential. **Figure 2-20** is a cyclic voltammogram (C-V) of the underpotential region of this system. Starting at the middle of the figure at a voltage of approximately 1V, if the potential is increased, the gold surface will begin to oxidize, indicated by the increase in current. At a maximum potential of 1.85 V vs. a platinum wire counter electrode, the direction is reversed. There is a hysteresis in the stripping of the oxide caused by the antiparallel orientation of the oxide dipoles. At approximately 1.3 V the oxide is stripped from the gold surface. As the potential is further reduced we enter the under potential region. At 0.4 V the lead begins to deposit on the surface. Bulk deposition, indicated by the line at zero volts, occurs at or below (more negative to) the reversible Nernst potential. If the potential were held below the Nernst potential the deposition reaction would continue indefinitely. When the potential is cycled above the Nernst potential the lead will be stripped off the surface. In this c-v the stripping of the sublattices of lead are apparent by the multiple positive current peaks.

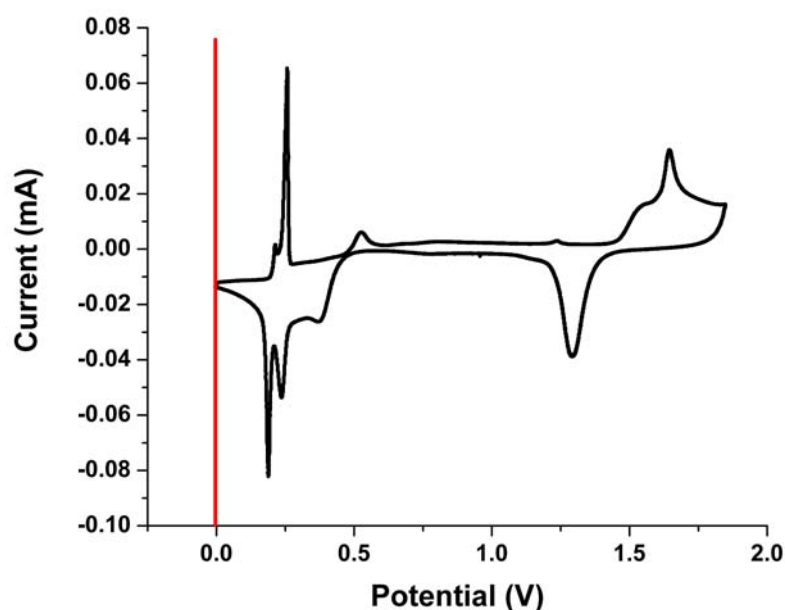


Figure 2- 20 Cyclic Voltammogram of a gold (111) working electrode in a 1.0 mM $\text{Pb}(\text{ClO}_4) + 0.1 \text{ M HClO}_4$ electrolyte, scanned from 0.01 V to 1.85 V vs. platinum wire counter electrode. Bulk deposition is indicated by the line at zero volts. The peaks at potentials above this line indicate the depositon and stripping of a lead monolayer on the surface.

UPD is caused by the interactions between the substrate and the metal ions in solution. The metal ions are repulsed from one another and attracted to the substrate. This indicates that the process will be influenced by the presence of other ions on the substrate surface, leading to a modified Nernst Potential [77]:

$$E = E_{o,Me/Me^{n+}} + E_a + \frac{RT}{nF} \ln \left(\frac{c_{Me^{n+}} \cdot f_{Me^{n+}}}{\Theta \cdot f_{Me}} \right) \quad (2.53)$$

Where $c_{Me^{n+}}$ is the concentration of metal ions, Θ is the amount of coverage, and f_{Me} = activity coefficient of monolayer. E_a accounts for metal/substrate interactions, meaning the difference in the potential of UPD of Ag on Au as opposed Pb. This new monolayer creates a lattice that is much less dense than that of the substrate. The sublattices of different energy requirements are evident in the C-V in Figure 2-20. As you get closer to the Nernst potential, the monolayer will continue to fill in and start to match the substrate in density. These deposits are reversible and will be stripped in the same manner with rising potential. Unlike bulk deposition, that continues at a constant potential at or below the Nernst, when potential is held constant in the UPD region the monolayer will form and the current goes quickly to zero. Thus, UPD is considered a potential dependent process [78].

UPD is of interest not only for theoretical understanding, but also for metal deposition processes. UPD exhibits well-ordered two-dimensional growth, as opposed to the often three-dimensional growth exhibited in bulk deposition. The growth of the bulk is hypothesized to be influenced by the structure of the UPD layer. Through an understanding of the adlayer behavior, important clues about surface chemistry and physics can be obtained. UPD can also give us a better comprehension of binding energy determinations, the initial steps of electrocrystallization, electrocatalysis, semi-conductor metallization, or chemisorptions, in general. Through the investigation of such behavior on single crystals, exact thermodynamic, kinetic, and structural behavior can be more accurately quantified and detailed. Ultimately, in depth knowledge of the factors that facilitate and influence such sorption and nucleation processes will allow us to manipulate structures of certain deposited metals for engineering applications.

UPD may have first been noticed in 1912 by Hevesy [77]. He found small amounts of radioactive metals were adsorbing on the surface of copper at potentials several tenths of a volt above those predicted by the reversible Nernst Potential. Herzfelt followed with theoretical explanation of why this was happening using variation of activity and surface coverage. In the late 40's many groups including Rodgers et al. looked specifically at stripping and depositing small amounts of metal, namely radioactive Au and Cu. They investigated effects of numerous substrates, ion concentrations and electrolytes. The majority of this work looked at how this phenomenon affected bulk properties. It was not until the late 60's and early 70's that UPD was studied exclusively. Studies were initially done on polycrystalline systems and then slowly progressed to single crystals to analyze specific behaviors more carefully. All single crystal studies have been conducted on low index planes [(111),(110),(100)] of fcc single crystals [79].

In the 1980's there was a large resurgence of efforts due to the invention of the Atomic Probe microscopes. This enabled people to see images of atoms and their structure for the first time. With these investigations came development of small-scale electrochemical cells to allow scientists to observe reactions as they occur. This facilitated documentation of *in situ* growth for the first time. UPD is dependent upon many factors. Only certain systems work because the substrate must be stable and

reversible in the underpotential region. This means that the UPD has a very limited range. Ramping the potential too high could cause oxidation of the surface and then pitting damage. By bringing the potential too low, into bulk deposition, it is possible for your metals to start to alloy. This would damage the surface and result in curves that are no longer repeatable.

Since UPD is caused by the strong interactions between the substrate and the adatom, it is understandable that the crystallographic orientation should have dramatic effects on the monolayer structure. The orientation direction directly affects the number and location of near neighbors in the monolayer. The crystallographic orientation of your substrate also determines the spacing or packing of your substrate atoms and therefore the shape and size of the sites available for deposition. The structure of a substrate dictates a great deal about the C-V plot; the number of peaks, the potentials, the half widths, and the amplitudes.

Charge transfer is the only way to monitor the amount of metal that is being deposited the uniformity of the layer is questioned. Before the invention of electrochemical scanning tunneling microscope (ECSTM), one of the methods used to ensure uniform dispersal was to monitor Hydrogen adsorption. It is well known that prior to Hydrogen evolution, H_2 adsorbs on the surface of Platinum, and it is also well known that hydrogen does not adsorb on the surface of many of the UPD metals, such as Cu and Ag. The adsorption of hydrogen was linearly reduced by the increase in ion deposition. The degree to which the adsorption is suppressed is highly dependent upon the size of the ion. A full monolayer completely suppresses hydrogen adsorption, indicating uniform coverage.

Experimental parameters are closely linked with the C-V curves received. There are dramatically different shapes of the C-V curves depending on electrolyte [73]. This difference occurs because of the interactions and adsorptions of the different ions in the electrolyte. Metal ion concentration will cause the curve to shift according to the Nernst equation, i.e. 60mV per decade. Surface roughness and therefore exposed surface area affects the size of the peaks due to the increased number of absorption sites. These UPD systems are also very sensitive to contaminants. Depending upon the time of air exposure, the clarity of the curves can be greatly affected due to adsorbents on the surface. Optimum detail can only be obtained when a sample has been freshly flame annealed or recently removed from the vacuum chamber (24 hours). Otherwise, these contaminants can “mask” important reactions that may be occurring. In addition, the scan rate can alter the shape and size of the peaks in your C-V plot. Only through integration of the peaks can you determine the charge exchanged in the deposition. A faster rate produces a bigger peak because the same amount of charge occurs in less time. However, when you scan at a faster rate it allows more room for error and potentially enabling a masking effect.

The area under the curve is integrated to determine the charge transfer. C-V graphs are not just measures of fluxes of the adsorbed UPD species; they have contributions from the non-Faradaic reactions of the non-steady state UPD processes. One of the disadvantages is that the concentration must be calculated which means that you must make a number of assumptions about charge transfer and electroadsorption valancey.

Isolated study of the underpotential region will enable better understanding of mechanisms that affect monolayer deposition, which in turn may affect bulk deposition. Only through complete understanding will we be able to consistently modify surfaces for engineering applications. Future work needs to be done to evaluate the influences these monolayers have on material properties. Areas of potential application are in specialty coatings and electronics instrumentation. Only through understanding of the mechanisms and the effects of deposition will surfaces be efficiently engineered to obtain the desired properties.

CHAPTER 3: EXPERIMENTAL

All experiments were done on 10 mm diameter by 2 mm thick Au (111) single crystals, 99.99% pure, purchased from Monocrystals Inc. Gold was chosen as a model material because it is a well characterized FCC metal. Gold is also a noble metal and therefore has no natural oxide layer. A single crystal specimen eliminates grain boundary issues. Gold also has a number of electrochemical advantages, which were of primary importance at the onset of the study. Surface preparation techniques that enable the growth of surface terraces on the order of hundreds of nanometers are well known from work done in the electrochemical field.

3.1 Surface Preparation

There are three stages to the surface preparation of gold, mechanical polishing, electropolishing and flame annealing. Starting with the most macroscopic, the crystal is mechanically polished by hand, using alumina paste and soft cloth for precious metals. Depending upon the state of the surface, the powder size starts as high as 5 micron and always ends with a 0.05-micron polish. A specialized fixture, shown in **Figure 3-1**, is used to maintain the crystal orientation. A tungsten carbide ring ensures planarity and resists wear. A micrometer at the top of the fixture enables control over the amount of material removed. Typically we remove of approximately 25 μm . Embedding of particles can be a significant problem, so after each stage of mechanical polishing, the crystal is soaked in a potassium hydroxide solution (1N KOH) to ensure that all the alumina is removed. Gold is stable at this pH, but alumina is dissolved in the solution. The crystal is then washed with 18 M Ω de-ionized water and dried. **Figure 3-2 (a)** is a surface image taken with STM of a mechanically polished surface.

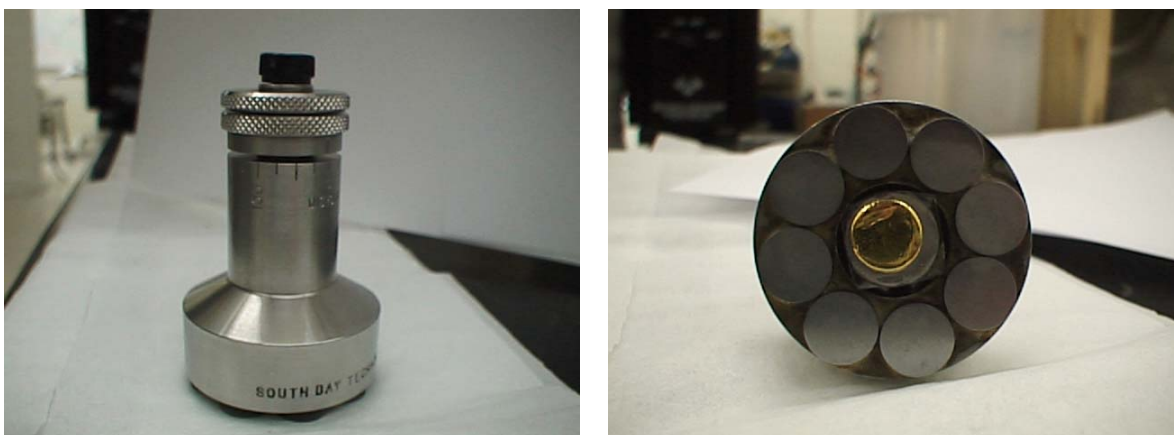


Figure 3- 1 Specialized polishing fixture used to maintain crystal orientation. The fixture has tungsten carbide feet to resist wear and maintain a planar surface and a micrometer at the top to monitor the amount of material removed.

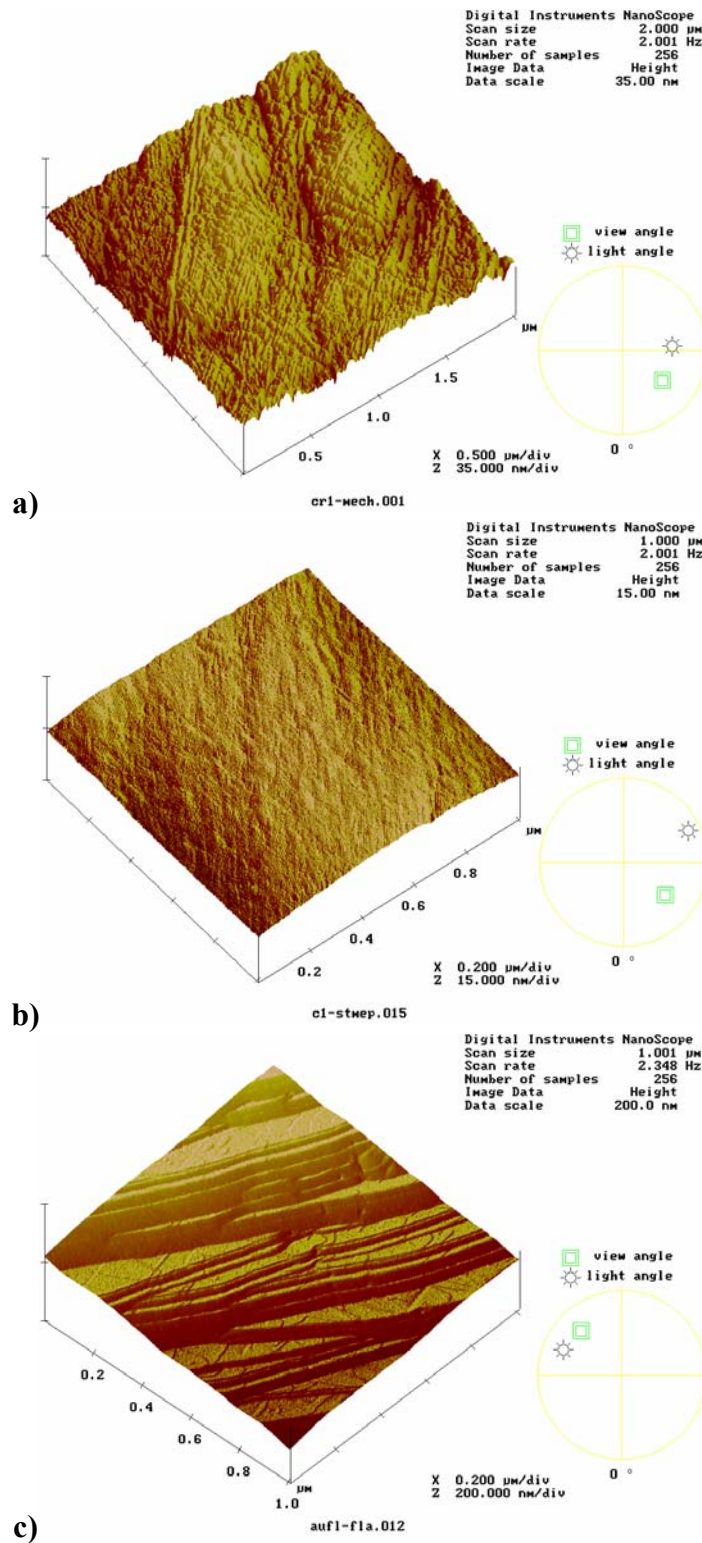


Figure 3- 2 Surface images taken with STM at various stages of surface preparation, all $1\mu\text{m} \times 1\mu\text{m}$.
a) Surface that has been polished with $0.5\mu\text{m}$ alumina paste **b)** Surface that has been mechanically polished and electropolished for approximately 45 seconds **c)** Surface that has been mechanically polished, electropolished and flame annealed for 15 minutes.

Next the crystal is electropolished in a two-electrode cell, with a platinum cathode. The electrolyte of 2.5 Ethylene Glycol: 1.5 Hydrochloric Acid. The solution is heated to 55-60°C. A voltage is applied using an Agilent DC power supply. The initial voltage is set to 10 V, and adjusted as necessary to ensure a good surface. Good surfaces are highly reflective and are detected by visual inspection. Depending upon the surface appearance, additional time may be needed. For example if the surface is slightly cloudy the voltage may be increased. The electropolishing step takes a minimum of 20 seconds. An image of the surface taken with STM is shown in **Figure 3-2 (b)**.

The third step is flame annealing. The flame annealing technique is used extensively in the electrochemical STM community to produce clean Au surfaces, better than submonolayer contamination, with atomically flat terraces of several 100 nm in width. A hand held ultra high purity hydrogen (99.99%) torch is used to heat the crystal until it reaches a yellow glow, just prior to melt (approximately 1000 °C). The maximum temperature is achieved by visual inspection of the color. This temperature is maintained for a minimum of approximately 5 minutes. Typically the crystal is allowed to room cool on a ceramic refractory brick. A STM image of the surface after flame annealing is shown in **Figure 3-2 (c)**. The crystal is flamed immediately before each set of indentation experiments, unless otherwise indicated, to ensure a clean surface.

As part of the investigation into the role of some of the preparation parameters the cooling rate of the crystal was varied in an attempt to change vacancy concentrations. The highest vacancy concentration was produced by the fastest cooling rate. After the designated duration of flame annealing was finished, a flow of nitrogen was used to quench the crystal. The intermediate vacancy concentration was produced by letting the crystal air cool on a refractory brick. The cooling rate is relatively rapid because of the large heat sink. The low concentration was achieved by an extended stepped anneal in a furnace that was purged with Argon. The cooling profile for the anneal is given in **Figure 3-3**.

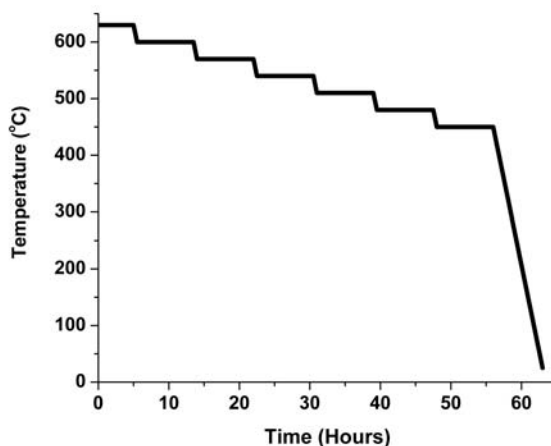


Figure 3- 3 Annealing profile used to reduce the vacancy concentration in the gold single crystal. Anneal was performed in a furnace purged with Argon. The total duration of anneal is 63 hours.

3.2 Nanoindentation

All nanoindentation experiments were conducted using a Hysitron, Inc. TriboScope ®, as an attachment to a Digital Instruments Nanoscope III SPM. One of the main advantages of the Hysitron system is the ability to image before and after indentation, using a specially designed force transducer and the AFM imaging software. The indenter tip is used as the imaging probe in contact mode. The imaging capabilities make it possible to indent on specific surface features, and avoid any sites with deformation due to a previous impact. This also enables post indent imaging that facilitates identifying the relative location of the indent. It is also a fully quantifiable system. The indentations were done using electrochemically etched W tips and Berkovich Diamond indenters. The instrumentation was calibrated in the manner described in Section 2.1.

All indentation tests had a loading cycle of 10 seconds, a hold at maximum load for 5 seconds and a 10 second unloading duration. All indents, unless otherwise indicated, had a maximum load of 100 μN . The set point for imaging of the gold surface was 0.8 nA, which is equivalent to 800 nN. All hardness values were derived by the Hysitron software, utilizing the equations detailed in Chapter 2. The yield point determinations were determined from identifying the initial change in loading behavior for each indent.

3.3 Electrochemistry

All glassware was cleaned in a standard $\text{HNO}_3 + \text{H}_2\text{SO}_4$ cleaning solution at 60°C, followed by one hour of rinsing in 18 M Ω water. The cyclic voltammetry was carried out with electrochemical cells specifically designed for the Digital Instruments Microscopes. The configuration for the electrochemical cell used in this study is shown in **Figure 3.4**. The cell has an exposed working area of 0.59 cm². Experiments were performed in an electrolyte of 1.0 mM Pb (ClO_4) + 0.1 M HClO_4 . The reagents are Alderich Gold Label. Solutions were prepared with ultra-high purity 18M Ω deionized water, from a Barnstead e-pure system. The reference electrode was a lead wire and a platinum wire was used as a counter electrode. All potentials for the CV are given with respect to open circuit. In the investigated potential range investigated deaeration of solutions was unnecessary. The electrochemistry was controlled by Gamry Instruments potentiostat, model DHC1. The range of voltage, scan speed, and surface area are input in to the software. The time, applied voltage and current are recorded and can be subsequently plotted in any combination.



Figure 3- 4 Electrochemical cell developed for use with Digital Instruments Electrochemical STM. The exposed area is 0.59 cm^2 . The gold crystal is the working electrode, reference electrode is a lead wire and the counter is a platinum wire. The screws hold the electrodes in place and are the leads to connect to the potentiostat. The base of the cell measures approximately 20 mm.

CHAPTER 4: RESULTS AND DISCUSSION

4.1: Initial Testing

4.1.1 Preliminary Results

Indentation tests are sometimes referred to as “material fingerprints,” for each material behaves slightly differently. As with any good characterization tool, indentation tests should enable differentiation. Hardness tests are used for quality control, to ensure material is consistent and uniform. Inherently some materials behave in a more repeatable manner than others.

Figure 4-1 (a) is a series of indentation tests done on fused quartz, with a Berkovich diamond indenter. The four indents are done at the same load on two different days of testing. The consistency of the results is what we would expect for a model system and demonstrates the repeatability the instrumentation is capable of. **Figure 4-1 (b)** is a series of indentation tests done on the same gold (111) surface with a tungsten indenter. There are two features of the indentation tests on gold that are a marked contrast to the fused quartz, the discontinuous loading curves and the large variation in depth of penetration. The amorphous structure of fused quartz deforms uniformly, evident by the smooth loading curve. The gold experiences staircase loading; repeated elastic loading followed by events of plastic deformation. The fused quartz has a very consistent and repeatable displacement behavior. The four indents on the gold surface differ in the maximum depth of penetration by over 30 nm. This is a surprising result because the samples are well-prepared (electropolished and flame annealed) gold single crystals, selected to be a model system for surface modifications. The irreproducible behavior makes any intended subtle surface changes indistinguishable.

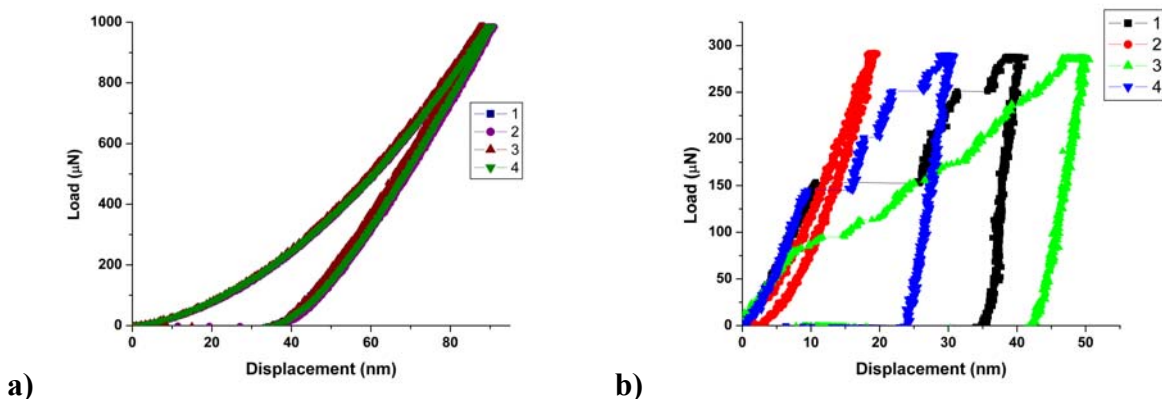


Figure 4- 1 a) Four load-displacement curves done by a diamond Berkovich indenter on fused quartz taken on two different days, demonstrating the consistency that is anticipated in this form of material testing. **b)** Four load-displacement curves done by a tungsten tip on the same gold (111) surface under identical conditions, demonstrating considerable variability in the mechanical behavior on what should be a consistent surface.

The differences in behavior for the fused quartz and the gold surfaces highlight the two main aspects of the indentation tests that we are concerned with: the initiation of plasticity and the overall deformation. Many materials experience discontinuities in the loading curve for a variety of reasons (oxide breakthrough, phase transformations, dislocation formation). In gold these displacement jumps are attributed to the formation and motion of dislocations, as discussed in Chapter 2 Section 3. If the load is removed prior to the first displacement jump there is no indication of plastic deformation. The load at which the first displacement event occurs is therefore termed the yield load. This load can be used in **Equation 2.12**, to determine the maximum shear stress (τ_{\max}) required to initiate plastic deformation. The calculated shear stress can then be compared to the theoretical shear stress for the motion of one plane of atoms relative to another. This will give a general indication of the quality of the structure. The amount of plasticity, and therefore the displacement of the indenter, is used to determine a material's hardness. The maximum depth of penetration is used to calculate the hardness, and can therefore be an indicator for the mechanical property. All indentation testing will be discussed in terms of the two points taken from the load displacement data, the yield load and the maximum displacement, and the property values calculated from those points, the maximum shear stress and the hardness.

Beside hardness the most commonly reported property value determined from load-displacement data is indentation modulus. (The equations and the assumptions involved with these property calculations are discussed in Section 2.1.2.) The modulus is related to the unloading slope and is very sensitive to any changes in slope caused by creep. Gold experiences creep, or continued displacement at a static load. It can be observed in tests by continued deformation during the hold at maximum load. If the creep is significant enough it can even result in negative unloading slope, giving very unrealistic modulus values. The contribution from creep is typically cited as the reason for inconsistencies in measured modulus values. The modulus of gold will not be reported because isolating the influence of creep in these tests is beyond the scope of this project. We would expect, and for the most part observe, a modulus near the experimental polycrystalline value (78 GPa), due to the fact that the induced stress field is hemispherical and not uniaxial. It should also be noted that this is considerably less than the theoretical modulus for Au [111] which is 116 GPa [80].

Initial tests were often run without extensive imaging before and after indentation testing of the surface because of the time required to do so. One of the initial theories for the wide variation in material response was the role of surface structure. **Figure 4-2** is a representative Scanning Tunneling Micrograph of a gold (111) surface. The height scale is 30 nm, and the x and y-axes are both 2 μm . The step bunches in this image are nominally 5 nm. From this image it is easily imagined that the measured displacement would be different if the tip landed on a flat portion (often referred to as a terrace) or on a spot that included steps. The response would also be dependent upon the relative size of the step and the tips relative proximity. The imaging technique (STM) used to acquire **Figure 4-2** has very high resolution; even atomic sized steps are distinguishable. The tunneling current between the surface and the tip is exponentially related to the distance between them. Therefore this technique is very sensitive to surface features in conductive materials. The in-situ imaging of the Hysitron transducer utilizes contact

AFM, so the tip rides along the surface and its resolution is a function of the size of the probe. In indentation testing the tips are very broad by AFM standards, decreasing the resolution capabilities even further. The tungsten tips used in our experiments were fabricated with tip radii between 50 nm and 1 μm . The Berkovich indenter we use has a radius of approximately 325 nm. The large tip radius and the instrumentation noise make it difficult to resolve certain surface features even when extensive before and after imaging is done. The resolution is adequate to enable indents to be intentionally placed on surface features that are over 0.5 nm in height but not single atomic steps. Occasionally indentation tests were performed on features in order to investigate their influence. The results of such tests are discussed in the context of all the indents performed on that surface.

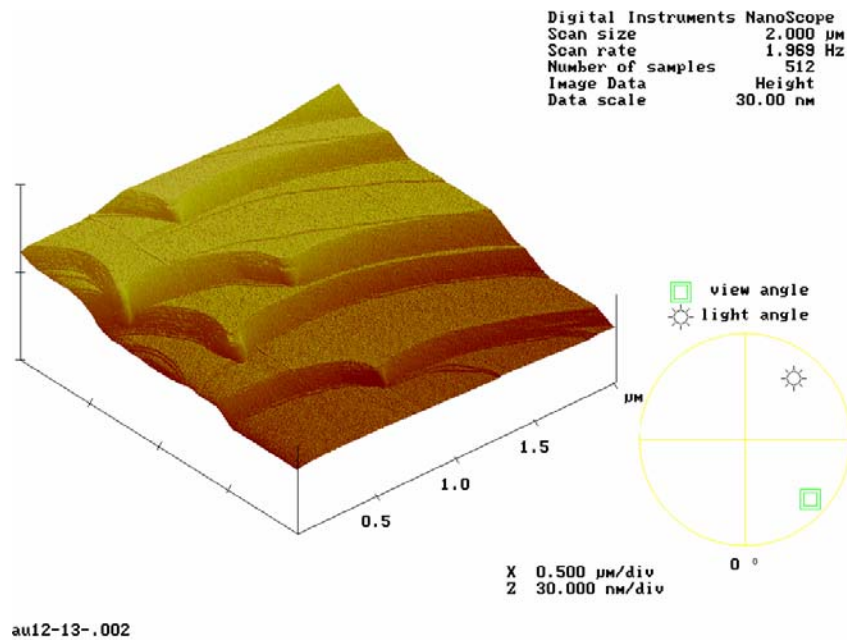


Figure 4- 2 Scanning Tunneling Micrograph of a gold (111) surface. The x and y-axis are 2 μm . The total height pictured is 30 nm. Each of the step bunches is approximately 5 nm in height.

The load displacement data recorded for a tungsten probe tip on a gold (111) surface during a single day of testing is plotted in **Figure 4-3**. Some of the important measurements from the indentation data are recorded in **Table 4-1**. The data displays very high loads required to permanently deform the material. The average yield load was 93.0 μN , with a standard deviation of 64.0 μN . This is a huge variability in the ability bear load elastically. The point at which the material yields does not appear to have a significant influence on the remainder of the deformation behavior. Unfortunately the tip was destroyed before its radius was measured, which is a necessary parameter in calculating the maximum shear stress. Using the idealized reduced modulus and fitting the elastic portion of the curve, an approximate radius was determined to be 500 nm. This results in maximum shear stresses (τ_{max}) at yield in the range of 1.3 to 3.2 GPa, which agrees with the results from other tips. This is also in the range associated with theoretical yield strengths, indicating that the structures being indented are nearly ideal.

The depth of penetration has an average value of 55.5 nm with a standard deviation of 6.2 nm. The total difference between the maximum and minimum depth is 22.1 nm. The difference is over 32 % of the deepest penetration depth. This is a large variation in deformation behavior for what should be a well behaved system. The tip used in these experiments was made of tungsten, and the typical calibration methods for diamond indenters would damage the tip. This means that there is no well defined tip area function, and therefore no hardness calculations. The variability in the maximum depth of penetration indicates an equally large variation of hardness values. All indents appear to have similar extent of creep, indicating this does not play a role in the final depth of penetration. While the modulus has not been calculated, all indents seem to have the similar unloading slopes, indicating the same degree of elastic recovery. In an attempt to look at the change in response based on structure, indents were placed on different surface elements, some indents were made on terraces and some were made on step bunches. The purpose was to investigate if there was a correlation between the structural aspects and the final depth of penetration. The flat locations had surface features less than a nanometer in height. The steps ranged from 3 to 15 nm. There was no consistency in the results for features of the same size and no trend in larger features having more of an influence on displacement than smaller features. There was no apparent correlation between the yield loads or the surface structure and the observed displacement. There is no obvious cause for this variability in mechanical behavior.

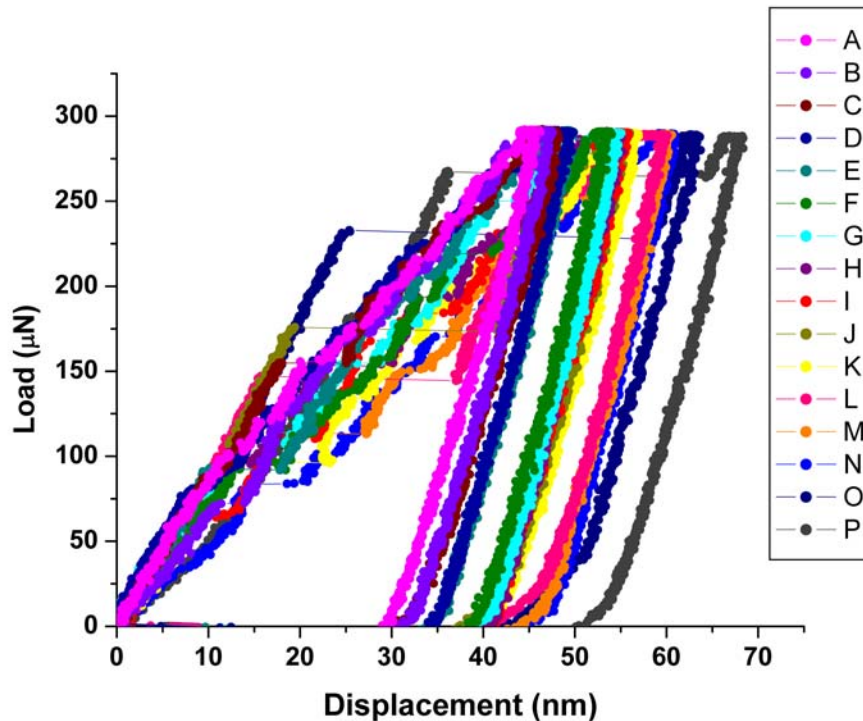


Figure 4- 3 Load-displacement data for a tungsten tip on a gold (111) surface. This demonstrates the tremendous variation measured on a single surface in one day of testing. The final displacement does not seem to correlate to the yield point, surface structure, or extent of creep at hold.

Indent	Yield Load	τ_{\max}	Max. Depth
	(μN)	(GPa)	(nm)
A	29.1	1.62	46.2
B	72.4	2.19	47.6
C	16.7	1.34	48.2
D	27.7	1.59	49.8
E	91	2.37	49.9
F	51.6	1.96	54.0
G	33.7	1.70	55.1
H	64.9	2.11	55.2
I	63.5	2.10	55.9
J	175.3	2.94	56.0
K	96	2.41	56.9
L	146.8	2.78	60.1
M	113.9	2.55	60.6
N	33.7	1.70	61.0
O	232.3	3.23	63.7
P	175.6	2.95	68.3
AVERAGE	93.0	2.26	55.5
Stand. Dev.	64.0	0.56	6.2

Table 4- 1 Important values for indentation tests shown in Figure 4-3. Yield load is the point at which plastic deformation begins, indicated by a displacement jump or change in loading slope. The maximum shear stress (τ_{\max}) is calculated from the yield load and indicates the shear stress required to initiate plastic deformation at the location of the indent. The maximum depth of penetration (h_{\max}) is the displacement at the end of the hold at maximum load. The maximum depth is used in hardness calculation. Due to the fact that this was a tungsten tip, we were unable to get an accurate tip area function and therefore have not reported hardness values.

The same irreproducibility was apparent when using a diamond indenter, as shown by the load-displacement data plotted in **Figure 4-4**. All of these indents were done on the same gold (111) surface during a single day of testing. The tip was a diamond Berkovich indenter that has a well characterized tip area function. The yield load and the associated maximum shear stress at yield are shown in **Table 4-2**, along with the maximum depth of penetration and hardness values for each indentation test. The yield points range from 5.2 μN to 92.9 μN , with corresponding spread in τ_{\max} of 1.3 GPa to 3.4 GPa. Again these values are on the order of theoretical estimations of the shear stress required for dislocation formation. The average yield load for this set of experiments was 27.8 μN , with a standard deviation of 25.6 μN . The enormous standard deviation demonstrates the dramatic disparity in different locations ability to sustain load elastically. There is also considerable variation in the total displacement of each test. The average maximum depth of penetration is 25.6 nm with a standard deviation of 5.0 nm. The total variation is over 16 nm for depths that range from 18.4 to 34.0 nm, another considerable discrepancy. These tests have an average hardness measurement of 2.05 GPa, with a standard deviation of 0.62 GPa. The total range of hardness values is 1.2 to

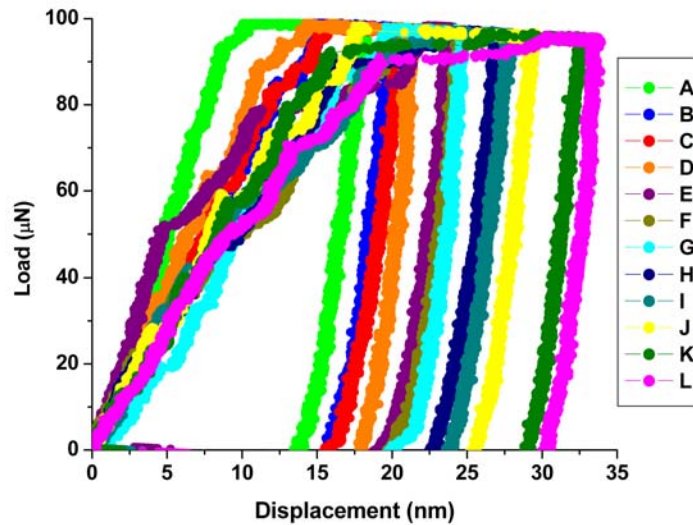


Figure 4- 4 Load-displacement data for a diamond Berkovich indenter on a gold (111) surface. This demonstrates the tremendous variation measured on a single surface in one day of testing. The final displacement does not seem to correlate to the yield point, surface structure, or extent of creep at hold.

Indent	Yield Load (μN)	τ_{max} (GPa)	Max. Depth (nm)	Hardness (GPa)
A	92.9	3.43	18.4	3.28
B	6.9	1.44	20.4	2.79
C	5.2	1.31	20.8	2.62
D	34.2	2.46	21.6	2.38
E	60	2.96	24.2	2.12
F	20.4	2.07	24.9	2.01
G	6.5	1.41	25.1	1.94
H	20.8	2.08	27.2	1.75
I	32.5	2.42	28.1	1.66
J	26.2	2.25	29.8	1.54
K	13.5	1.80	33.0	1.31
L	14.9	1.86	34.0	1.21
AVERAGE	27.8	2.12	25.6	2.05
Stand. Dev.	25.6	0.64	5.0	0.62

Table 4- 2 Important values for the indentation tests shown in Figure 4-4. Yield load is the point at which plastic deformation begins, indicated by a displacement jump or change in loading slope. The maximum shear stress (τ_{max}) is calculated from the yield load and indicates the shear stress required to initiate plastic deformation at the location of the indent. The maximum depth of penetration (h_{max}) is the displacement at the end of the hold at maximum load. The maximum depth is used in hardness calculation. Hardness is a common property measurement used to compare materials resistance to deformation.

3.3 GPa. There is a difference of over a factor of two between the shallowest indent and the deepest in comparing the depth of penetration and the calculated hardness. The variation in the depth at yield does not correlate to the variation in final depth of penetration. **Figure 4-5 (a)** shows two indents that yield at nearly the same load, but have significantly different depths of penetration. **Figure 4-5 (b)** show two indents that have similar resultant depths, yet yield at very different loads. The ability to sustain load elastically does not influence the overall deformation behavior. This set of experiments does not have an obvious explanation for the tremendous variability observed.

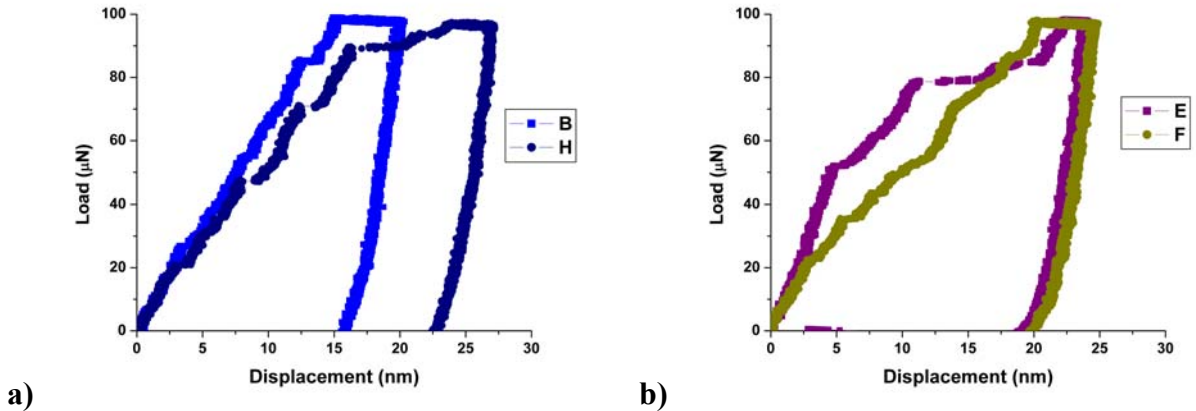


Figure 4- 5 Load-displacement data demonstrating that the yield load does not correlate to final depth a) two indents with very similar loads at yield with very different depths of penetration b) two indents with very similar depths of penetration that have very different yield points.

There are some other interesting points of comparison in the data pictured in **Figure 4-4**. The indents at the extremes of this spectrum of results show a factor of two difference in hardness and would therefore be expected to have vastly different surfaces. The before and after pictures for each indent are shown in **Figure 4-6 (a-d)**. Both indents involve step groupings and appear to have very similar surfaces. Cross sections of the images prior to indentation are pictured in **Figure 4-6 (e-f)**, with the approximate area of the indent outlined by the arrows. This reiterates the observation that the locations of these two indents are comparable. The load-displacement data for these tests is shown in **Figure 4-6 (g)**. The vastly different measurements can not be attributed to structural aspects, for the two locations appear very similar.

In contrast, some of the tests shown in **Figure 4-4** have nearly equivalent displacement results. **Figure 4-7** compares indents E, F, and G. The before and after images of the locations of these tests display surprising differences in the surface structure. Indent E is done in the middle of a step bunch. Indent F is done on a relatively flat part of a terrace. Indent G is on surface the experienced significant scratching. Subsequent testing has demonstrated that indenting the center of a step tends to decrease the measured hardness, while scratching tends to increase that same value. (The results concerning the role of surface features will be discussed in Section 4-3) These surfaces involve some significant attributes that usually lead to changes in the measured hardness,

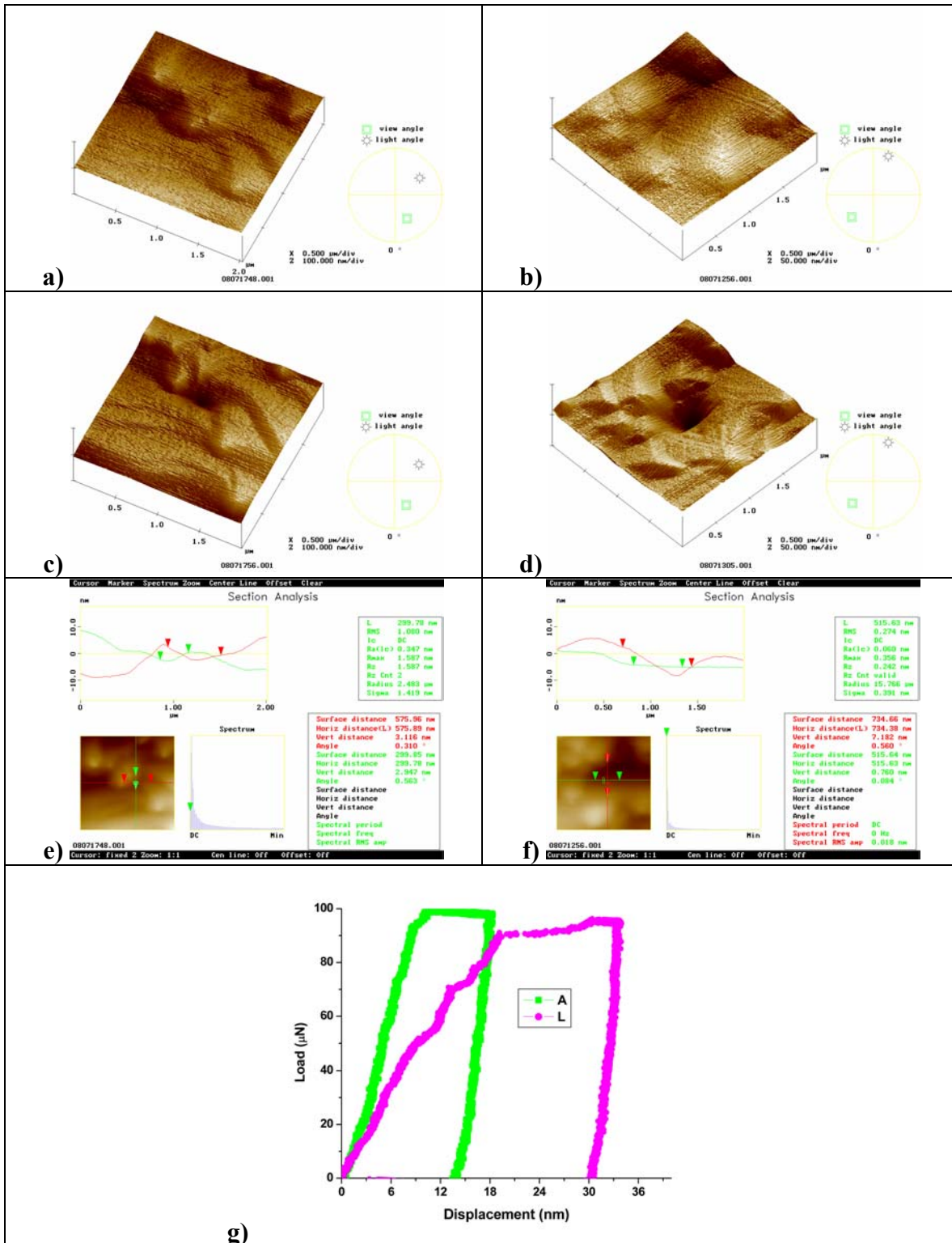


Figure 4- 6 Comparing the two extremes in measured hardness pictured in Figure 4-4. a) Image of the gold surface before indentation test A. b) Image of the gold surface before indentation test L. c) Image of the gold surface after indentation test A. d) Image of the gold surface after indentation test L. e) Cross section of before picture with area of indent A approximated by arrows. f) Cross section of before picture with area of indent L approximated by arrows. g.) Load-displacement data for two pictured indents. Despite their drastically different hardness results, the two surfaces look relatively similar.

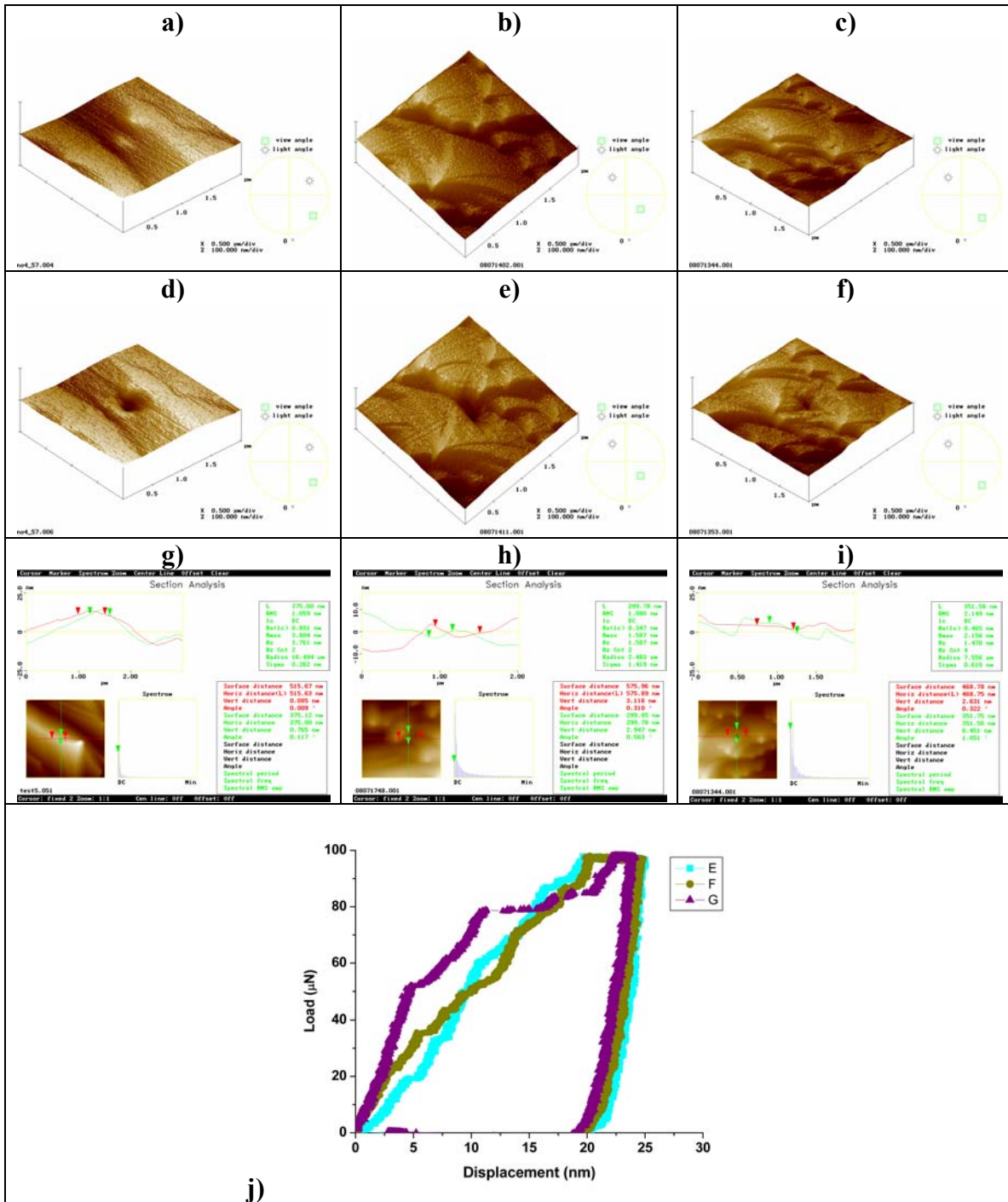


Figure 4- 7 Comparison of indentation tests E, F, and G pictured in Figure 4-4, which display very consistent results. a) Image of the gold surface before indentation test E. b) Image of the gold surface before indentation test F. c) Image of the gold surface before indentation test G. d) Image of the gold surface after indentation test E. e) Image of the gold surface after indentation test F. f) Image of the gold surface after indentation test G, with some evidence of slight surface scratching g) Cross section of before picture with area of indent E approximated by arrows. h) Cross section of before picture with area of Indent F approximated by arrows i) Cross section of before picture with area of indent G approximated by arrows. j.) Load-displacement data for indents E, F, and G. Indent E is on a step which tends to make a material appear softer. Indent G shows evidence of scratching, which work hardens the surface, making it appear harder. Despite their drastically different surfaces, they result in very similar hardness.

yet all three of these surfaces have similar results. For this entire set of experiments the standard deviation for the load at the onset of plasticity is nearly as high as the average value and the hardness varies by well over a factor of two. The inconsistencies in these values are not correlated to one another, or differences in surface structure.

Our initial experiments on gold (111) single crystals did not display the consistent results expected from what should be a model system. Indentation tests were done with both tungsten and diamond tips. Both tips had qualitatively similar results. Tests done with either tip material initially display consistent elastic loading followed by a displacement jump, indicating a burst of plastic deformation. The load at which plastic deformation occurs or the length of the initial jump in displacement varied considerably and did not correlate to the final depth of penetration. Both tip materials displayed significant variation in the depth of penetration. This is very surprising because even materials that experience staircase loading tend to exhibit relatively consistent hardness for a given surface and load. **Figure 4-8** is a histogram of hardness values measured on different days of testing. This graph shows a large distribution with no identifiable maximum or center to the population. This is not the Gaussian shaped distribution typical of most hardness tests. This histogram also spans a much larger range of measured values than is typical for this form of testing. This demonstrates that the gold (111) surface is behaving in a very unusual manner, with no obvious cause.

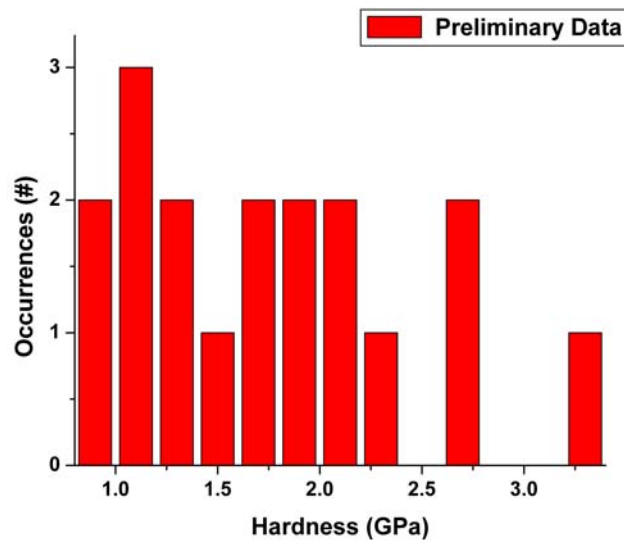


Figure 4- 8 Histogram of all the measured hardness values for a diamond indenter on gold (111) surface. This shows no identifiable center to the population. The range for the hardness values is also extremely large for this method of testing.

4.1.2 Potential Defects in Gold (111) Samples

One of the most interesting observations from the preliminary research is that whatever is controlling the deformation behavior influences almost every indent. As shown in the previous section there is no obvious cause based upon the surface images for the material to behave in such a sporadic manner. If the reason for inconsistency is not the surface, than it must be subsurface. Single crystals are often thought of as perfect structures. The data collected on Au (111) demonstrates this is not always true, for if the lattice were ideal it would always respond in the same way. The deformation behavior is considerably different than that presented by other researchers [5, 15, 64, 69, 71]. There is something causing this variation in response to point loading. The new controlling parameter must be on a specific length scale, on the order of the tip radius, in order to change the behavior of two indents in relative proximity. If the discontinuities were considerably smaller in spacing than the tip radius, there would be a large concentration within an indented volume. The influence of the high number would most likely average out and lead to a consistent response for all indents. At the other extreme, if the defects were separated by many times the tip radius, the likelihood of encountering at least one would be low, therefore only a few indents would be affected. The defects of interest are on an intermediate scale, for they influence almost all tests.

At this scale, in this system, there are a limited number of defects that are capable of causing this type of discontinuity. There are four potential crystal defects that might influence the displacement behavior: 1) Proximity to residual dislocations, 2) Surface topography, 3) Vacancy concentration and stacking fault tetrahedra, and 4) Impurity concentration. Each of these four factors has the potential to influence material deformation; some may even dominate at different times. The behaviors of these features are not fully understood at this scale. Some have never even been considered as potential factors influencing indentation behavior.

4.1.2 a Dislocations

The dislocations formed upon indentation are termed “geometrically necessary” [79]. This means that when the material is beyond its elastic limit it must make room for the indenter with dislocations. The displacement is the release of the elastic stress. The necessary stored energy to withstand the high applied force manifests itself as a dislocation that must move quickly to restore equilibrium once it is nucleated. If a dislocation is already present, propagation and stress for its motion are well below that of nucleation. Some of the indents discussed in Section 4.1.1 required resolved shear stresses on the order of theoretical shear strengths of the material in order to initiate plasticity. That indicates that there is sufficient applied stress to create dislocations. The high stresses to initiate yield do not automatically exclude the possibility of dislocations remaining in the lattice after annealing. Preexisting dislocations not only determine the applied load for deformation, but also influence subsequent dislocation behavior. The location, size, and interactions of any residual dislocations play a significant role in their ability to be operated.

The primary inconsistency in the collected data is the amount of plasticity for a given load. The formation and movement of dislocations is at the center of this problem. The most obvious factor to influence dislocation behavior is their initial presence in the lattice. The proximity of the indenter to a dislocation determines the ability of the material to deform elastically. The dislocation density of a metal single crystal is reported to be approximately 10^7 cm^{-2} , which corresponds to a mean dislocation spacing of about $3 \mu\text{m}$ [82]. Assuming the separation is well above the indentation radius and depth of penetration, the indenter could easily land in an area that is free of dislocations. A perfect lattice will initially deform elastically before a new dislocation is nucleated. There is also a probability of landing directly on a dislocation. Landing on an operable dislocation results in immediate plastic deformation. In between these extremes, a dislocation may lie somewhere within the affected zone. Differences in the distance a dislocation is from the tip can lead to variation in the onset of plasticity and resultant deformation. Where a dislocation lies within the stress field will dictate the applied load to operate it. The load falls off as the reciprocal of the distance; the further a dislocation is from the point of contact the higher the applied load must be to operate it. The variation in this distance may contribute to the spectrum of deformation behavior. It is impossible to determine by imaging where subsurface dislocations might be. Dislocation behavior quickly becomes very difficult to test because of their complex interactions and rapid movement and multiplication.

Another way to look at the dislocations is to assume that they behave as Frank-Read sources. The energy required to operate such a dislocation source is dependent upon the distance between the two pinning points. The closer together the pin points are the more difficult it is to operate the dislocation. **Figure 4-9** is a plot of the necessary shear stress as a function of pinning point separation. Note that the resolved shear stress to operate a Frank-Read source that has a separation smaller than 20 nm requires a load on the order of those observed in our experiments. Shear stresses of this order are often thought to be attributed to the formation of a dislocation by the slipping of one atomic plane over another. This means that shear stresses on the order of theoretical do not necessarily mean that the structure is perfect for other methods of dislocation formation can also require loads of this order to initiate deformation. This is important because it indicates that preexisting inoperable dislocations can be present and still require extremely high loads to operate.

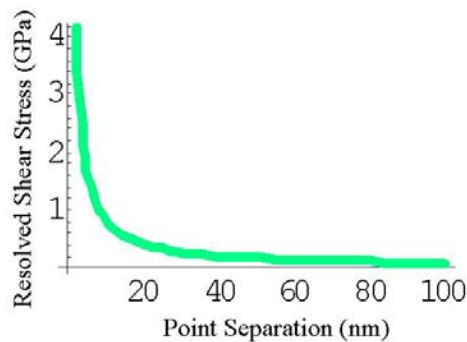


Figure 4-9 Plot of the resolved shear stress required to operate a Frank Read Source as a function of pin point separation. Resolved Shear Stresses observed in our experiments correlate to separations of 20 nm or less.

At the macroscale, hardness tests are independent of dislocation density [9]. This does not hold true at small scales, where the initial dislocation distribution is known to influence a material's ability to bear load elastically. The extensive surface preparation techniques enable surfaces with dislocation spacing on the order of microns. This is well above the indentation size; meaning tested volumes could be initially perfect structures. This gives us the potential for great insight on the creation of dislocations and their initial behavior with applied load. It is reasonable to assume that dislocation could be of the appropriate spacing to cause such sporadic behavior.

4.1.2 b Surface Structure

Another possible aspect of the crystal that is capable of causing such wide variability is the structure of the surface. The features of the surface can be as large as 100s of nanometers large at times, or in some cases quite small, less than 0.5 nm, at or below the instrumentation sensitivity, and therefore difficult to identify. There are two important aspects to the role of the surface features. The first is the change in actual contact area from that predicted based upon displacement. If the contact area is significantly different than anticipated, the applied stress is not what is expected. This will dramatically change the extent of deformation, and therefore any calculated property values. The second aspect is how the defect itself influences the criteria for dislocation movement and nucleation. There are most likely changes in the energy requirements depending upon the structural feature. A step for example will have increased influence from image forces, for there is more surface. The shape and size of the affected zone will also change. Depending upon the feature, its relative size and the indenter's proximity to it, the deformation behavior may vary widely.

During the preliminary testing we tried to isolate the influence of features. We found that the size of the feature did not seem to correlate to the displacement behavior. This is very surprising because the contact area changes are real and unavoidable, therefore they should be measurable. The fact that the surface features had no noticeable impact is a testament to how strange the initial behavior is. It is difficult to say if the indenter landed on the intended surface. It is also unclear if there were aspects of the feature, smaller or larger, that were preventing uniform contact between the indenter and the surface. The resolution of the tip, potential for inducing surface damage, and the extremely high background noise leave doubt about the implications of these tests. Further investigation is necessary to identify the contribution of inaccurate estimations in contact area and the change in requirements for deformation.

4.1.2 c Vacancies

Vacancies are lattice sites that are missing an atom. Every metal has an equilibrium number at a given temperature. Many samples are annealed before indentation testing. Annealing can create large numbers of vacancies in a material and quenching or rapid cooling can trap them at non-equilibrium concentrations. Despite the

knowledge of their presence in metals, vacancies have never been addressed as a potential factor influencing nanoindentation behavior. The main reasons for this is that most materials have sinks for vacancies such as grain boundaries. The vacancies are drawn to the lower energy state of a pre-existing discontinuity in the lattice structure. In single crystals it is reasonable to assume that there are areas of perfect lattice, as indicated by the shear stresses on the order of theoretical required to initiate deformation. In near perfect structures large numbers of vacancies can be trapped during sample preparation, for the nearest sink is the surface. Based on what we know of our samples and the heat treatment they are subjected to (to ensure a clean surface) it is very likely that vacancies are being trapped in the crystals.

In order to determine the role of vacancies, the equilibrium concentrations must be determined, both at room temperature and at the annealing temperature. The equation for equilibrium vacancy concentration is exponentially related to the temperature (T) and the enthalpy of formation per mole of vacancy (H_f) [83].

$$C_V = E^{H_f/RT} \quad (4.1)$$

C_V is the concentration of vacancies and R is the ideal gas constant (8.31 joules per mole degree K). For gold, the formation energy for a mole of vacancies (H_f) is 83,900 joules. At room temperature (300 K) the vacancy concentration is 2.46×10^{-15} , or one vacancy every 74,000 atoms linearly. When gold is just about to melt (1335 K), the vacancy concentration raises to 5.21×10^{-4} , which is approximately a vacancy one out of every 12 atoms linearly.

In order to determine the likelihood of trapping vacancies in the metal, we need to calculate the diffusion of vacancies to the nearest defect, i.e. the surface. Vacancy movement is dependent upon the self-diffusion rate of the lattice element. Diffusion rates are also exponentially dependent upon temperature. The diffusion rate (D_T) of vacancies in a lattice is approximated by:

$$D_T = D_0 \cdot E^{-Q/RT} \quad (4.2)$$

Where D_0 is the self-diffusion rate of gold, 3.1×10^{-6} m²/s, and Q is the activation energy per mole of diffusing species, 164.8 kJ/mole for gold [84]. Solving for room temperature and the premelt temperature, diffusion rates of less than 10^{-16} nm²/second and 10^6 nm²/second are predicted respectively. This is a considerable difference in mobility.

A concentration profile can predict how quickly these equilibrium configurations are attained. While there is not a good description of the crystals cooling profile, these calculations will indicate if the trapping of vacancies is likely to occur. Using Fick's second law we can write an expression for concentration as a function of time (t) and position (x), at a given an annealing temperature T . This can be written [83]:

$$C[x,t] = C_0 + (C_T - C_0) \cdot \text{Erf} \left(\frac{x}{\sqrt{4 \cdot D_T \cdot t}} \right) \quad (4.3)$$

Where C_0 is the initial vacancy concentration and C_T is the equilibrium or surface concentration at the annealing temperature. To demonstrate the difference in diffusion rates, at the pre-melt temperature it takes 30 seconds to diffuse in the equilibrium concentration of vacancies at a depth of 100 nm. If the gold were then quenched to room temperature, it would take 10^{38} years for the material to diffuse out these vacancies to reach its equilibrium room temperature vacancy concentration. While the crystal is not actually quenched, it does cool very quickly. A very large number of vacancies are most likely trapped in the crystal, on the order of a billion in an average sized indent. This number is far too large for the vacancies themselves to cause the variability, for each indented volume would have similar concentrations.

Vacancies in super saturation often coalesce and form stacking faults. In FCC metals these low-energy stacking faults often grow to form stacking fault tetrahedra [22]. Transmission Electron Microscope (TEM) of quenched gold has shown that these tetrahedra can be 10s of nanometers, with spacing on the same order. Stacking fault tetrahedra nucleate heterogeneously at lattice defects such as impurities. The large stacking fault tetrahedra grow at the expense of the smaller ones [23]. These structures can start as small as a few vacancies. The upper size limits are defined by the stacking fault energy. When the energy cost of the large stacking fault area is too great, a dislocation is nucleated.

A possible explanation for the observed gold behavior is the presence of stacking fault tetrahedra in the structure. These tetrahedra grow with the pressure applied during indentation, until they reach a critical size. When the stacking fault energy is too large, the tetrahedra break apart, nucleating the geometrically necessary dislocations. The extent of displacement is dependent upon the location of the tetrahedra, its orientation, and size, as well as the concentration of these structures within an indented volume. From approximate calculations it looks as if the spacing of these tetrahedra may be of the right order to be causing the variation in indentation.

4.1.2 d Impurities

Impurities in single crystals are known to exist but are often ignored. The number and type of impurity depends upon the fabrication method and apparatus history. Different elements would have a varied strain on the lattice depending upon their proximity to each other and their size relative to that of gold. For example a silver atom only differs from a gold atom by less than 0.2 % and would have a minimal misfit. Iron would cause more of a lattice strain for it is 13.9 % smaller than a gold atom. The presence of a potassium atom would significantly distort the structure for it is 57.6 % larger than that of gold [76]. Unfortunately the relative percentages of impurity atoms in our crystals are unknown, but the crystal is 99.99% pure gold. Some typical impurities are Ag, Cu, Fe, and Si. Although this sounds very pure, it means that 1 out of every 10,000 atoms is an impurity. This translates to a linear spacing of 1 every 22 atoms, or approximately every 10 nm. In this study the average indented volume contains approximately 3×10^9 atoms, which means there are approximately 3×10^5 impurities in that space. This is quite a large number, much bigger than anticipated for an apparently pure substance. Even if the crystals were made 99.9999% pure, there would still be $3 \times$

10^3 impurities in any given indent. At this concentration it is highly unlikely that the impurities could be responsible for any deviation in behavior. They are so abundant that they would most likely be evenly distributed throughout the lattice. At these densities it is difficult to say that the distribution would be sufficiently different in one indented volume compared to another. It is not readily apparent how to test for impurity influence, for the concentration or distribution cannot be changed. For this reason, we are not going to investigate the specific role of impurities in deformation behavior.

4.2 Test Matrix

Often when performing experiments, there are numerous parameters that influence test results. It is often difficult to identify the contribution from each factor and simultaneously optimize their level without doing a large number of experiments. Depending upon the number of factors and levels of interest, the required experimentation to fully evaluate the individual roles of each necessitates more tests than are capable of being performed. This is where design of experiments comes into use. Designed experiments allow evaluation of a variety of factors and even their interactions with a reduced number of trials. Dr. Genechi Taguchi's primary contribution to field of experimental design was the use of orthogonal arrays. The Taguchi approach specifically tries to optimize processing conditions to try and minimize variation. Using a statistical approach to analyzing the data, the role of factors and their optimum level can be readily determined with a fraction of the experiments.

4.2.1 Test Matrix Definition

The initial results from indentation tests on gold were nothing like those gathered by Corcoran or the group at Sandia National Labs [5, 15, 64, 71]. One of the only differences in the experiments performed by Corcoran et al and our experiments was the surface preparation technique. Although based upon the same guidelines, each of the steps of surface preparation is very operator dependent. The surface preparation technique was adopted from the Sieradzki group at Arizona State University, which primarily does in-situ imaging of electrochemical processes. The requirements for electrochemical observations and indentation experiments are very similar. Both groups want very clean samples with large atomically flat areas.

Since the slight changes in surface preparation seem to be the only difference in the samples tested by Corcoran and ourselves, we decided to test some of the aspects of the preparation technique that had changed with the operator. One of the differences was the length of flame annealing. The electrochemical group typically flame anneals for approximately 5 min, while our preparation often had flaming durations of at least 25 minutes. The reason we had increased the duration of flaming was that when we used shorter times the surface began to look like that pictures in **Figure 4-10**. This is a $1\mu\text{m}$ image, and clearly shows that the surface consisted entirely of steps, each only a nanometer or less in height. We thought that these uneven surfaces might be the source of some of the data inconsistencies. By flame annealing for longer periods of time the terrace between steps grew to 100's of nm, or large enough to place an indent upon.

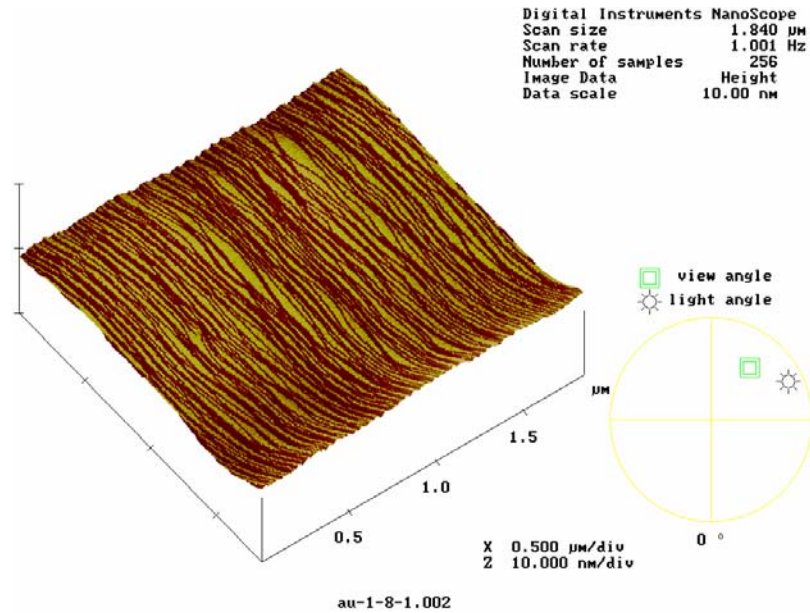


Figure 4- 10 Scanning Tunneling Micrograph of a gold (111) surface. The height of this image is 10nm, while the x and y-axes each measure 1 micron. The surface is covered with small steps, the result of insufficient flame annealing.

Another of the major differences in sample preparation techniques was the number of times the crystal was electropolished and flame annealed before it was mechanically polished to create a planar surface again. The Seradski group often does a quick mechanical polish every few cycles. **Figure 4-11** is an image of the surface using Scanning Tunneling Microscopy that shows there are large terraces on the surface, but there are also a significant number of scratches. While many of the goals for the surface quality are shared by these two groups there is a major difference. They are looking at growth and dissolution processes that occur on a surface. The presence of scratches and the dislocations that accompany them are not a primary concern. For mechanical testing these scratches are more significant. The more times electropolishing is done the more material is removed. It is apparent from **Figure 4-11** that more than one cycle of electropolishing is necessary in order to remove all of the damage incurred during a mechanical polish. This is one of the reasons we have looked at the number of times the crystal is electropolished and flame annealed prior to testing.

The slight changes in the sample preparation seemed to cause the measured mechanical behavior of the material to change dramatically. We decided to look at the two primary changes in our preparation technique to try to understand the role they played in the nanoindentation behavior. The duration of the flame anneal changes the surface topography. The length of time at elevated temperature also helps dislocations to be annealed out. Both of these factors are known to influence the nanoindentation behavior. The number of times a crystal is electropolished and flame annealed also influences the structure and dislocation density. Neither a change in the number of times a crystal is electropolished nor an increase in the duration of the flame anneal will isolate the contribution due to the surface features or the dislocation density, for they will both

be influenced by the changes. The purpose is to create different enough surfaces to help explain the measured variation in hardness.

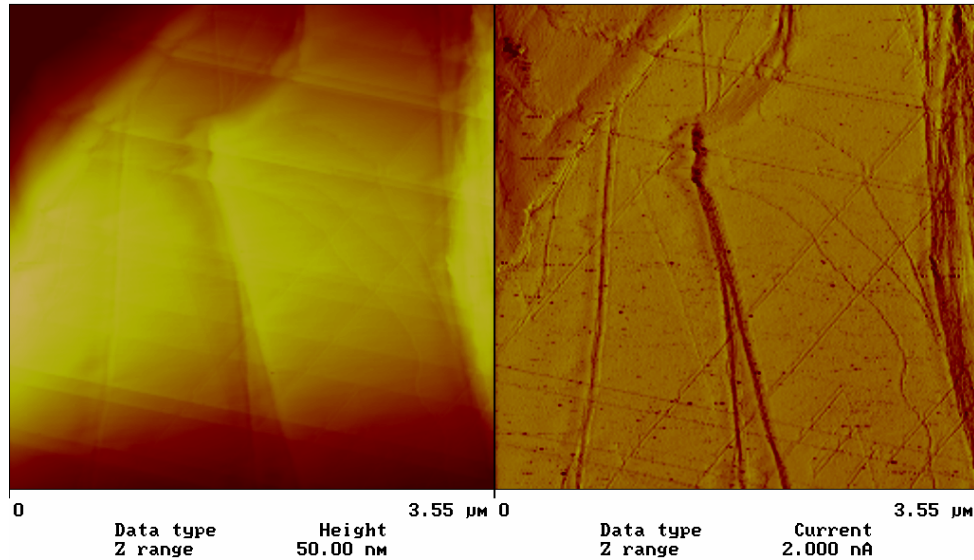


Figure 4- 11 Scanning Tunneling Micrograph of a gold (111) surface. The terraces are sufficiently large to place indents on, but show signs of scratches that remain from the mechanical polishing stage of sample preparation. The left image is a measure of the change in height across the imaged area. The image on the right is the change in current in the same region. Current images often highlight edges that are difficult to resolve in the height mode.

In the previous section we hypothesized that a defect might be responsible for the large variation in measured hardness. One potential defect is vacancies and the stacking fault structures they form when gold is quenched. The other two factors we decided to adjust did not influence the vacancies. To isolate their contribution different cooling rates were used to vary their concentration. Using Mathematica we created a program that utilizes finite difference to predict the concentration profile for vacancies in gold crystals subjected to different cooling rates. Initially we found that the vacancies are very difficult to remove without the presence of a large sink such as a grain boundary. The procedure used in all of our preliminary results had the crystal cooled on a refractory brick that acted as a large heat sink, cooling the crystal in a matter of minutes. This was our intermediate concentration. We utilized the finite difference program to optimize a cooling profile to reduce the vacancy concentration by a significant amount in a reasonable amount of time. We created a stepped furnace anneal to reduce our vacancies to the minimum level. The third level is created by quenching the crystal at the end of the flame annealing period.

Upon further investigation we realized that the diffusivity we were employing was incorrect. We were utilizing the self diffusion rate, which takes into account the probability that one of the nearest neighbors to an atom is a vacancy. Unlike an atom of metal that requires a neighboring vacancy to move, a vacancy can “jump” to any surrounding lattice site. In order to correct for the increased mobility, the self diffusion rate of the element is divided by the vacancy concentration [85]:

$$D_V = \frac{D_T}{C_V} = \frac{D_0 \cdot E^{-Q/RT}}{E^{H_f/RT}} \quad (4.4)$$

Solving for room temperature and the premelt temperature, diffusion rates of 10^{-2} $\text{nm}^2/\text{second}$ and 10^9 $\text{nm}^2/\text{second}$ are predicted respectively. At these diffusion speeds we would not even predict the formation of the stacking faults that have been proven to exist by TEM experiments [86]. Diffusivity alone is insufficient to predict the existence of stacking fault tetrahedral. The different cooling profiles still accomplish their initial intent, for the furnace annealed should render vacancy free samples and the quenched sample should contain stacking fault structures.

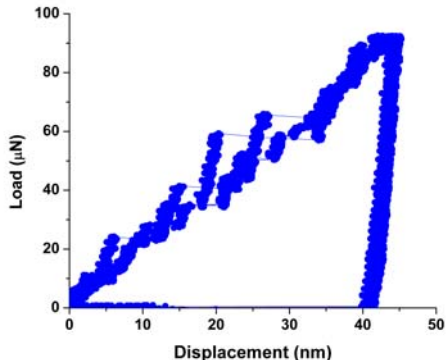
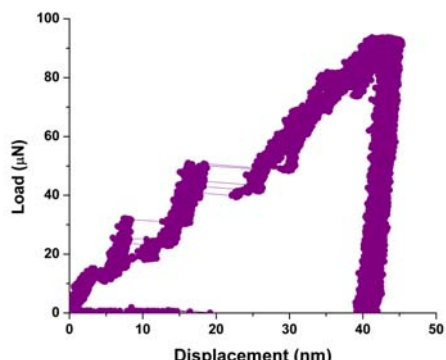
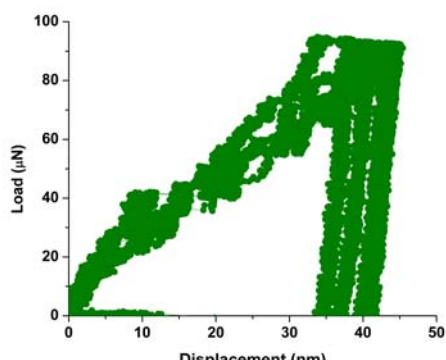
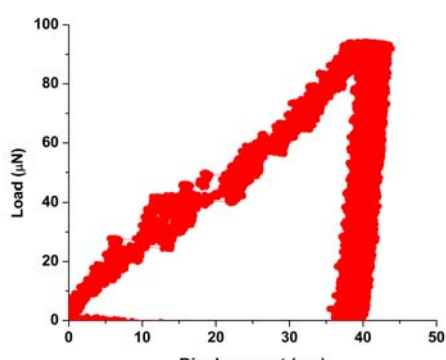
We wanted to perform a systematic study that investigated the influences of these changes in surface preparation on the mechanical behavior of the material. The resultant test matrix, an L-9 array of three different factors investigated at three different levels is shown in **Table 4-3**. Each test began with a surface that had been mechanically polished using alumina paste with a final grit size of $0.5 \mu\text{m}$. In order to ensure the same starting point for each test, mechanical polishing was performed prior to the preparation conditions indicated in the experimental matrix. The minimum duration for flame annealing was five minutes because that is the original guideline from the Sieradzki group. Twenty-five minutes was chosen because that is the minimum duration utilized by our group. Fifteen minutes was chosen as an intermediate value. The number of cycles of electropolishing and flame annealing was varied to see if the additional removal of material influenced the mechanical properties. Testing after one cycle was done to provide a worst case surface, a large number of residual defects from mechanical polishing. It was hypothesized that four cycles would be enough to remove all of the damaged area and this is approximately the frequency with which the crystal is polished by the other researchers. Eight cycles of electropolish and flame annealing would remove considerable material and have considerable time at temperature, and therefore should behave as an idealized crystal with no residual deformation from the mechanical polish. In order to identify the role of vacancies, the rate at which the crystal was cooled was varied. The crystal was cooled quickly with compressed Nitrogen gas in order to try and trap as many vacancies in the crystal as possible. Letting the crystal cool in the air after flaming was completed, a process that takes approximately 15 min yields an intermediate concentration. A three day stepped cooling profile was developed to dramatically reduce the number of vacancies. The three factors at the three levels were placed in a Taguchi test matrix. **Table 4-3** is the orthogonal array, which enables the statistical analysis of the results. In this context, orthogonal means balanced. In every column, each level appears the same number of times. This enables each factor to have the same opportunity to influence the data regardless of the column they are in. The array is balanced in a second way. Any two columns have equal numbers of each level combination. The balance enables the statistical analysis to separate the contribution of each factor and level.

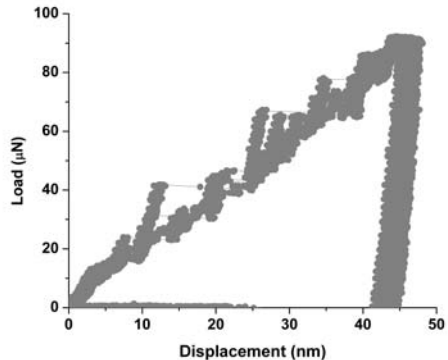
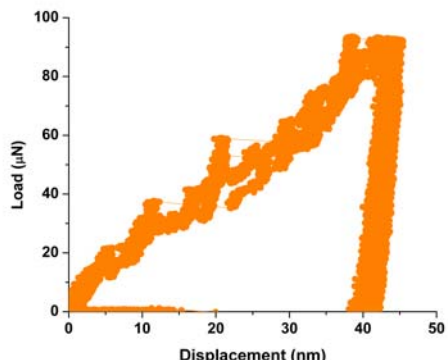
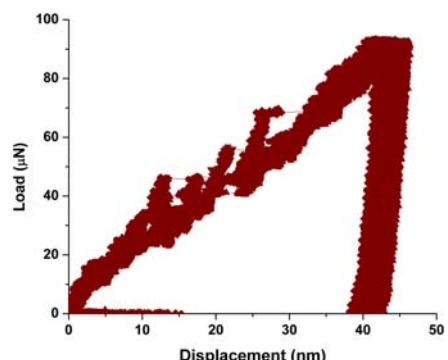
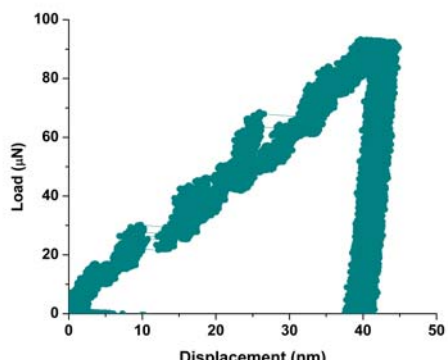
Test Number	Duration of Flaming (min)	Number of Cycles	Cooling Profile
1	5	1	Quench
2	5	4	Room Cool
3	5	8	Anneal
4	15	1	Room Cool
5	15	4	Anneal
6	15	8	Quench
7	25	1	Anneal
8	25	4	Quench
9	25	8	Room Cool

Table 4-3 Taguchi L-9 Array for three parameters at three levels. The first parameter is the duration of flame annealing which was varied from 5 min to 25 minutes. The second factor was the number of times the crystal was electropolished and flame annealed before it was tested. This was varied from a single electropolish and flame anneal to eight such surface treatments prior to testing. The third parameter is the cooling rate which was varied from a rapid quench to a 63 hour stepped anneal.

4.2.2 Experimental Results

For each of the matrix test conditions we identified the five best indents. These were selected based upon the criteria that the surface had not been scratched prior to testing (as best could be determined) and the indent was placed on a relatively flat spot (meaning minimal step bunches involved in the deformed area). This was done in order to compare like surfaces. The role of stepped and scratched surfaces adds considerable complexity. By selecting an equal number of like indents the testing conditions are compared more fairly. The results for each set of preparation conditions are shown in **Figure 4-12**, along with the average values and standard deviation for some of the important aspects of the data. In comparing the initial gold indentation testing to that of fused silica it became very apparent that the ability to bear load elastically and the extent of deformation are the two aspects that most clearly demonstrate the inconsistency in measured behavior. Two points have been taken from each load-displacement curve, the yield load (the point at which plasticity is indicated by a displacement jump or change in loading slope) and the maximum depth taken at the end of the hold at maximum load. These two values are then used to calculate the maximum shear stress required to initiate deformation and the hardness of the material.

<p>Test 1</p>	 <p>A scatter plot showing Load (μN) on the y-axis (0 to 100) and Displacement (nm) on the x-axis (0 to 50). The data points are blue. The curve starts at (0,0), rises to a yield point at approximately 10.7 μN, then continues to a maximum load of about 90 μN at 44.5 nm displacement, before dropping sharply to zero at approximately 42 nm.</p>	<table border="1"> <thead> <tr> <th></th> <th>Average</th> <th>Standard Deviation</th> </tr> </thead> <tbody> <tr> <td>Yield Load (μN)</td> <td>10.7</td> <td>2.1</td> </tr> <tr> <td>τ_{max} (GPa)</td> <td>1.66</td> <td>0.11</td> </tr> <tr> <td>Maximum Depth (nm)</td> <td>44.5</td> <td>0.8</td> </tr> <tr> <td>Hardness (GPa)</td> <td>0.796</td> <td>0.029</td> </tr> </tbody> </table>		Average	Standard Deviation	Yield Load (μN)	10.7	2.1	τ_{max} (GPa)	1.66	0.11	Maximum Depth (nm)	44.5	0.8	Hardness (GPa)	0.796	0.029
	Average	Standard Deviation															
Yield Load (μN)	10.7	2.1															
τ_{max} (GPa)	1.66	0.11															
Maximum Depth (nm)	44.5	0.8															
Hardness (GPa)	0.796	0.029															
<p>Test 2</p>	 <p>A scatter plot showing Load (μN) on the y-axis (0 to 100) and Displacement (nm) on the x-axis (0 to 50). The data points are purple. The curve starts at (0,0), rises to a yield point at approximately 13.0 μN, then continues to a maximum load of about 95 μN at 44.7 nm displacement, before dropping sharply to zero at approximately 42 nm.</p>	<table border="1"> <thead> <tr> <th></th> <th>Average</th> <th>Standard Deviation</th> </tr> </thead> <tbody> <tr> <td>Yield Load (μN)</td> <td>13.0</td> <td>1.8</td> </tr> <tr> <td>τ_{max} (GPa)</td> <td>1.78</td> <td>0.83</td> </tr> <tr> <td>Maximum Depth (nm)</td> <td>44.7</td> <td>0.5</td> </tr> <tr> <td>Hardness (GPa)</td> <td>0.805</td> <td>0.015</td> </tr> </tbody> </table>		Average	Standard Deviation	Yield Load (μN)	13.0	1.8	τ_{max} (GPa)	1.78	0.83	Maximum Depth (nm)	44.7	0.5	Hardness (GPa)	0.805	0.015
	Average	Standard Deviation															
Yield Load (μN)	13.0	1.8															
τ_{max} (GPa)	1.78	0.83															
Maximum Depth (nm)	44.7	0.5															
Hardness (GPa)	0.805	0.015															
<p>Test 3</p>	 <p>A scatter plot showing Load (μN) on the y-axis (0 to 100) and Displacement (nm) on the x-axis (0 to 50). The data points are green. The curve starts at (0,0), rises to a yield point at approximately 20.5 μN, then continues to a maximum load of about 95 μN at 43.1 nm displacement, before dropping sharply to zero at approximately 42 nm.</p>	<table border="1"> <thead> <tr> <th></th> <th>Average</th> <th>Standard Deviation</th> </tr> </thead> <tbody> <tr> <td>Yield Load (μN)</td> <td>20.5</td> <td>7.3</td> </tr> <tr> <td>τ_{max} (GPa)</td> <td>2.05</td> <td>0.25</td> </tr> <tr> <td>Maximum Depth (nm)</td> <td>43.1</td> <td>2.7</td> </tr> <tr> <td>Hardness (GPa)</td> <td>0.862</td> <td>0.090</td> </tr> </tbody> </table>		Average	Standard Deviation	Yield Load (μN)	20.5	7.3	τ_{max} (GPa)	2.05	0.25	Maximum Depth (nm)	43.1	2.7	Hardness (GPa)	0.862	0.090
	Average	Standard Deviation															
Yield Load (μN)	20.5	7.3															
τ_{max} (GPa)	2.05	0.25															
Maximum Depth (nm)	43.1	2.7															
Hardness (GPa)	0.862	0.090															
<p>Test 4</p>	 <p>A scatter plot showing Load (μN) on the y-axis (0 to 100) and Displacement (nm) on the x-axis (0 to 50). The data points are red. The curve starts at (0,0), rises to a yield point at approximately 12.3 μN, then continues to a maximum load of about 95 μN at 42.4 nm displacement, before dropping sharply to zero at approximately 42 nm.</p>	<table border="1"> <thead> <tr> <th></th> <th>Average</th> <th>Standard Deviation</th> </tr> </thead> <tbody> <tr> <td>Yield Load (μN)</td> <td>12.3</td> <td>3.7</td> </tr> <tr> <td>τ_{max} (GPa)</td> <td>1.73</td> <td>0.16</td> </tr> <tr> <td>Maximum Depth (nm)</td> <td>42.4</td> <td>1.1</td> </tr> <tr> <td>Hardness (GPa)</td> <td>0.876</td> <td>0.039</td> </tr> </tbody> </table>		Average	Standard Deviation	Yield Load (μN)	12.3	3.7	τ_{max} (GPa)	1.73	0.16	Maximum Depth (nm)	42.4	1.1	Hardness (GPa)	0.876	0.039
	Average	Standard Deviation															
Yield Load (μN)	12.3	3.7															
τ_{max} (GPa)	1.73	0.16															
Maximum Depth (nm)	42.4	1.1															
Hardness (GPa)	0.876	0.039															

<p>Test 5</p>	 <p>A scatter plot showing Load (μN) on the y-axis (0 to 100) and Displacement (nm) on the x-axis (0 to 50). The data points are grey, forming a hysteresis loop that rises to a peak load of approximately 90 μN at 45 nm displacement before returning to zero.</p>	<table border="1"> <thead> <tr> <th></th> <th>Average</th> <th>Standard Deviation</th> </tr> </thead> <tbody> <tr> <td>Yield Load (μN)</td> <td>12.8</td> <td>1.3</td> </tr> <tr> <td>τ_{\max} (GPa)</td> <td>1.77</td> <td>0.61</td> </tr> <tr> <td>Maximum Depth (nm)</td> <td>47.0</td> <td>0.8</td> </tr> <tr> <td>Hardness (GPa)</td> <td>0.720</td> <td>0.026</td> </tr> </tbody> </table>		Average	Standard Deviation	Yield Load (μN)	12.8	1.3	τ_{\max} (GPa)	1.77	0.61	Maximum Depth (nm)	47.0	0.8	Hardness (GPa)	0.720	0.026
	Average	Standard Deviation															
Yield Load (μN)	12.8	1.3															
τ_{\max} (GPa)	1.77	0.61															
Maximum Depth (nm)	47.0	0.8															
Hardness (GPa)	0.720	0.026															
<p>Test 6</p>	 <p>A scatter plot showing Load (μN) on the y-axis (0 to 100) and Displacement (nm) on the x-axis (0 to 50). The data points are orange, forming a hysteresis loop that rises to a peak load of approximately 95 μN at 45 nm displacement before returning to zero.</p>	<table border="1"> <thead> <tr> <th></th> <th>Average</th> <th>Standard Deviation</th> </tr> </thead> <tbody> <tr> <td>Yield Load (μN)</td> <td>14.9</td> <td>3.1</td> </tr> <tr> <td>τ_{\max} (GPa)</td> <td>1.86</td> <td>0.12</td> </tr> <tr> <td>Maximum Depth (nm)</td> <td>44.8</td> <td>0.6</td> </tr> <tr> <td>Hardness (GPa)</td> <td>0.796</td> <td>0.023</td> </tr> </tbody> </table>		Average	Standard Deviation	Yield Load (μN)	14.9	3.1	τ_{\max} (GPa)	1.86	0.12	Maximum Depth (nm)	44.8	0.6	Hardness (GPa)	0.796	0.023
	Average	Standard Deviation															
Yield Load (μN)	14.9	3.1															
τ_{\max} (GPa)	1.86	0.12															
Maximum Depth (nm)	44.8	0.6															
Hardness (GPa)	0.796	0.023															
<p>Test 7</p>	 <p>A scatter plot showing Load (μN) on the y-axis (0 to 100) and Displacement (nm) on the x-axis (0 to 50). The data points are dark red, forming a hysteresis loop that rises to a peak load of approximately 95 μN at 45 nm displacement before returning to zero.</p>	<table border="1"> <thead> <tr> <th></th> <th>Average</th> <th>Standard Deviation</th> </tr> </thead> <tbody> <tr> <td>Yield Load (μN)</td> <td>15.5</td> <td>4.6</td> </tr> <tr> <td>τ_{\max} (GPa)</td> <td>1.87</td> <td>0.18</td> </tr> <tr> <td>Maximum Depth (nm)</td> <td>45.0</td> <td>1.2</td> </tr> <tr> <td>Hardness (GPa)</td> <td>0.789</td> <td>0.029</td> </tr> </tbody> </table>		Average	Standard Deviation	Yield Load (μN)	15.5	4.6	τ_{\max} (GPa)	1.87	0.18	Maximum Depth (nm)	45.0	1.2	Hardness (GPa)	0.789	0.029
	Average	Standard Deviation															
Yield Load (μN)	15.5	4.6															
τ_{\max} (GPa)	1.87	0.18															
Maximum Depth (nm)	45.0	1.2															
Hardness (GPa)	0.789	0.029															
<p>Test 8</p>	 <p>A scatter plot showing Load (μN) on the y-axis (0 to 100) and Displacement (nm) on the x-axis (0 to 50). The data points are teal, forming a hysteresis loop that rises to a peak load of approximately 95 μN at 45 nm displacement before returning to zero.</p>	<table border="1"> <thead> <tr> <th></th> <th>Average</th> <th>Standard Deviation</th> </tr> </thead> <tbody> <tr> <td>Yield Load (μN)</td> <td>14.3</td> <td>2.2</td> </tr> <tr> <td>τ_{\max} (GPa)</td> <td>1.83</td> <td>0.94</td> </tr> <tr> <td>Maximum Depth (nm)</td> <td>43.7</td> <td>0.7</td> </tr> <tr> <td>Hardness (GPa)</td> <td>0.833</td> <td>0.026</td> </tr> </tbody> </table>		Average	Standard Deviation	Yield Load (μN)	14.3	2.2	τ_{\max} (GPa)	1.83	0.94	Maximum Depth (nm)	43.7	0.7	Hardness (GPa)	0.833	0.026
	Average	Standard Deviation															
Yield Load (μN)	14.3	2.2															
τ_{\max} (GPa)	1.83	0.94															
Maximum Depth (nm)	43.7	0.7															
Hardness (GPa)	0.833	0.026															

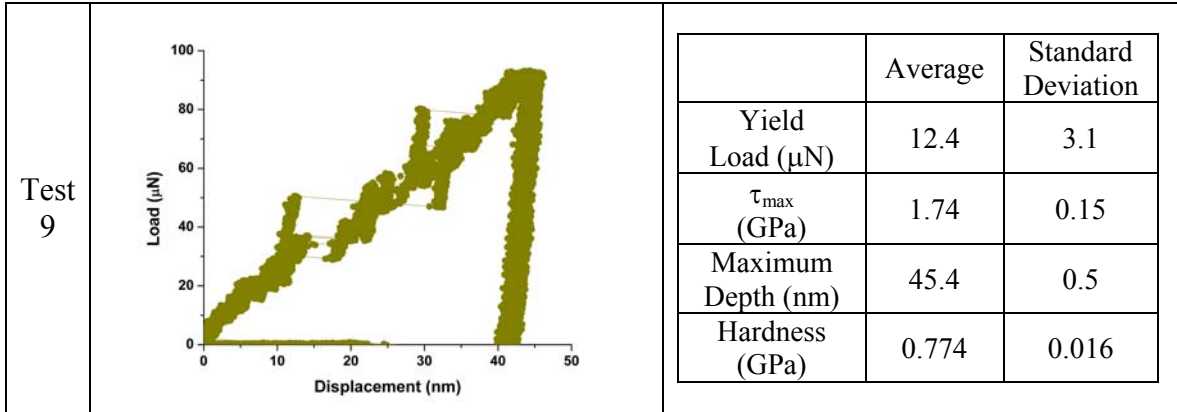


Figure 4- 12 Load-displacement data for each of the experiments defined by the test matrix. Five indents were selected for each testing condition based upon the images of the location to try and compare like surfaces. Selected indents were placed surfaces that were not scratched and involved the smallest steps possible. Average property values for the selected tests are also given. The selected properties are yield at load, maximum shear stress at the initiation of plasticity, maximum penetration depth and calculated hardness.

Figure 4-13 is a histogram showing the maximum and minimum hardness values for the indents selected for analysis for each of the test matrix experiments. The yellow line indicates the average value for each condition.

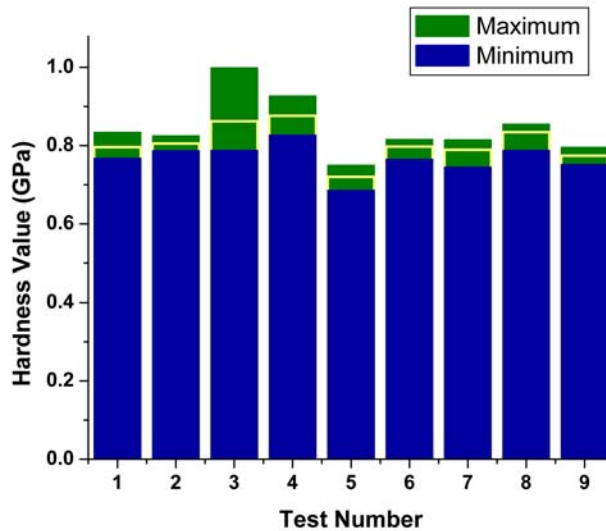


Figure 4- 13 Histogram showing the range of hardness values for each test in the matrix. These indents were selected as the 5 best under each set of conditions. This means the surfaces were not scratched and involved the smallest steps possible.

Some of the tests when isolated and compared to one another have significant differences. For example Tests 4 and 5 have a difference of over 0.156 in their average hardness value. This is a 17.8% reduction from the hardest surface of Test 4 to the softest in Test 5. Both of these test surfaces have experienced flame annealing durations

of 15 minutes for each cycle. Test 4 is only electropolished once while Test 5 experiences four cycles of electropolishing and flame annealing. Test 4 is room cooled, while Test 5 is annealed for 3 days prior to testing. The flame annealing serves two purposes. It allows the surface atoms to move to more energetically favorable lattice sites, and also cleans the surface, eliminating any organic layer that may have absorbed on the surface. Other investigations have shown that prolonged air exposure can influence the measured mechanical properties [5]. Additional tests were done on the surface of Test 5. It was flame annealed and indented again. Even with the cleaning the average hardness did not change significantly (0.75 GPa), indicating that it was not the vacancy concentration or surface contamination that caused the difference in hardness. **Figure 4-14 (a) and (b)** are representative surface images for these tests. Both surfaces have wide flat terraces to be indented upon. Surface 5 has slightly larger step bunches. Just from looking at the surface it is difficult to say why the measured hardnesses are so different. The surface for Test 4 has only experienced one electropolish, and therefore most likely has residual deformation from the mechanical polish stage. This surface is likely to be slightly work-hardened and therefore measure less deformation during testing. The reason for the more extensive deformation of the surface created by the Test 5 preparation conditions is not readily apparent based upon the data we have.

Since the original cause for the surface preparation study was the observed variation in hardness, the test with the largest standard deviation may give some insights into what causes variability. Test 3 had the widest spread in the data collected, while Test 2 was the most consistent. Representative images for these two surfaces are shown in **Figure 4-15**. Test 3 has an extremely flat surface, the z-axis is only 20nm. Test 2 does not have as flat a surface. The consistency in Test 2 is most likely due to the fact that even though flat areas were chosen for indents the terraces are not sufficiently wide, and each indent still involves step bunches. For Test 3 the standard deviation in hardness for the selected indents was 0.090 GPa for an average hardness of 0.862 GPa. This is more than twice the next closest standard deviation of 0.039 GPa for Test 4. Test 3 also happens to have initial yield loads that are nearly 1.5 times those of the other testing conditions. The average τ_{\max} for Test 3 is 2.05 GPa, which is the only test close to the preliminary result average of 2.13 GPa. This indicates that although the yield point does not correlate to the depth of penetration, that the general ability of a material to bear load elastically may be correlated to its reproducibility. The ability to bear load elastically may be correlated to the very high surface quality, indicated by wide terraces and small steps.

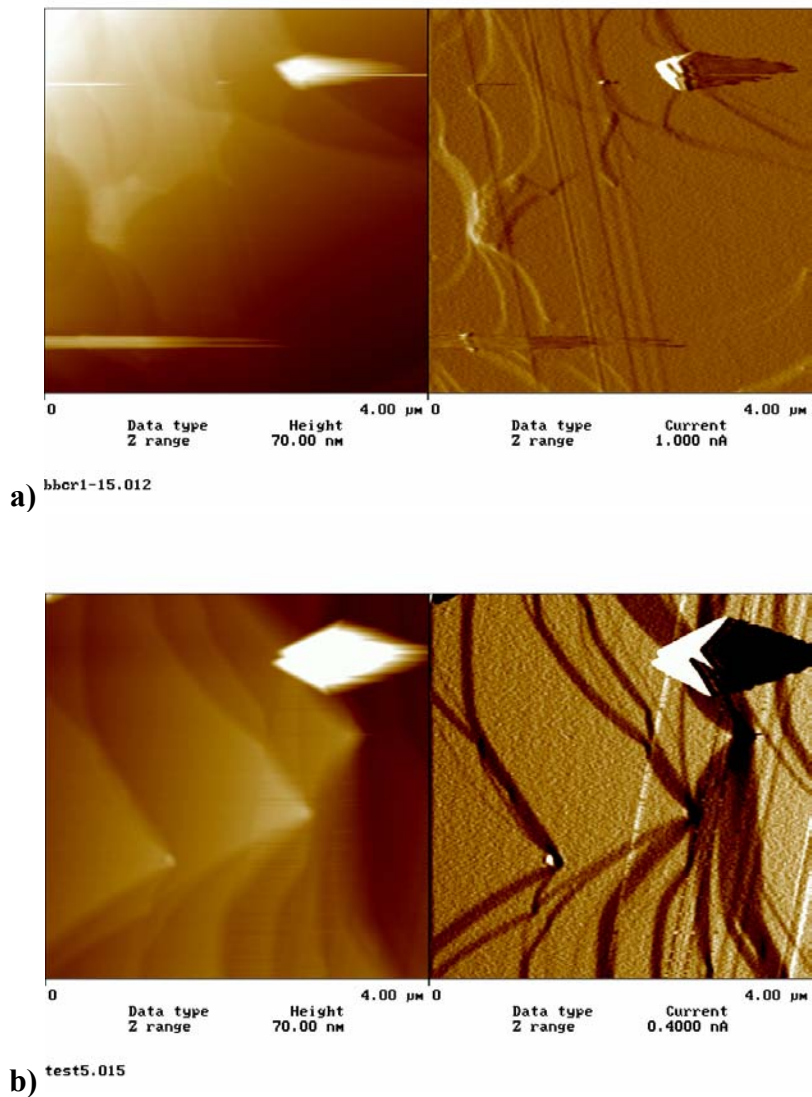


Figure 4- 14 a) Representative surface images from Test 4 Surface b) Representative surface images from Test 5 surface. Test 4 Surface was the hardest of the 9, while Test 5 was the softest. The images on the left are height images with a z axis of 70 nm in each. The images on the right are both current images.

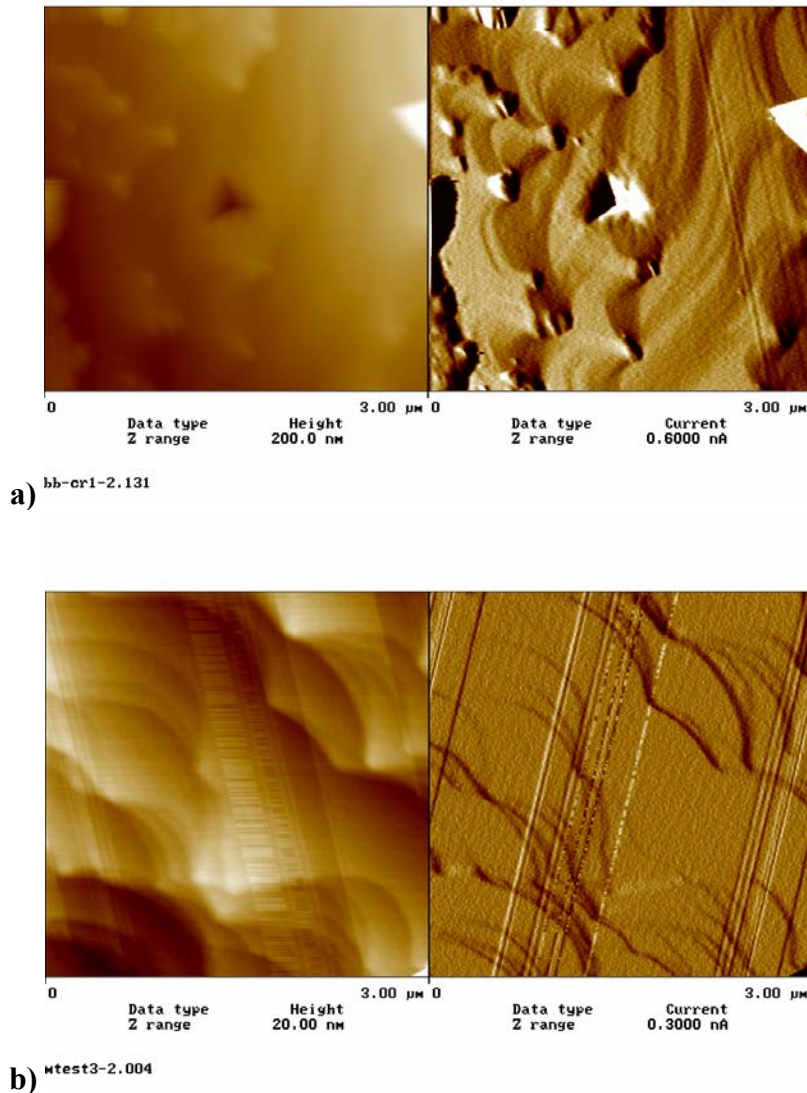


Figure 4- 15 a) Representative surface images from Test 2 Surface b) Representative surface images from Test 3 surface. Test 2 Surface had the smallest standard deviation in measured hardness, while Test 3 had the largest. The images on the left are height images with a z axis of 200 nm for Test 2 surface and 20 nm for the Test 3 surface. The images on the right are both current images.

In order to better analyze trends in the behavior and influence of changes in the preparation technique we employ the Taguchi analysis that is made possible by the orthogonal testing array. Taguchi uses a term *consistency of performance* as a means of defining quality. Consistency is when performances are nearer the target more often. The ability to make the same product every time is desirable. In our case we want to measure the same hardness value every time on the same surface. By having a particular hardness value it enables you to determine the influence of subsequent modifications to that surface. Consistency can be quantified by using the Mean Square Dividend (MSD).

The MSD is defined as the number representing the average deviation of the results from the target, and is a function of the average and standard deviation.

$$MSD = \left(\frac{(Y_1 - Y_0)^2 + (Y_2 - Y_0)^2 + \dots + (Y_n - Y_0)^2}{n} \right) = \sigma^2 + (Y_{avg} - Y_0)^2 \quad (4.5)$$

The data points are $Y_1, Y_2,$ through Y_n , the target value is Y_0 , and n is the number of data points. The MSD can also be written in terms of the standard deviation σ and the average Y_{avg} . The term σ^2 is also called the variance. This equation is very valuable because it gives equal weight to changes in the average and the standard deviation. The consistency is increased by the average value getting closer to the target and by the reduction in the distribution about that average.

The signal to noise ratio (S/N) is the term used for a modified MSD. Signal to noise ratios can be calculated in a number of different ways. The one we utilize is the logarithmic transformation of the Mean Square Dividend (MSD). This enables a wide spectrum of data to be plotted together as well as helps to highlight linear relations in the level of factors.

$$\frac{S}{N} = -10 \cdot \log_{10} MSD = -10 \cdot \log_{10} \left(\frac{(Y_1 - Y_0)^2 + (Y_2 - Y_0)^2 + \dots + (Y_n - Y_0)^2}{n} \right) \quad (4.6)$$

Multiplying the MSD number by -10, changes the desirability from smaller is better for MSD to bigger is better for S/N. These equations can be modified depending upon the desirable direction of property value shift. Specifically, if the measured value wants to be maximized (bigger is better), the reciprocal of the measured value squared is used instead of the difference from the target. For a goal of a reduced measured value (smaller is better) the measured value squared is used (a target of zero). In our case there is no specific target, but rather the variance itself was quantified. We utilize a nominal is best approach.

The S/N is averaged for each test done at each factor level, and plotted to help identify trends. **Figure 4-16** is the results of the three factors we studied and what their role was in the variation of the system. **Figure 4-16 (a)** is a plot of the influence of flame annealing duration on the hardness consistency. As might be expected it appears that increasing the duration of the flame anneal also increases the repeatability. **Figure 4-16 (b)** is the plot of the change in consistency for surfaces that were electropolished and flame annealed different number of times before testing. Increasing the number of times initially increases the consistency. As discussed above, this makes sense for it is unlikely that all the damage caused by mechanical polishing is removed with a single electropolish. What is surprising is that continued electropolishing makes the surface less consistent. Theoretically more electropolishing and flame annealing would lead to more perfect structures. The increase in variability indicates that as structure quality improves the way in which that structure responds to loading becomes more variable. We can speculate that conducting further electrochemical and flaming cycles would further

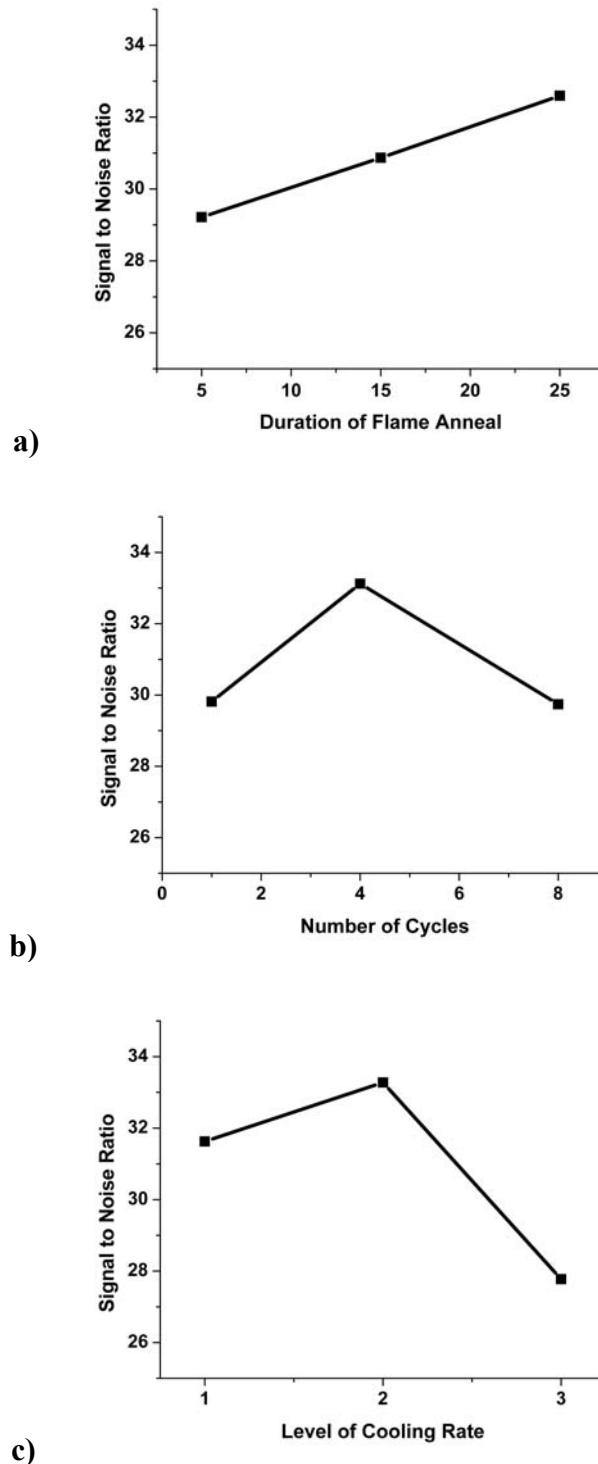


Figure 4- 16 Plots of the S/N as a function of factor level. a) Flame annealing the surface decreases variability with an increase in duration. b) The number of cycles of electropolishing and flame annealing prior to indentation testing does not have a linear relationship. Variability is increased by too little or too much electropolishing. c) Cooling rate of the crystal indicates that the largest variability occurred in the slowly cooled crystal. This may be explained by the fact that these are the only crystals that do not experience cleaning just prior to testing.

increase the variability in measured hardness. The final factor investigated was cooling rate, the results of which are pictured in **Figure 4-16 (c)**. The primary purpose of varying the speed at which the crystal cooled was to look at the role that vacancies play in the deformation. It is not clear that we would see the influence of changing the vacancy concentration based on the fact that the deformation mechanism has obviously changed in these tests. It is not entirely clear that we have even created the intended tetrahedral. The most significant difference for this factor is at the low concentration. The annealed crystal is in a furnace for three days prior to testing. The furnace was purged with argon to prevent any reactions from occurring on the surface, but none the less these are the only tests not freshly cleaned prior to testing. The extended annealing time also reduces the dislocation density. Crystals that have more time at elevated temperature should have more ideal structure. The increased variation in the annealed samples again indicates that variability is correlated to high structure quality.

Taguchi arrays also enable the study of interactions. In experiments with factors having two levels the interpretation is relatively straight forward. One factor is the x-axis. The second factor is plotted as a line for each of its levels; the endpoints are the S/N ratio for the experiments that have the two factors at the appropriate levels. If the lines are parallel there is no interaction. If the lines have very different slopes, there is most likely an interaction, the severity of which is indicated by the size of the angle made by the bisecting lines. In experiments with three level factors, the plots used to interpret interactions make it very difficult to isolate the importance of these interactions. The complexity is related to the structure of the orthogonal array and the inability to isolate the contribution of level changes from the interactions of other factors. **Figure 4-17 (a)-(c)** are the interaction plots for our test matrix. These graphs will not define the presence of interactions, but rather indicate what might be of interest to investigate with future studies. The interaction that seems to have the most influence is the combination of flame duration and cooling profile. The number of cycles and the cooling profile also appear to have some interaction. The combination of the duration of flame annealing and the number of cycles seems to have a relatively small influence. None of these interactions look significant enough to warrant extensive further testing.

Figure 4-18 is a histogram of the data recorded on the nine surfaces. Some of the surfaces appear slightly softer, and some have broader distributions than others. Overall the tests have very consistent hardness measurements despite the changes in surface preparation, even resulting in a normal distribution for the whole matrix. This histogram shows all the indents taken, including those intentionally placed on steps and those that were placed in regions that had been damaged by the probe tip prior to testing. The surface structure, both that which is created during sample preparation and that which is modified during testing, plays a role in the measured hardness. We will discuss the specific role of steps and the induced roughness caused by the probe tip scratching the surface in the next section.

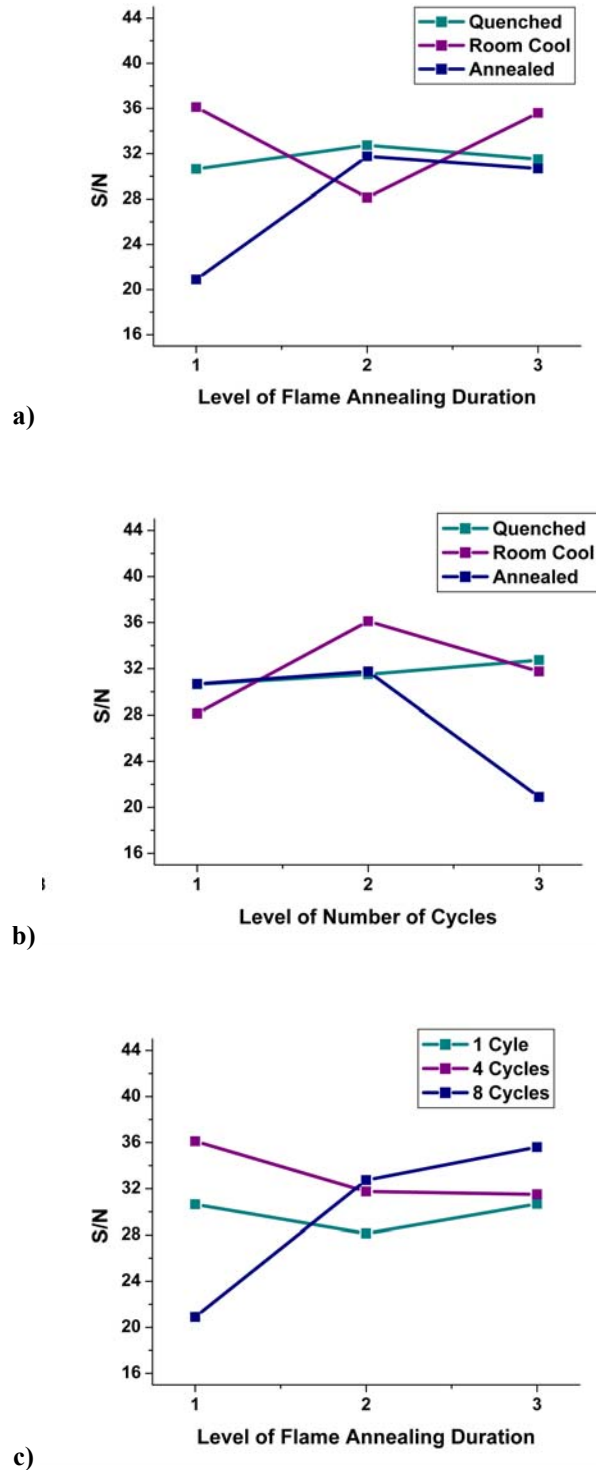


Figure 4- 17 Plots of Factor interactions a) The interaction of flame annealing and the cooling rate. b) The interaction of the number of cycles and the cooling rate. c) The interaction of the flame annealing duration and the number of cycles. Interaction plots of three level factors are very difficult to interpret, but can indicate directions for future studies. None of these interactions are significant enough to merit further investigation.

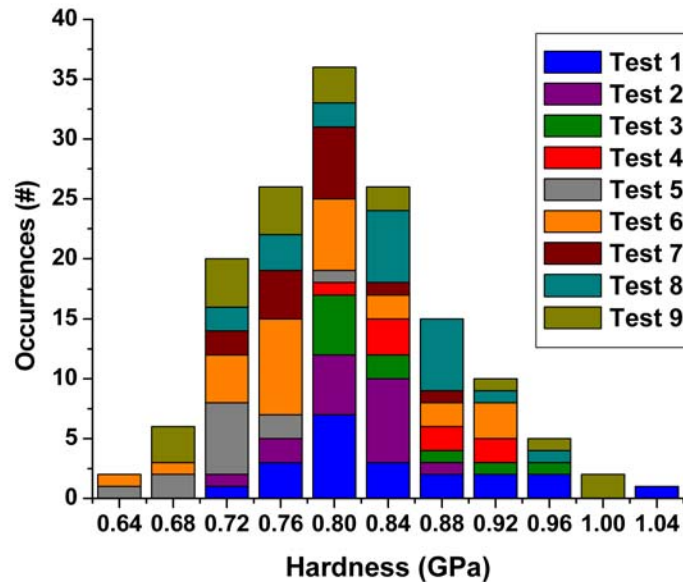


Figure 4- 18 Histogram of hardness values for all indents done on nine surfaces in test matrix. There are some slight shifts in average hardness with in a test. Some testing conditions demonstrate broader population distributions, but over all the test matrix surfaces behave in a very consistent manner. When combined the test matrix results demonstrate a normal population distribution.

The results from the test matrix were quite surprising, for the variation so prominent in the initial tests was no longer apparent. In comparison to the preliminary results, all of these tests had essentially the same measured hardness. The hardness for all of these indents is between 0.720 and 0.876 GPa. This is considerably lower than the average value of 2.05 GPa for the tests done with the same tip on the same crystal, discussed in the previous section. The average load at initial yield has changed from 27.8 nm for the variable surface to 14.0 nm for the test matrix experiments. The same gold crystal no longer displayed the very high initial yield loads seen in the preliminary results. The material yielded at lower loads and appeared considerably and consistently softer. There were some slight differences in the measured hardness and the distribution of the measurements within the test matrix. For the most part the data was extremely repeatable for all nine surface preparation conditions.

This is a significant contrast to the data discussed previously in Section 4-1. **Figure 4-19** is a histogram of the hardness values measured during the preliminary testing plotted with all the hardness results from the test matrix. For convenience the test matrix data has been plotted as a single population. It is readily apparent that there is a significant difference in the shape of the distributions and the range over which they fall. The test matrix has the bell shaped distribution we would expect and a reasonable amount of scatter about a mean. The old data has a much broader range of values as well as no central value to the distribution.

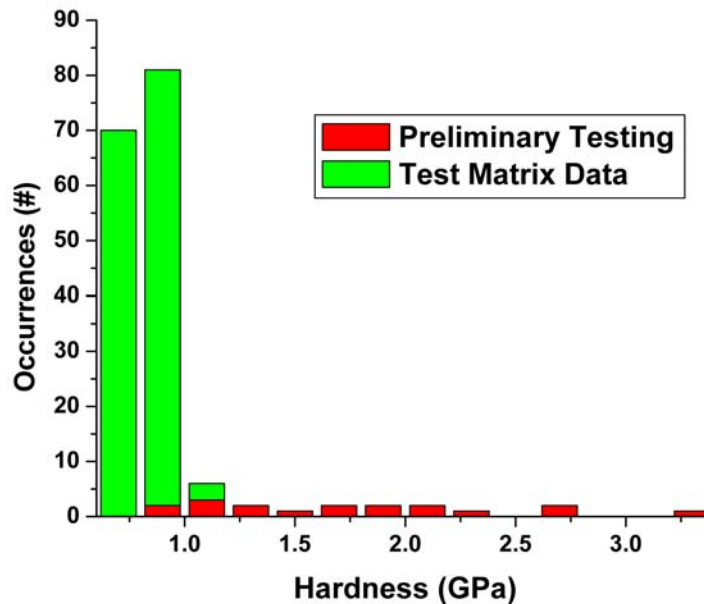


Figure 4- 19 Histogram of the preliminary data plotted with that of the total test matrix (all nine surface preparations). The test matrix data has a bell shaped distribution over a smaller range compared to the scattered distribution of the preliminary tests.

The reason for the consistent measurements or the original cause of the variation is not clear. The test matrix did indicate that the more perfect the structure is the more variable it becomes. When you consider the preliminary testing from this perspective it indicates that the structure was probably closer to perfect, enabling deformation mechanisms that are masked by less ideal structures. One thing that is established is the preparation technique is more robust than originally thought. Dramatic differences in the preparation resulted in only slight shifts in the measured hardness values. Originally we speculated that a defect of a particular length scale must be dominating the deformation behavior. The results of test matrix indicate that this defect has either been removed or is being masked by another. Not only are the measurements far more consistent, but they also yield at much lower shear stresses, indicating a change in deformation behavior.

4.3: Influence of Surface Inconsistencies

Hardness measurements are very sensitive to contact area. In depth sensing indentation, the contact area is assumed based upon the tip displacement and not directly measured. Distortion in the contact area can be caused by pile-up or sink in, surface roughness, and surface features such as steps (changes in contact area are discussed in Section 2.2.1). On the macroscale direct measurement of the contact area allows these aspects to be accounted for. The lack of accurate imaging in most nanoindentation tests makes correction difficult. With repeatable values for hardness tests on flat surfaces, we can begin to investigate the significance of changes in contact area.

4.3.1 Surface Structure

The imaging capability is one of the major advantages of the Hysitron system. While the resolution is not as high as some SPM techniques, it is sufficient to determine the size of most surface features. During the experiment of the test matrix array, indents were often intentionally placed on step bunches of varying size to probe the role of surface structure on measured hardness. Step bunches varied from 0.5 nm to 60 nm in height. Not only is the size of the step important, but the location of the indenter in relation to the top or bottom of the steps is crucial. The indent may be placed on a location below steps. As the tip penetrates the surface the contact area spreads to contact the steps. This results in a larger contact area than predicted by the tip calibration function. If the indent is placed above a step the opposite happens. With increasing depth of penetration the actual contact area becomes smaller than the predicted value.

Figure 4-20 is a comparison of two indents done on the same surface. **Figure 4-20 (a)** and **(c)** are the before and after images of an indent placed on a relatively flat surface. **Figure 4-20 (b)** and **(d)** are the before and after images of an indent placed on the low side of a step bunch. **Figures 4-20 (e)** and **(f)** are cross sections of the before indent images with the location of the indent indicated by arrows. These images help to visualize the topography of the indented region. The arrows show that the steps were changing the contact area from the moment of contact. **Figure 4-20 (g)** is a cross-section of the stepped region, which measures the step height to be approximately 12 nm. **Figure 4-20 (h)** is the load displacement data for each of these indents. The indent placed on the step has a 12% decrease in the depth of penetration which results in an 18% increase in calculated hardness. The reason for the reduced depth of penetration is the increased contact area. The load is applied over more area, decreasing the localized stress. This results in less deformation and therefore an increased measured hardness.

When an indent is placed on the high side of a step bunch, it influences the hardness in the opposite direction. **Figure 4-21** is the comparison of two indents done on the same surface, one on a flat surface the second on the high side of a step bunch. **Figure 4-21 (a)** and **(c)** are the before and after images of an indent placed on a relatively flat surface. **Figure 4-21 (b)** and **(d)** are the before and after images of an indent placed on the high side of a step bunch. **Figures 4-21 (e)** and **(f)** are cross sections of the before

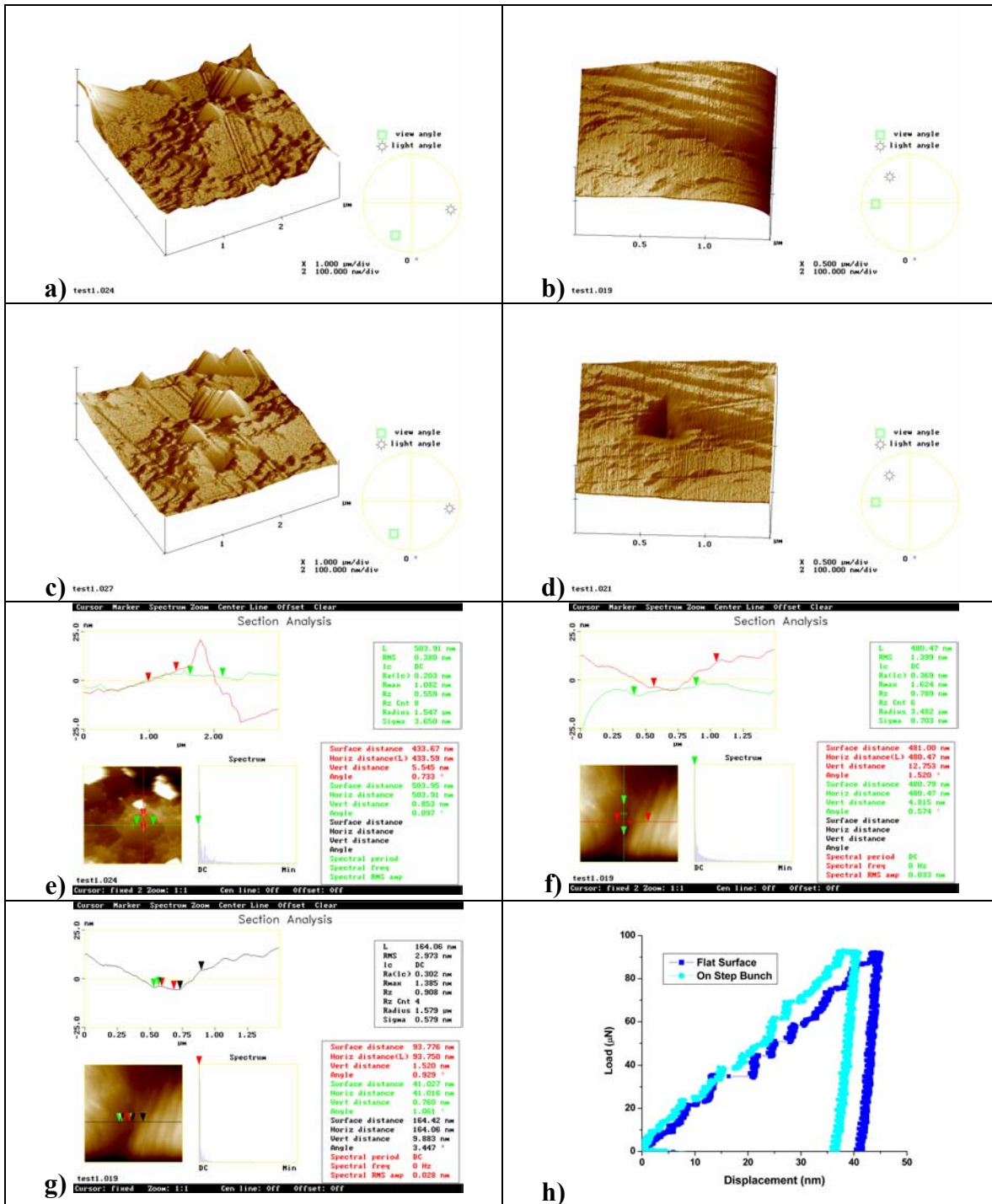


Figure 4- 20 Comparison of two indents done on the same testing surface, one on a flat terrace, the second on the bottom side of a step bunch. a) Surface image before indentation test on flat surface. b) Surface image of step bunch before indent. c) Surface image post indent on flat surface. d) Surface image of surface post indent on step bunch. e) Image cross section of flat surface, area of indent defined by arrows. f) Image cross section of flat surface, area of indent defined by arrows. g) Image cross section measuring step height, dimensions of which are given in the legend. h) Load-Displacement data for two indents pictured. The increase in contact area due to the step decreases the force per unit area, resulting in a calculated increased hardness compared to the test done on a flat surface.

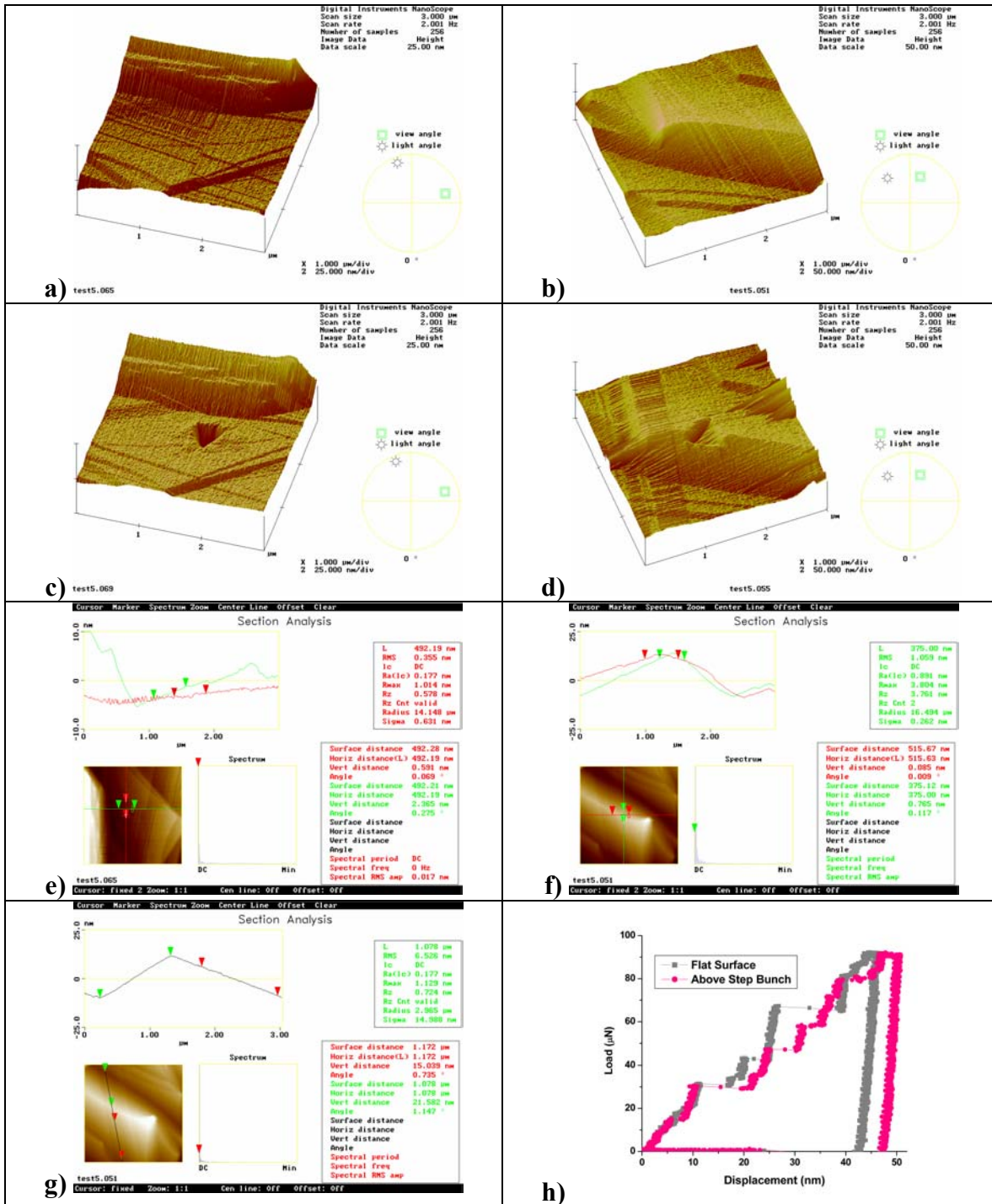


Figure 4- 21 Comparison of two indents done on the same testing surface, one on a flat terrace, the second on the high side of a step bunch. a) Surface image before indentation test on flat surface. b) Surface image of step bunch before indent. c) Surface image post indent on flat surface. d) Surface image of surface post indent on step bunch. e) Image cross section of flat surface, area of indent defined by arrows. f) Image cross section of stepped surface, area of indent defined by arrows. g) Image cross section measuring step height, the dimensions of which are given in the legend h) Load-Displacement data for two indents pictured. The decrease in contact area due to the step increases the force per unit area, resulting in a decreased calculated hardness compared to the test done on a flat surface.

indent images with the dimensions of the indent indicated by the four arrows. These images again help to visualize the topography of the indented region. This image clearly demonstrates that the indent was placed on the very edge of the step bunch. **Figure 4-21 (g)** is a cross-section of the stepped region, which measures the step height to be approximately 35nm. **Figure 4-21 (h)** is the load displacement data for each of these indents. The indent placed on the step has a 9.1% increase in the maximum depth of penetration which results in a 12.7% decrease in calculated hardness. The reason for the increased depth of penetration is the reduced contact area. The load is applied over a much smaller area, increasing the localized stress. This results in more deformation and therefore decreases the measured hardness.

These two examples demonstrate some of the most significant changes in the mechanical properties due to surface features. The steps on the surfaces had a range of sizes. In order to better understand the influence of these steps we categorized the indentation tests into five groups. The first is a flat surface with no identifiable surface features. The next group consists of any steps involved in the indented area that were at under a nanometer in height. The next size range was features between 1 and 10 nanometers in height. There were numerous surface features on our samples that had heights over 10 nanometers and they composed the fourth group of tests. The fifth group was indents that involved regions that had been damaged due to imaging by the probe tip. Scratching often masks the role of the surface feature that is involved in the indentation test. Surface scratching will be discussed more extensively in the second half of this section.

Figure 4-22 is a histogram of all of the test matrix data categorized by size of feature. Indents placed on flat surfaces have a very tight distribution. If indents are placed on steps, even as small as a fraction of a nanometer, the distribution is broadened slightly. The peak broadening is continued as the steps get larger in size. Eventually, when the feature size is large enough, the population has no obvious center and a very broad distribution. As previously demonstrated the placement of the indenter, on the high or low side of a step, can decrease or increase the measured hardness significantly. The size of the feature influences contact area, as does the distance from that step. If the indenter is further from the step edge it will have less of a change in the contact area compared to an indent done immediately on top of the same step. It is very easy to visualize the steps influence on contact area. The hemispherical deformation cavity that is produced by the displacement of material required to make room for the tip is also influenced by the discontinuity in structure due to a step. The shape of the cavity will change as will its ability to constrain the deformed material.

Also shown in the histogram is the change in measured hardness due to surface scratching. Scratch was not a factor we set out to investigate, but on occasion it did occur. In these cases the imaging scratches the surface, work hardening it and therefore significantly increasing the measured hardness. The hardness increase is correlated to the extent of scratching. Scratching is usually identified before it becomes too severe. It follows that the largest number of affected tests would be only slightly harder than an unscratched surface and continues to taper off as the induced damage becomes more apparent to the operator.

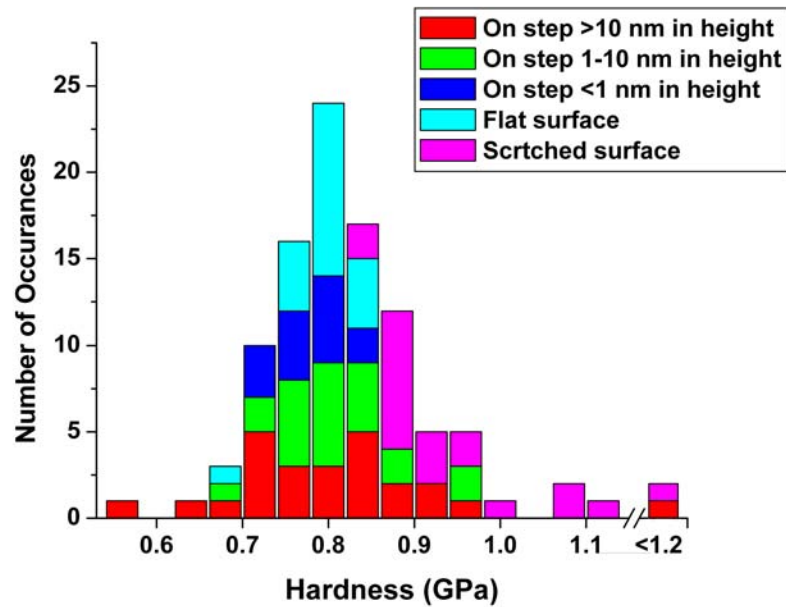


Figure 4- 22 Histogram showing the influence of different ranges of step height on hardness measurements. Flat surfaces have a normal distribution. As the steps get larger they broaden the distribution. When the steps get large the distribution has no identifiable peak. Scratching in these experiments work hardened the surface, as demonstrated by the increase in hardness measurements.

Keily and Zimmerman [71, 72] from Sandia National labs have also investigated the role of steps on the mechanical properties of gold using IFM and EAM. Keily's experiments were on a slightly smaller scale using tips with radii between 25-230 nm, looking at steps between 0.5 and 3.0 nm in height. The steps significantly change the yield load of the material. What is interesting is they found the yield strength to be equally influenced by being on the high or low side of a step. The distance from that step was the most important parameter. Zimmerman also found that contact area can be dramatically changed by the presence of a step. They found that steps have longer range influence than originally thought. The hemispherical zone of deformation has a significant role in mechanical response. They normalized much of their dimensional findings by the tip radius to facilitate comparisons between scales. They found that an indent placed within three times the tip radius of a step would have a noticeable change in the yield strength of gold. If this is scaled to the dimensions of our tests, this requires step free terraces of nearly 2 μm . Terraces of this size are extremely rare even on the highest quality surfaces. According to their results almost every indentation test we make is influenced by a step.

In our experiments there was no noticeable change in the yield strength. All indents yield in the same load region independent of the presence of steps. The changes in hardness due to the influence of steps are significant. Inaccurate predictions in contact area and changes in shape of the deformation cavity broaden the distribution of the measured hardness, masking an identifiable center. Indents done on large surface features have a hardness distribution similar in shape to that seen in the preliminary results. There are two important attributes to keep in mind. First, not all of the preliminary results involved surfaces features that measured over 10 nm in height. Below

this size, the indentation hardness still has a normal distribution. The role of steps was indistinguishable in those experiments. Second, the distribution increase due to steps is significant but not as large as that shown in the preliminary results. Often when the surface feature is over 20 nm in height, the feature is often larger than the indent itself, indicating the spread in distribution will not continue to grow with increasing feature size.

Surface features have the ability to broaden the distribution of measured hardness due to changes in actual contact area (both positive and negative) from that predicted by indenter displacement. This indicates that the surface structure most likely contributed to the sporadic measurements reported in the preliminary results. The surface structure does not tell the whole story for it does not explain the significantly higher loads required to initiate plastic deformation. The role of surface steps in measured hardness is difficult to quantify, although qualitatively it dramatically influence property distribution.

4.3.2 Surface Scratching

Surface roughness is another factor that has a significant influence on indentation data. At the nanoscale the irregularities in sample height can be a significant portion of the overall depth of the indent. Very often the cause of roughness also induces a large number of near surface dislocations. Not only does the roughness change the contact area from that which is predicted by the probe displacement, but interactions of dislocations change the deformation behavior. That is one of the reasons that surface preparation for nanoscale mechanical property tests is so important. The extent of surface preparation can have a dramatic influence on the smoothness of a surface and the dislocation density, which in turn have significant influence over the measured hardness.

Figure 4-23 (a) shows a series of indentation tests done on a gold single crystal after mechanical polishing. The sample does not demonstrate the staircase loading associated with the same crystal after it has been electropolished and flame annealed. The data has significant distribution in the test results caused by the surface roughness. The same surface is one of the mechanically polished surfaces plotted **Figure 4-23 (b)**. This demonstrates that if the same surface is loaded further, to depths well beyond the dimensions of the surface roughness, the measurements are repeatable. Load-displacement data for a second mechanically polished surface and one that has been electropolished and flame annealed are also plotted **Figure 4-23 (b)**. The average measured hardness for the mechanically polished surfaces is 1.20 GPa. The average measured hardness for the electropolished and flame annealed surface is 0.64. This is almost a factor of two differences in measured hardness. The dislocations created by mechanically polishing quickly work harden the sample causing this dramatic increase in measured hardness. This clearly demonstrates the important role of surface preparation, the scale of roughness, and the influence of the starting dislocation density.

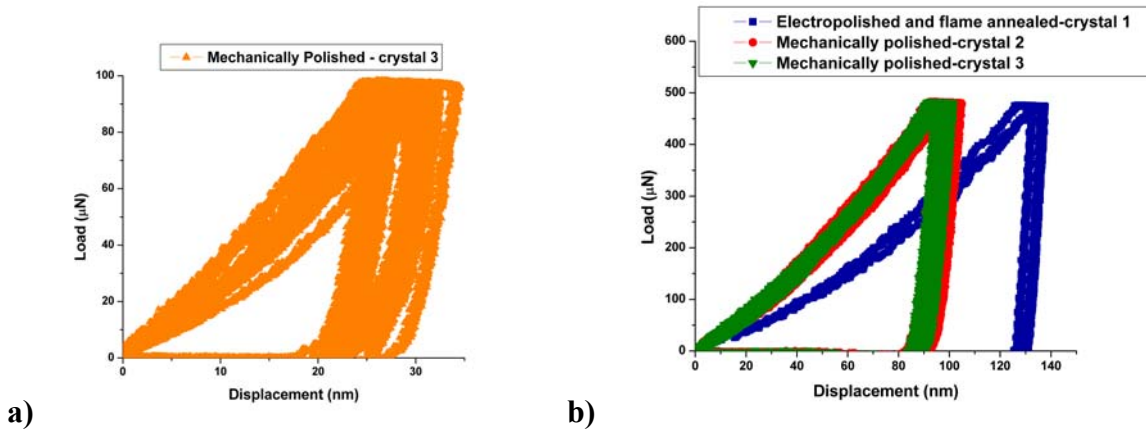


Figure 4- 23 a) Load displacement data on a mechanically polished surface. The variability in response to applied load is caused by the fact that the roughness is a significant portion of the overall displacement. If the load is increased, the variability will be reduced if the depth is beyond the scale of the roughness (as shown by measurements on same surface in b). b) Load displacement data for three different crystals. Two of the crystals were mechanically polished prior to testing. The third sample is electropolished and flame annealed after the mechanical polishing. The mechanically polished surfaces have nearly twice the measured hardness compared to the electropolished and flame annealed sample.

Nanoindentation data has many complicated aspects that may influence the calculated mechanical properties. One aspect that is often overlooked is the contact associated with locating the surface, a very important part in measuring relative displacement of the probe tip. This initial contact must cause some deformation, the extent and nature (whether it is elastic or plastic) is material and instrument dependent. In the Hysitron system, the location of initial contact is not only the point of contact at the location of the indent but the whole imaged area.

The Hysitron utilizes contact AFM to image the surface. The load is input by the operator and the software applies a constant load. The plates in the three plate capacitor have a tendency to drift with local changes in temperature. Any drift by the probe will not be compensated for by the software. When the probe drifts away from the surface, the applied load is less than anticipated. The load is increased when the probe drifts closer to the surface. If the probe drifts away from the surface, the image resolution is reduced dramatically. In some material systems when the probe drifts toward the sample it can damage the surface. The ability to cause damage is controlled by the sample material, probe radius, and the input imaging load. Gold is very soft and therefore scratches easily, making it sensitive to the two other parameters. The probe tip we use is very broad, with a radius of approximately 325 nm. Sharper tips in our possession (radius of approximately 100 nm) scratch the surface no matter the imaging load. Even with a very broad tip, the imaging load must be very carefully monitored when testing soft materials such as gold. Thermal drifts as well as sample height changes limit the low end range of applied imaging load. If the set point is too low, the probe loses contact with the sample too quickly, and full images are unable to be captured. The set point we use for all imaging gold with the blunt Berkovich indenter is 800 nN; this load is high enough to maintain contact with the surface and low enough to not damage the surface. A small drift in the transducer stack can result in a 50% increase in the imaging load.

The load is still in the range that is commonly used to image most materials, but results in damage to the gold surface.

If the applied load is too high the probe tip will deform the surface as it images each line. If this happens at a high enough load or for sufficient passes it will result in material pileup at the edges of the image area. **Figure 4-24** is a $6\mu\text{m} \times 6\mu\text{m}$ image of a gold surface. The probe tip had drifted closer to the surface during prior $3\mu\text{m} \times 3\mu\text{m}$ images, scratching the surface and creating piles of material at the edges of the scan area. The scratching has destroyed some of the smaller features such as the step bunches visible outside the previously imaged region.

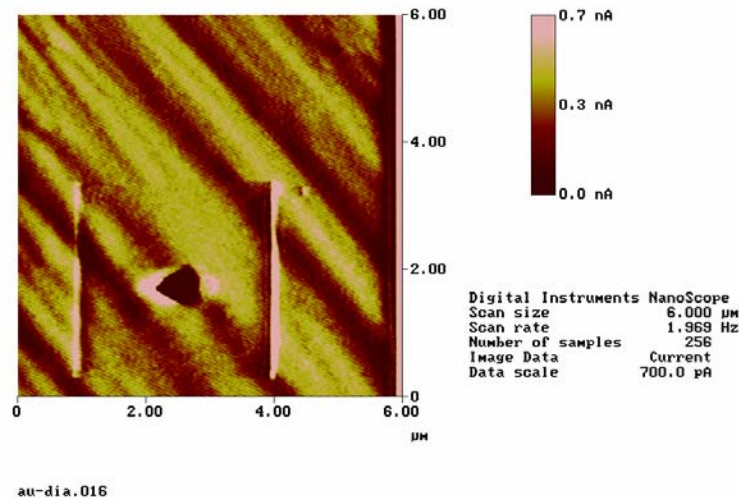


Figure 4- 24 Surface image, $6\mu\text{m} \times 6\mu\text{m}$, taken by Berkovich indenter during nanoindentation testing. Previous images, $3\mu\text{m} \times 3\mu\text{m}$ in dimension, have caused surface damage due to a drift in applied imaging load. The scratching results in the destruction of small surface features such as step bunches, an increase in roughness, and piles of excess material at the edges of the imaged region.

Scratching can have a dramatic influence on measured mechanical properties. **Figure 4-25** shows load displacement data taken with a sharp Berkovich indenter during preliminary testing on gold. Due to the sharpness of the probe tip, it scratched the surface even at very low contact loads. These particular indents were not imaged before and after so the details of each test is not known, but extensive scratching is known to have occurred. Lack of imaging means that the damage due to the tip is at worst a line caused by indexing to a new spot. This means that the surface could be perturbed, but it is unlikely that the surface has experienced the work hardening often caused by the rastering of the imaging process. We speculate that the one shallow indent was done in an area where the tip had drifted sufficiently far from the surface that it was not damaged before the hardness test was performed. The scratched surfaces have an average hardness of 0.746 GPa, which is slightly lower than the average of the selected test matrix values which 0.806 GPa. The reduction in measured hardness is due to the surface being perturbed, slightly decreasing the contact area. The unscratched surface has a measured hardness of 2.48 GPa, which is in the range measured by the preliminary tests shown in **Figure 4-4**.

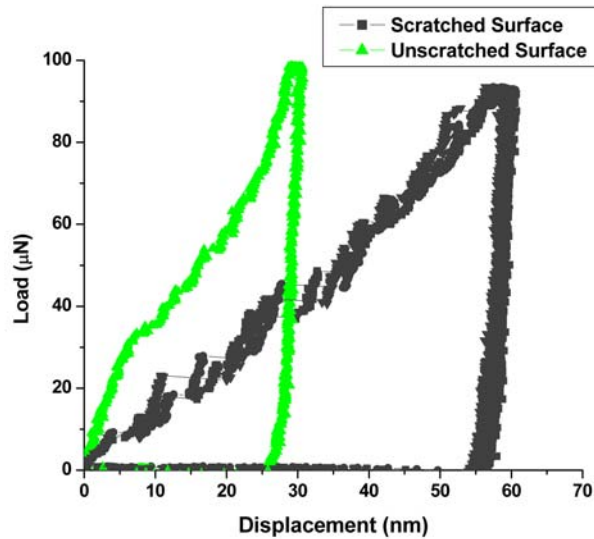


Figure 4- 25 Load displacement data taken during preliminary testing with a sharp Berkovich indenter. The majority of the tests occurred on surfaces that had been roughened by scratching of the probe tip. One indent demonstrates significant elastic loading prior to deformation. The surface is most likely undamaged prior to testing.

In this case the induced roughness makes the material appear softer. This is the opposite of the influence from mechanical polishing. This can be explained by the difference in surface roughening and work hardening. The indent on the area that was not damaged prior to testing has nearly linear loading for over the first 30 μN . The resulting maximum shear stress is 4.1 GPa, which is well within the range of theoretical shear strengths when resolved in the plane most likely to slip. Looking again at **Figure 4-23**, when a material is work hardened the loading slope increases, but it will never be as steep as an elastic loading curve. The scratching can also induce surface roughness. Out of plane deformation can decrease contact area compared to that predicted by the displacement of the probe, meaning the localized stress is increased and there is more deformation at a lower load. This would explain why the scratched surface appears softer than even the test matrix data. It is obvious from the materials ability to sustain load elastically (the high yield load) that this particular sample had a very low initial dislocation density. The surface scratching in this case was more of a surface roughening than a work hardening.

Scratching initially roughens the surface and eventually leads to work hardening. The progression of which is correlated to the initial dislocation density. The more dislocations present, the more quickly the material will work harden due to their interactions. If the surface continues to be deformed, it will begin to work harden. As is shown in the histogram in **Figure 4-22**, all of the surfaces that experience a high imaging load experience work hardening as opposed to roughening, demonstrated by the increased hardness for all of these surfaces. The increase in hardness is correlated to the extent of damage done by the tip. **Figure 4-26** shows the before and after images of two indents from the test matrix experiments as well as the load displacement data. One of the indented surfaces has suffered moderate to severe surface damage due to imaging. An undamaged surface from the same testing conditions is shown for comparison. **Figure 4-**

26 (a) and **(c)** are the before and after images of the undamaged surface, while **Figure 4-26 (b)** and **(d)** are the before and after images of the scratched surface. **Figure 4-26 (e)** and **(f)** are top views of the post indent images shown in height and current mode. While damage is evident in **Figure 4-26 (e)** it does not have the linear edges seen in **(f)**, indicating it is a result of the hardness test and not damage due to imaging. The surface scratching has resulted in a considerable difference in the measured hardness. The overall shape of the curves is the same, but there is a 15% decrease in depth of penetration for the scratched surface. This results in a 22% increase in calculated hardness. This is a moderate case of scratching. Depending upon the amount of transducer drift the damage can be worse and some cases have even a more subtle surface roughening. This is the opposite of what was observed in the previous example but confirms the influence of initial dislocation density. The scratched surface in the test matrix work hardens as opposed to the surface roughening that occurs in the previous example. This can partially be explained by the fact that the test matrix sample has had the probe cover the entire surface, while the preliminary testing only had the damage due to indexing the indenter to the location of testing. The test matrix sample had more opportunity to form and operate any induced dislocations. The observation that the undamaged test matrix surface does not sustain an elastic load comparable to that seen in preliminary testing, reinforces the theory that the test matrix surface has a higher initial dislocation density than the surfaces originally tested.

Scratching is not always easy to recognize because the deformation from one pass can be very subtle. It takes a large load or numerous passes to cause the extent of damage to a surface seen in **Figure 4-24**. It is even more difficult to determine scratching in post indent images for the indent itself often perturbs the surface. One way to identify and even quantify the damage done by the probe tip is surface roughness measurements. **Figure 4-27** are roughness measurements taken before and after the indents shown in **Figure 4-26**. The roughness analysis was done to small regions of the images, indicated by the boxes drawn on the surface. These regions are very small for two reasons. The first is to avoid surface steps. The second reason is to avoid including information that is distorted by the noise of the instrument. The instrument noise manifests as the straight lines that run through every image. The noise changes the displayed height and can have a dramatic influence on the calculated RMS value. The goal is to try and compare similar surface regions. **Figure 4-27 (a)** and **(b)** are roughness measurements taken just prior to testing. The mean roughness for these two surfaces is 0.154 nm for the undamaged surface and 0.201 nm for the scratched surface. After indentation, in the area that had been previously imaged a number of times, the RMS has increased to 0.193 for indent unscratched surface and 0.285 nm for scratched. While the RMS value increased dramatically for even the scratched surface, this can be attributed to the damage done by the indentation test. The roughness from an area outside the previously imaged area for both indents is used for comparison. These areas measure 0.150 nm for the unscratched surface and 0.163 nm for the scratched. On the scratched surface the roughness near the indentation is nearly twice that of the area outside the previous images. This is considerably higher than that measured for the unscratched surface. Significant changes in the Root Mean Square of the height values can indicate if scratching has occurred.

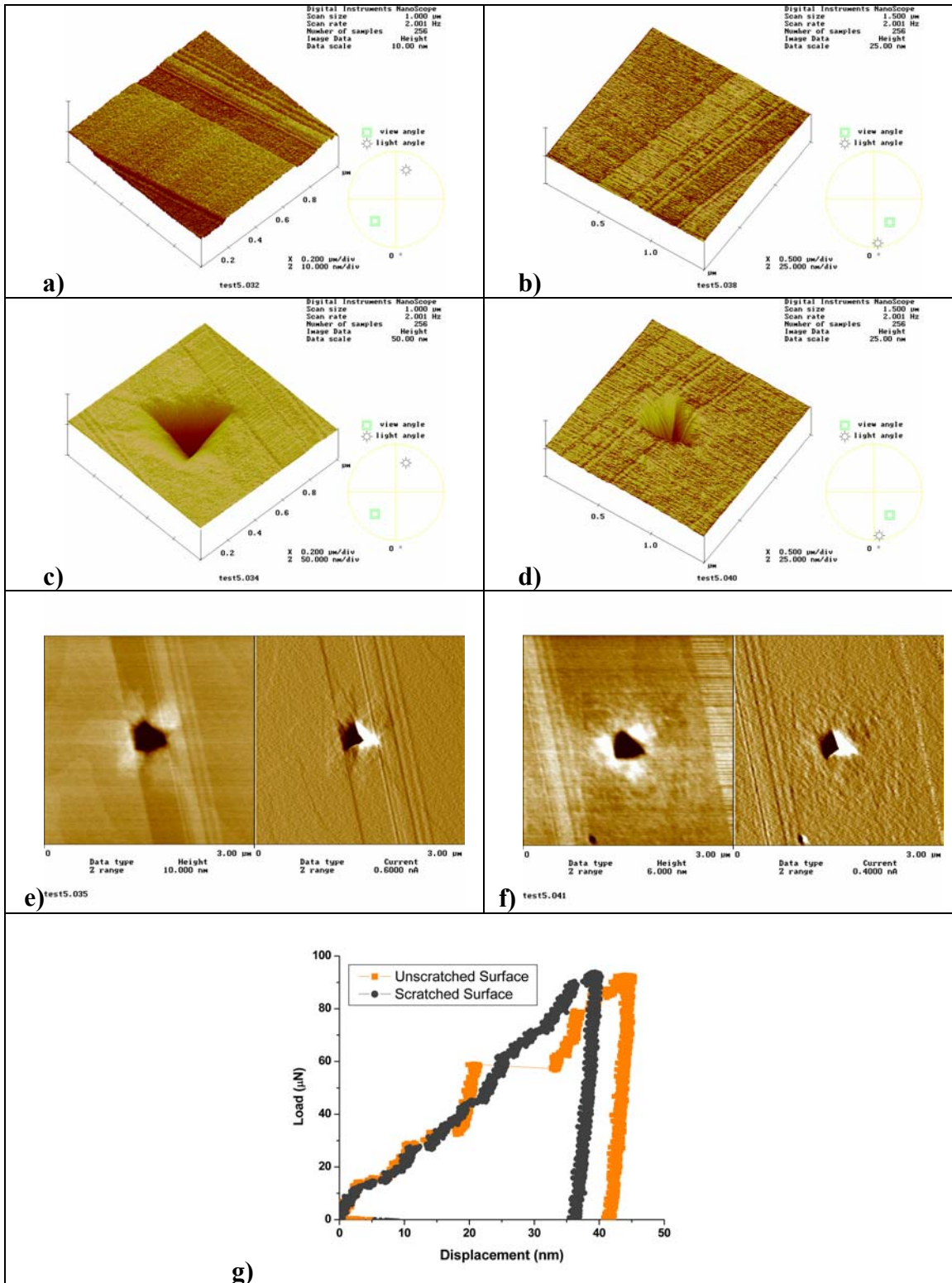


Figure 4- 26 Surface images taken by indenter probe a) before indent on undamaged surface b) before indent on scratched surface c) after indent on undamaged d) after indent on scratched surface e) surface height and current images after indentation of undamaged surface f) height and current images after indentation on scratched surface.

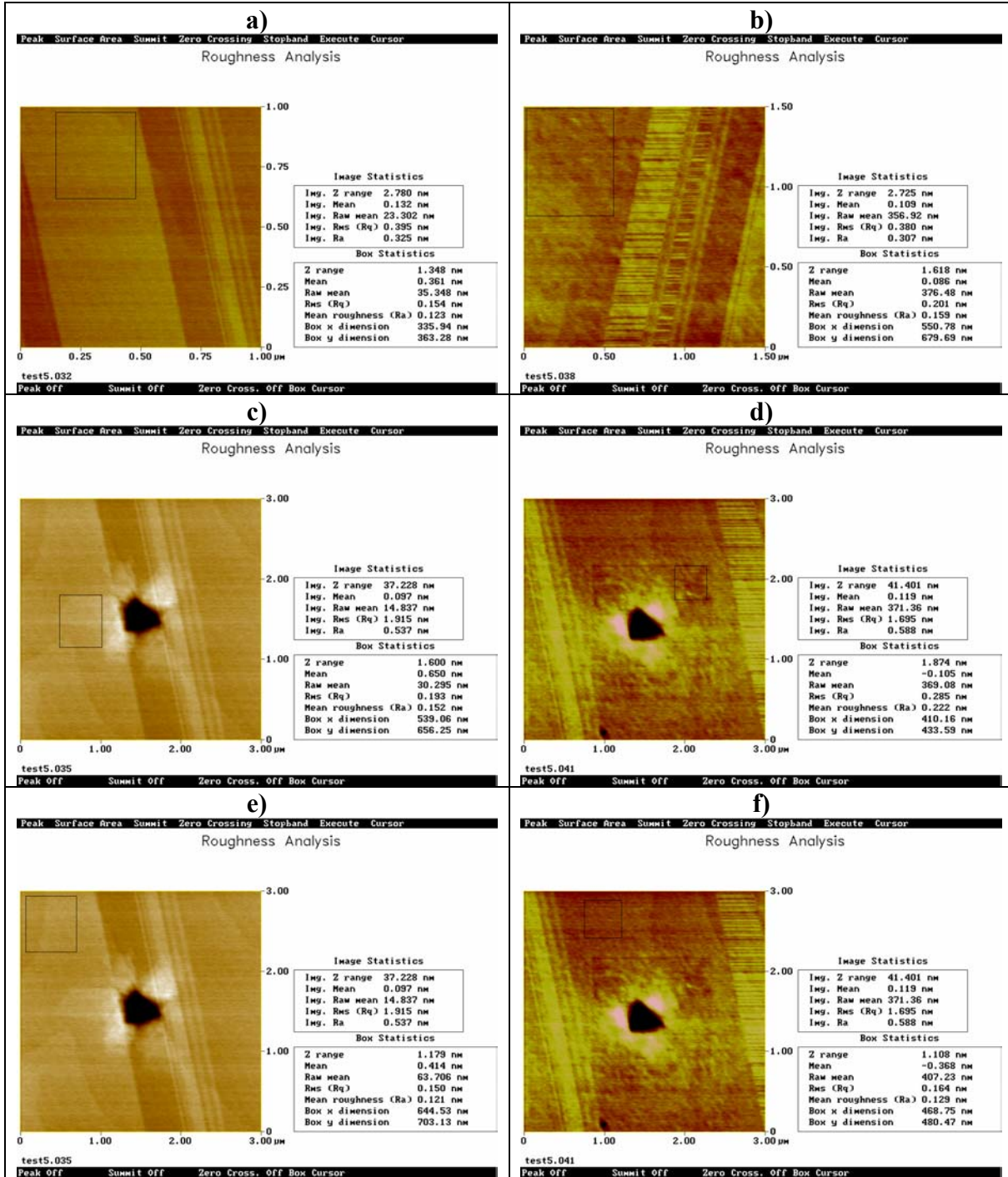


Figure 4- 27 Roughness determination from a) before image of unscratched surface b) before image of scratched surface c) after image of unscratched surface in zoom region d) after image of scratched surface in zoom region e) outside the zoom region on unscratched surface f) outside zoom region on scratched surface.

Comparing indentation tests enables the gathering of clues as to why surfaces have differences in mechanical behavior. Scratching by a probe tip can roughen a surface, eventually leading to work hardening. This can lead to confusion for roughening causes a reduction in measured hardness due to changes in contact area, while work hardening results in increased measured hardness. When there is a higher concentration of dislocations in a sample, the material will work harden faster. Surface roughness calculations can help alert us to the presence of surface scratching due to dislocation interactions. Surface roughness can change the mechanical response of a material, which means we must first know how an undamaged surface behaves before we can recognize the altered behavior. These examples also demonstrate the importance of initial dislocation density on measured hardness.

4.4 Ex-Situ Electrochemical Modification

4.4.1 Air Exposure

The original purpose of this research was to try and investigate the influence of a controlled monolayer deposition on the surface of a single crystal. Tests done by Corcoran et al demonstrated that significant changes in mechanical properties could be caused by slight surface modifications [5]. The idea for electrochemically altering the surface was inspired by the fact that measurements on gold surfaces that had been exposed to the air for a number of days displayed considerable variation on a surface that had previously behaved repeatably in indentation measurements. Upon analyzing these samples they discovered that the surface was covered in a thin organic layer. The fact that an absorbed organic monolayer could induce such noticeable variability in the measured mechanical properties of gold, lead the investigators to modify the surface in a more controlled manner. Corcoran et al. [15] used electrochemistry in order to ensure a clean surface and add to the surface in very discrete ways. They tested gold surfaces with an oxide layer, a lead up layer, a silver up layer, and a reconstructed surface.

Our initial measurements (described in Section 4.1) demonstrated extreme variability much larger than that observed by Corcoran, caused by an organic surface layer [5]. Once the crystal began to behave in a repeatable manner (described in Section 4.2), we decided to see if we too had an influence due to air exposure. After one of the experiments in the test matrix was complete, we left the crystal out, exposed to the environment for an extended period of time. While we did not observe the increased variability that was previously reported, we did find significant changes in the yield behavior. **Figure 4-28** shows load displacement data for three different surfaces. **Figure 4-28 (a)** is the load displacement data for Test 5 from the test matrix. The surface preparation conditions for this test were four cycles of electropolish after the mechanical polishing. The flame annealing durations is 15 min after each of the four electropolishing cycles. The crystal was also annealed in a furnace for 63 hours in a furnace purged with Argon. The data set shown in **Figure 4-28 (b)** is taken after the sample was left out 6 days after initial testing. Because Test 5 is an annealed sample and therefore was not freshly cleaned prior to test another experiment was performed on a freshly cleaned surface, the results of which are shown in **Figure 4-29 (c)**. The crystal was not electropolished so there was no additional material removal, just an additional 15 flame anneal.

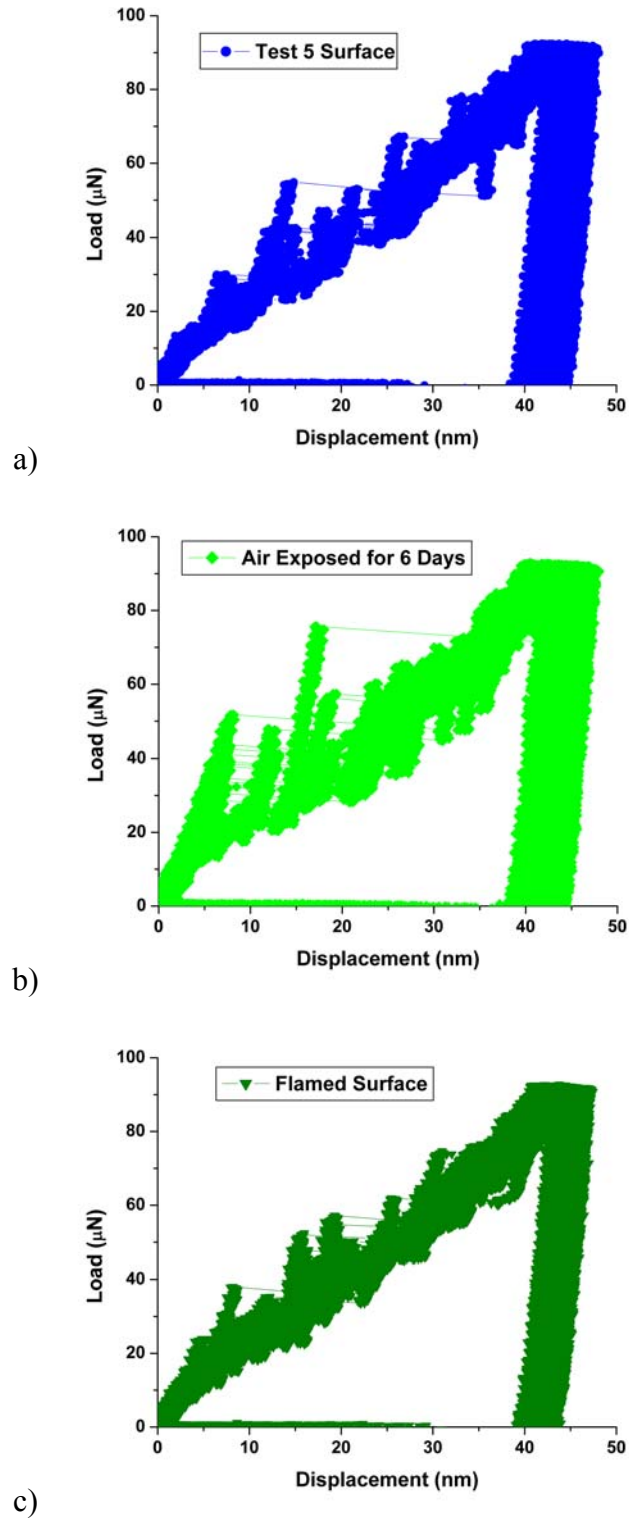


Figure 4- 28 a) Load-displacement data for surface preparation defined by test 5 from the test matrix b) Load-displacement data for the same surface after being exposed to the air for six days. c) Load displacement data for the same surface after it has been flame annealed (cleaned). The exposure to air significantly changes the initial yield strength of the sample.

	Test 5 Surface	Air Exposed	Flamed Surface
Yield Load (μN)	13.4 ± 3.4	31.4 ± 10.1	13.4 ± 3.6
τ_{max} (GPa)	1.79 ± 0.13	2.36 ± 0.27	1.79 ± 0.15
Maximum Depth (nm)	46.3 ± 1.3	45.5 ± 1.5	45.4 ± 0.9
Hardness (GPa)	0.745 ± 0.4	0.767 ± 0.043	0.771 ± 0.028

Table 4- 4 Average values for the property measurements from the indentation tests shown in Figure 4-28.

The results from the furnace annealed sample and the freshly cleaned surface are nearly identical, indicating the prolonged exposure in the furnace did not contribute to the change in yield behavior. It is readily apparent that the sample that was exposed to the air for six days has a dramatic increase in the loading behavior. The average property values for the three sets of data shown in **Figure 4-28** are given in **Table 4-4**. The average hardness does not change considerably from experiment to experiment. The yield load is increased by 31.8 % when the crystal is left out for six days.

A histogram of the yield loads for all the indentation experiments under the three different surface conditions is plotted in **Figure 4-29**. The values for the Test 5 surface and the flamed surface have very similar Gaussian distributions. The air exposure and the resulting organic layer increase the average yield point and significantly broaden the distribution.

The prolonged air exposure has a noticeable change in the mechanical properties. There was a significant increase in the crystals ability to bear load elastically. This is different behavior than that reported by Corcoran et al. Previously the organic layer absorbed on the surface made the mechanical behavior more variable. In our case the hardness remained consistent. However, once again the influence of a thin organic layer on the surface has recognizably influenced the load displacement behavior of gold.

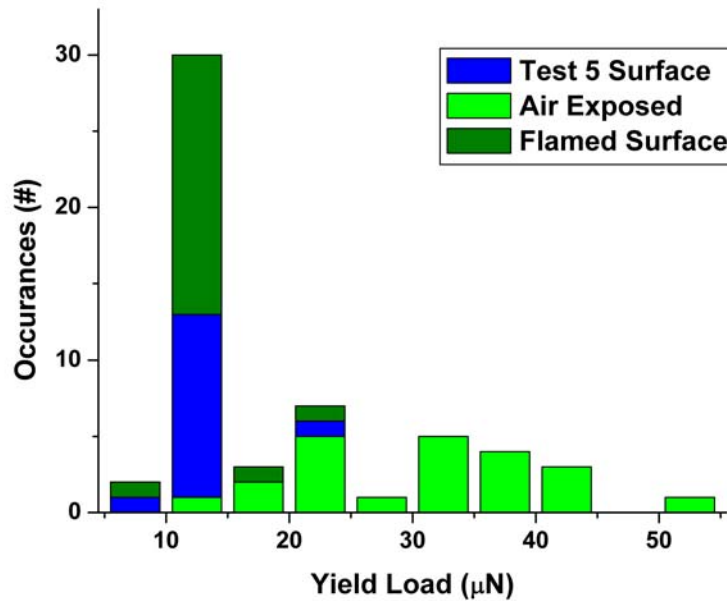


Figure 4- 29 a) Histogram comparing the yield load of surfaces: Test 5 from the test matrix, the same surface after 6 days exposed to air, and the same surface with an additional 15 minute flame anneal to clean the surface. Air exposure increased the measured yield load of a surface.

4.4.2 Indentation of gold oxide

The test matrix proved that gold (111) could demonstrate consistent mechanical behavior. The air exposure tests demonstrated that even subtle surface changes could alter the measured mechanical response. We decided to once again try to modify the surface using electrochemistry. By modifying the surface in a controlled manner we can determine the influence and even quantify changes due to these additions to the gold surface.

The first step is to take a series of indentations on a plain gold surface. **Figure 4-30 (a) and (b)** are the before and after images for the indents performed on a freshly clean gold (111) surface. **Figure 4-30 (c)** are the load displacement data measured on this surface. One of the indents has been highlighted as a representation of the average indentation curve. The yield load and final depth of penetration are similar to those measured for all of the test matrix surfaces.

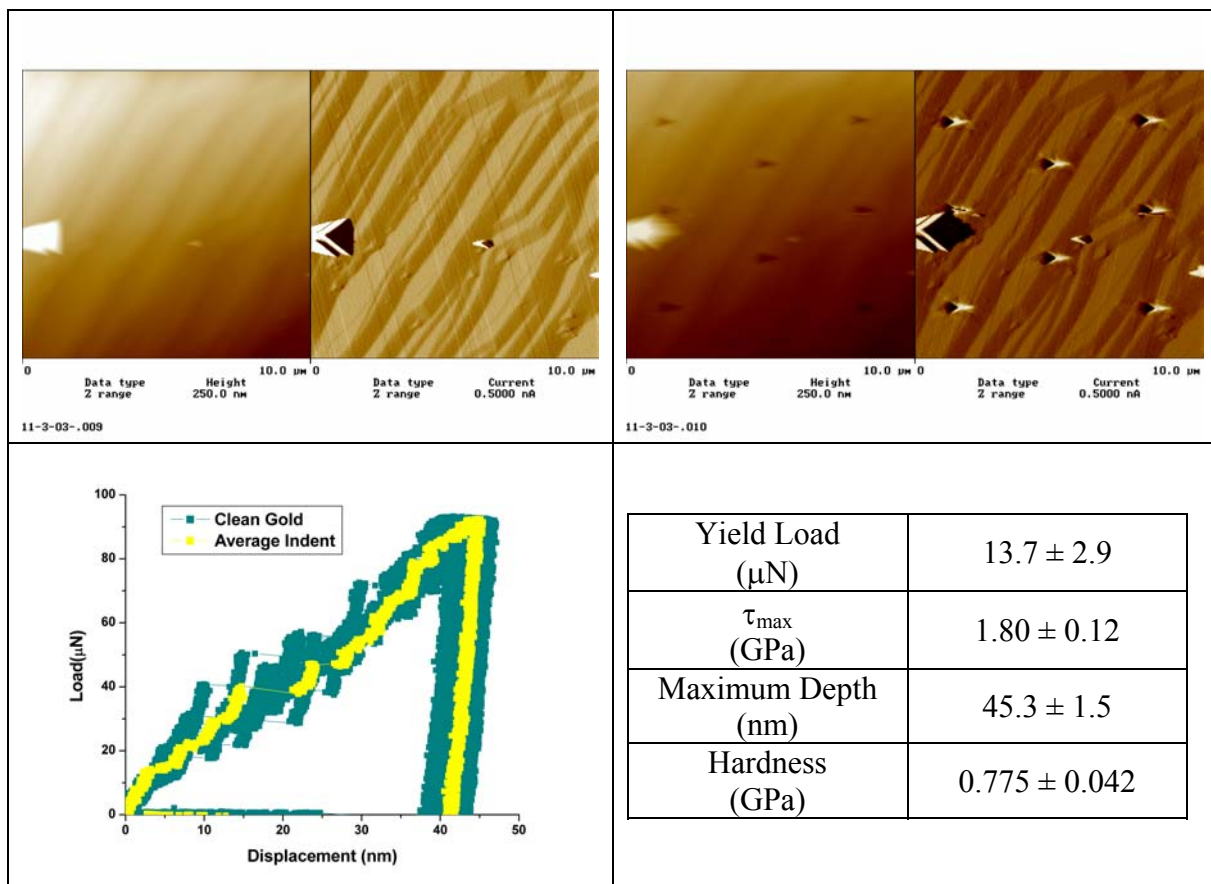


Figure 4- 30 Freshly cleaned gold (111) surface: a) Image before indentation testing b) Image after indentation testing c) Load displacement data for pictured indents d) average important property values for indentation tests.

After this crystal was tested mechanically it was placed in an electrochemical cell. **Figure 4-31** is a cyclic voltamogram of the gold crystal in an electrolyte 1.0 mM Pb (ClO_4) + 0.1 M HClO_4 . Gold electrochemistry and cyclic voltamograms are discussed more thoroughly in Chapter 2 Section 3. The voltage is cycled from 0.05 V to 1.8 V versus a platinum counter electrode. At 1.45 V versus a platinum counter electrode the gold begins to oxidize as evident by the increase in current density. The lead in the electrolyte does not influence the gold behavior at voltages this high. The cell was disconnected at a voltage of 1.75 V, in the region associated with the initial monolayer of oxide growth [73]. The crystal was rinsed with water and dried with a kimwipe. The gold oxide surface was then mechanically tested ex-situ.

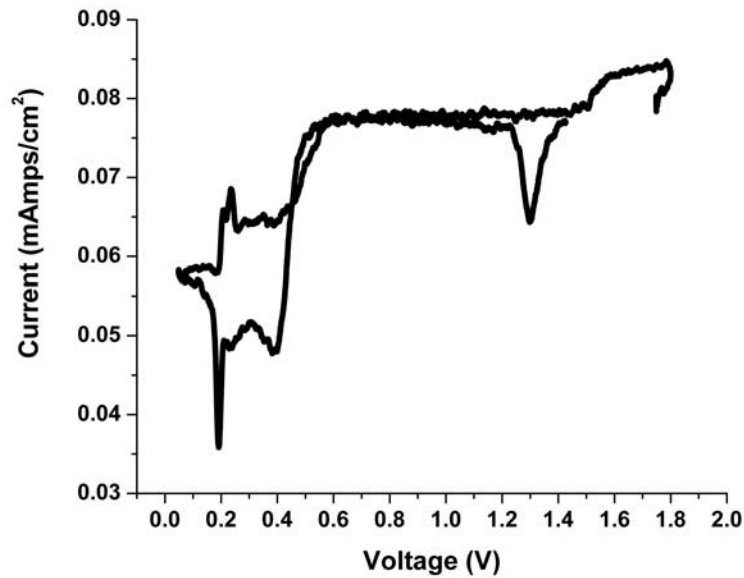


Figure 4- 31 Cyclic Voltammogram of oxide deposition on gold (111) surface in 1.0 mM $\text{Pb}(\text{ClO}_4) + 0.1 \text{ M HClO}_4$. The voltage is cycled between 0.05 V and 1.80 V versus a platinum wire counter electrode. The cell is disconnected at a voltage of 1.75 V, leaving the oxide monolayer on the surface.

Figure 4-32 (a) is an image of the oxidized gold surface. **Figure 4-32 (b)** is the surface post indentation testing. The load-displacement data is plotted in **Figure 4-32 (c)** and the important average property values are shown in **(d)**. A representative indentation curve is again highlighted. The average yield load, and thus the maximum shear stress, has increased considerably. For the plain gold surface the average yield load is $13.7 \mu\text{N}$, or an average maximum shear stress of 1.80 GPa. The oxide layer increases the average yield load to $47.7 \mu\text{N}$, or an average maximum shear stress of 2.73 GPa. This surface layer has increased the average maximum shear stress to initiate plastic deformation by 51.7%. The presence of a gold oxide layer has also increased the average hardness from 0.775 GPa to 0.979 GPa, a 26.3% increase. Again, we should note that the significance of this result is that a surface layer approximately 0.5 nm in thickness is influencing the mechanical properties for an indent that is 35 nm deep. This behavior is not seen for microindentation data on appropriately scaled thick coatings.

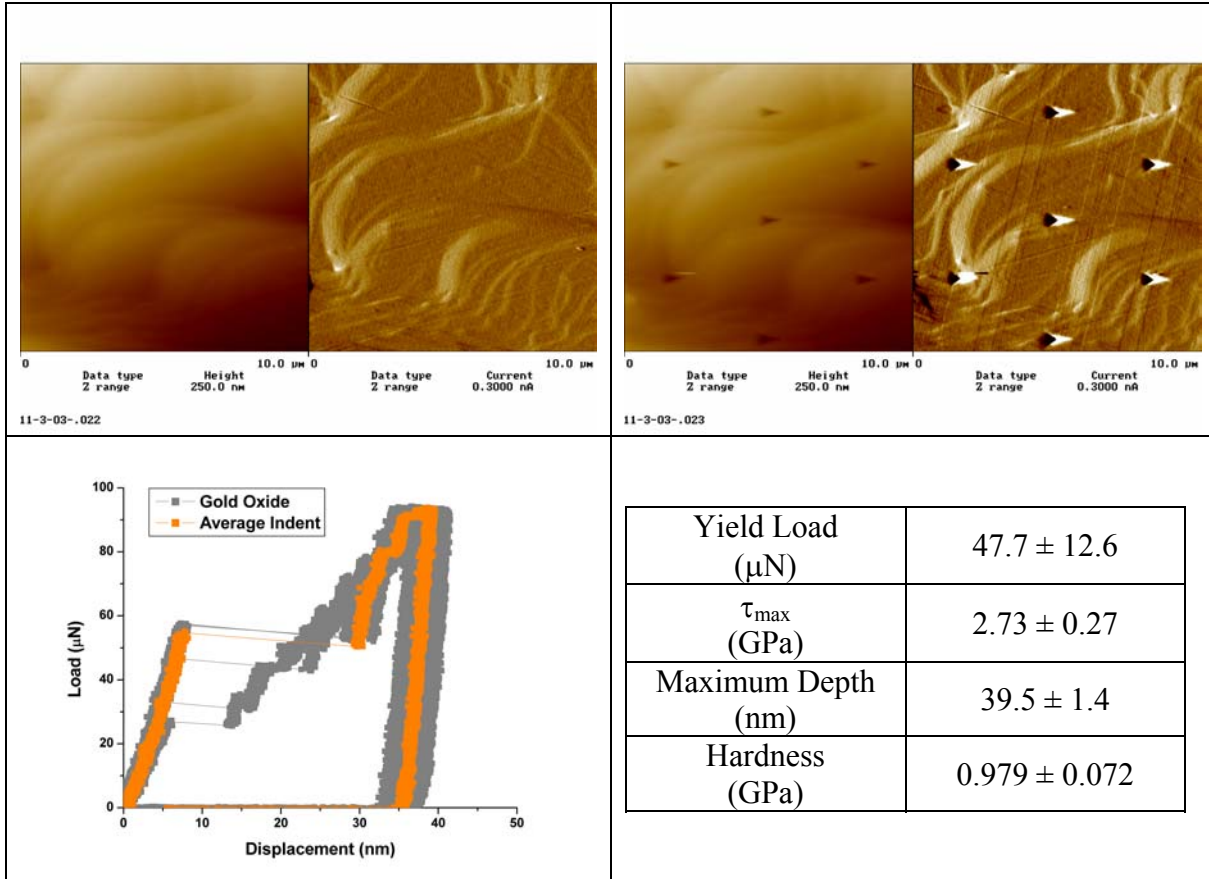


Figure 4- 32 Oxidized gold surface: a) Image before indentation testing b) Image after indentation testing c) Load displacement data for pictured indents d) average important property values for indentation tests.

In order to verify that the change in mechanical properties is not a result of surface changes caused by the electrolyte and applied potential the oxide was removed by placing the crystal back in the electrochemical cell and electrochemically reducing the oxide. The crystal was rinsed, dried, and again mechanically tested ex-situ. The before and after surface images are shown in **Figure 4-33 (a)** and **(b)**. The associated load displacement data and the average property values are displayed in **Figure 4-33 (c)** and **(d)**. The mechanical properties have once again changed dramatically. The average yield load for the stripped gold surface is 26.9 mN, which is a 43.6% reduction from the oxidized surface. The yield load is still a bit higher than the clean gold surface. The measured hardness is 0.840 GPa, which is a 14% reduction from the oxidized surface. This is still over 8% higher hardness than that measured on the plain gold surface. The difference in property values between the clean gold surface and the surface stripped of oxide can be attributed to the reactions that have occurred on that surface. Electrochemical reactions like oxidation are known to perturb or roughen a surface. The first monolayer of gold oxide also experiences a turn over of the anions in order to minimize repulsion. The before and after images show a surface that looks slightly perturbed compared to the images shown in **Figure 4-30**.

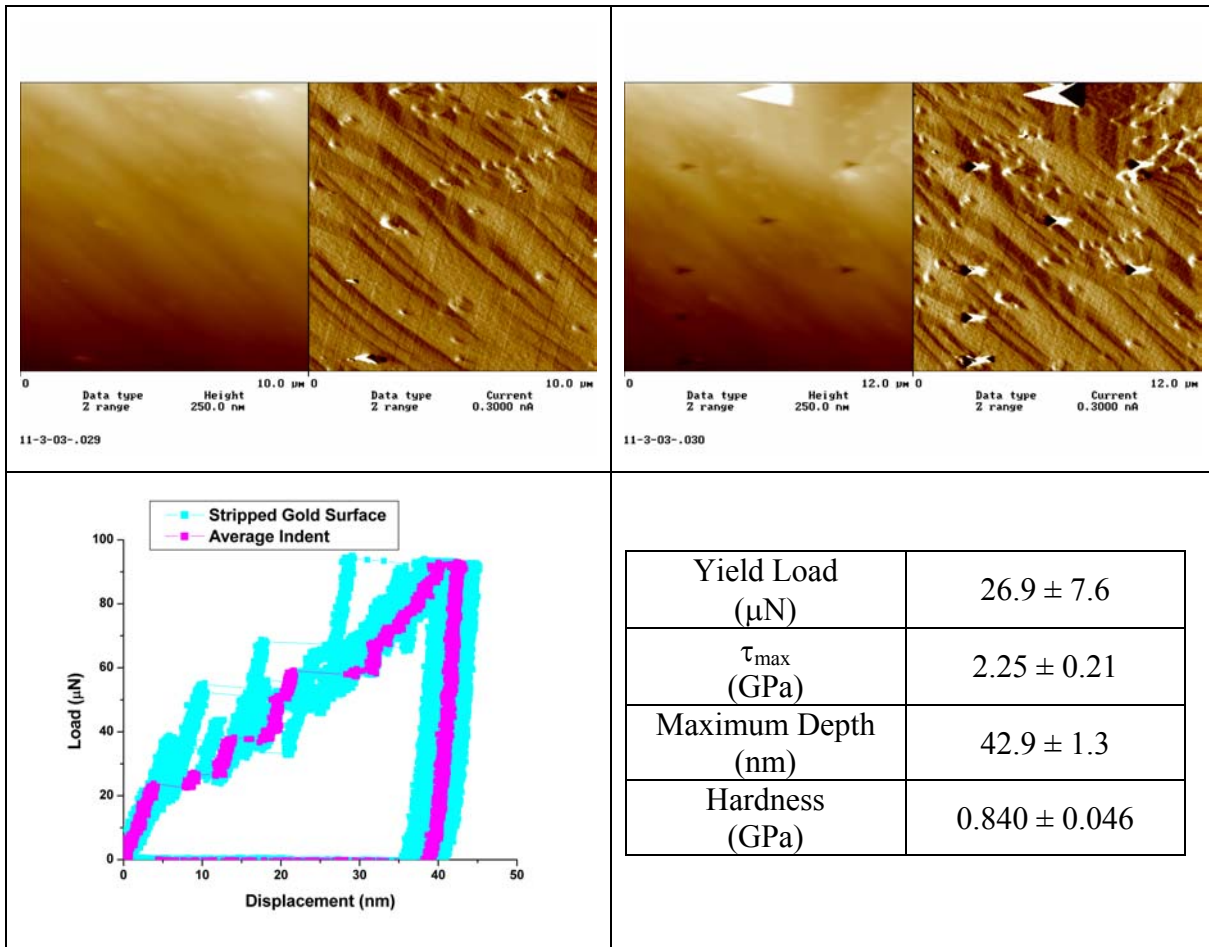


Figure 4- 33 Gold (111) surface stripped of oxide: a) Image before indentation testing b) Image after indentation testing c) Load displacement data for pictured indents d) average important property values for indentation tests.

Figure 4-34 shows the average indents for the three surfaces plotted together. The changes in measured hardness are more readily appreciated by looking at the histogram in **Figure 4-34 (b)**. The oxide layer not only increases the measured hardness but also results in a broader distribution. The removal of that oxide layer returns the property values back to nearly the same values as the original surface. The load at which plasticity initiates has also changed with the presence of a gold oxide. **Figure 4-34 (c)** is a histogram of the yield loads for all the indents taken under the three conditions. The removal of the oxide layer has shifted the values back toward the values for a plain gold surface, indicating that the influence of the oxide is real.

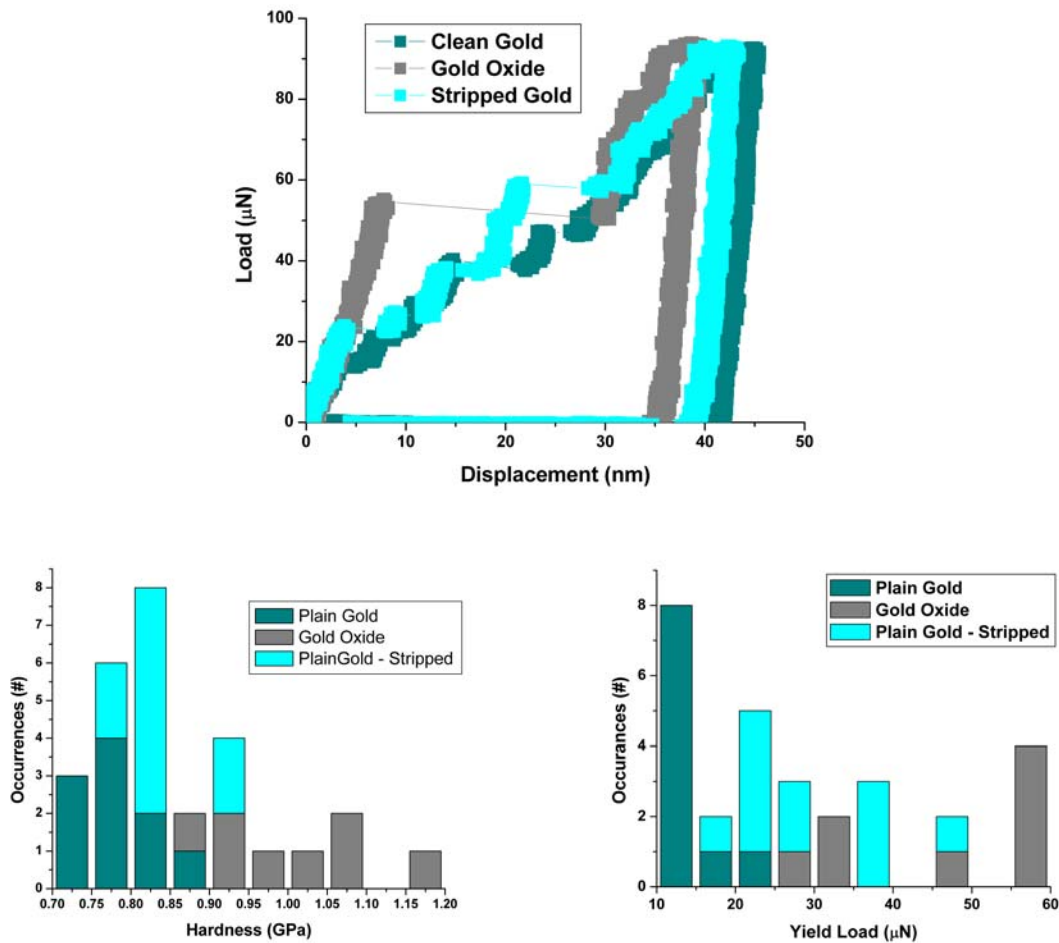


Figure 4- 34 a) Average indentation curve for plain gold surface, gold oxide surface, and plain gold surface after oxide stripped. b) Histogram of hardness values measured under each of these conditions. c) Histogram of yield loads measured under each of these conditions.

There is very little in the literature discussing the mechanical property values of gold oxide (Au_2O_3). Based upon the observation that most oxides are harder than their parent element, it is not surprising that gold oxide is harder than gold. What is surprising is that such a thin layer could have such a dramatic influence on the indentation data. Oxide layers are often ignored in the literature because they are usually a few angstroms in thickness and indents are significantly deeper. This data demonstrates that even a very thin oxide layer can have a dramatic influence on indentation data. We found that this thin oxide layer changed the measured hardness by over 25%. While stripping this oxide layer did not return the exact same measurements, they were appreciably reduced in the direction of the clean surface. The slight changes in property values can be attributed to the fact that one surface was freshly cleaned and the second was exposed to electrolyte and voltage. The change in measured values for the surface with an oxide layer is considerably larger than those caused by surface changes due to electrochemical exposure alone. This reiterates the significance of the surface changes caused by the presence of an oxide layer.

4.4.2 Indentation of lead UPD layer

Oxides have been shown to change the mechanical response of a material; we wanted to investigate the role of some other controlled deposits. Another experiment was performed using the phenomenon of under potential deposition. This is an electrochemical reaction similar to bulk deposition. The most important feature of this phenomenon is that only a single monolayer of the metal ion in the electrolyte is deposited on the working electrode. Some of the specific history and theoretical explanations are discussed in Chapter 2 Section 3.

Before the crystal is modified a freshly cleaned gold surface is tested. **Figure 4-35 (a) and (b)** are the before and after images for the tests performed on the plain gold (111) surface. **Figure 4-35 (c)** are the load displacement data measured on this surface. One of the indents has been highlighted as a representation of the average indentation curve. The yield load and final depth of penetration are similar to those measured for all of the test matrix surfaces and has similar values to the clean surface tested in the gold oxide experiment.

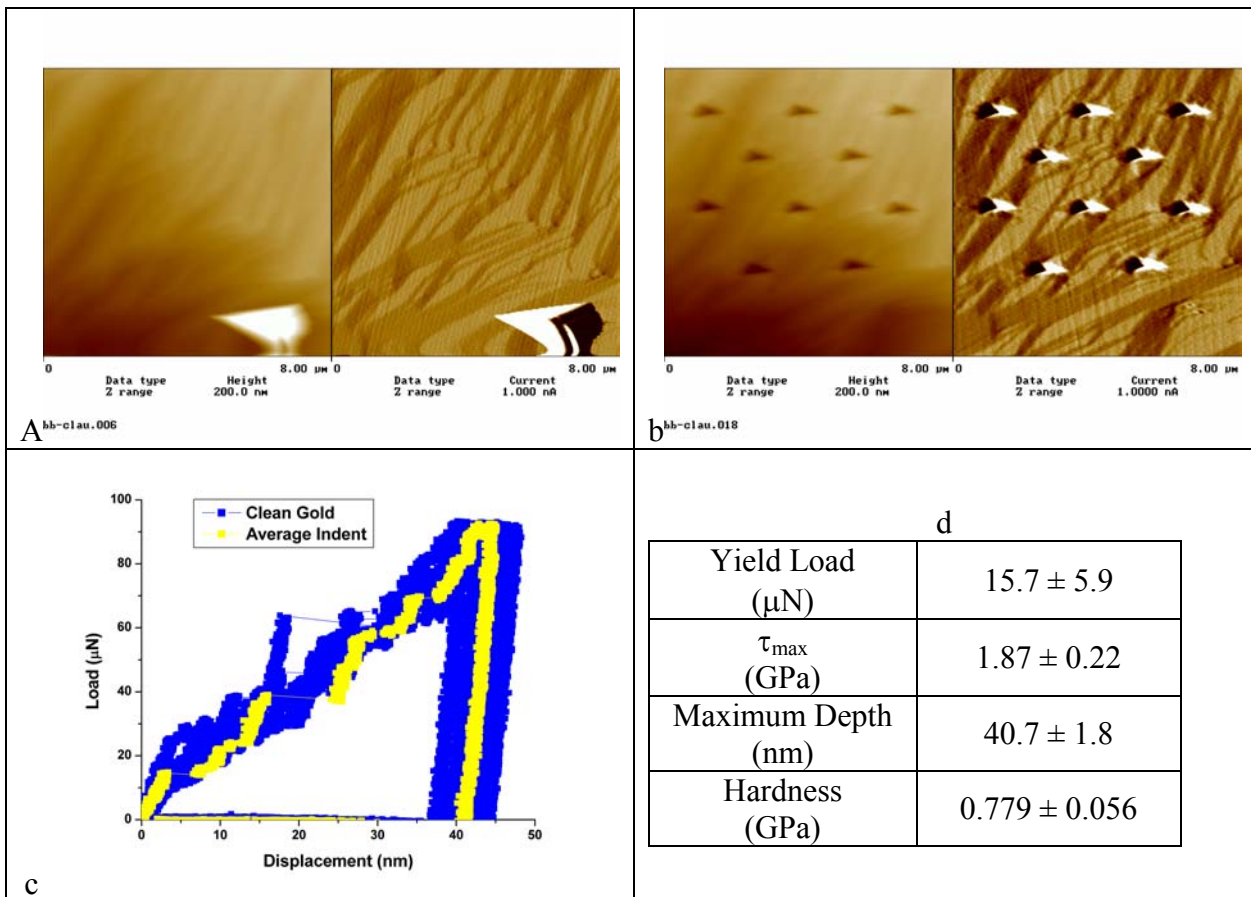


Figure 4- 35 Freshly cleaned gold (111) surface: a) Image before indentation testing b) Image after indentation testing c) Load displacement data for pictured indents d) average important property values for indentation tests.

Under potential deposition only occurs with certain metal pairs. Lead and gold is one such system. The phenomenon is that at a certain potential above that predicted by the Nernst equation, a single monolayer of lead deposits on the gold working electrode. Since the potential is above that for bulk deposition, only a single monolayer is deposited. **Figure 4-36** is a cyclic voltamogram of the gold crystal in an electrolyte of 1.0 mM Pb (ClO_4) + 0.1 M HClO_4 . The voltage is cycled from 1.75 V to 0.05V versus a platinum wire counter electrode. At 0.73 V the lead begins to be deposited, shown by the change in current. After the initial mechanical tests the crystal was placed in an electrochemical cell, in electrolyte containing lead ions and potential applied. The cell was disconnected at a voltage of 0.05 V, leaving the lead monolayer on the surface. The crystal was rinsed with water and dried. Once the lead is exposed to air it forms a lead-oxide (PbO) [86].

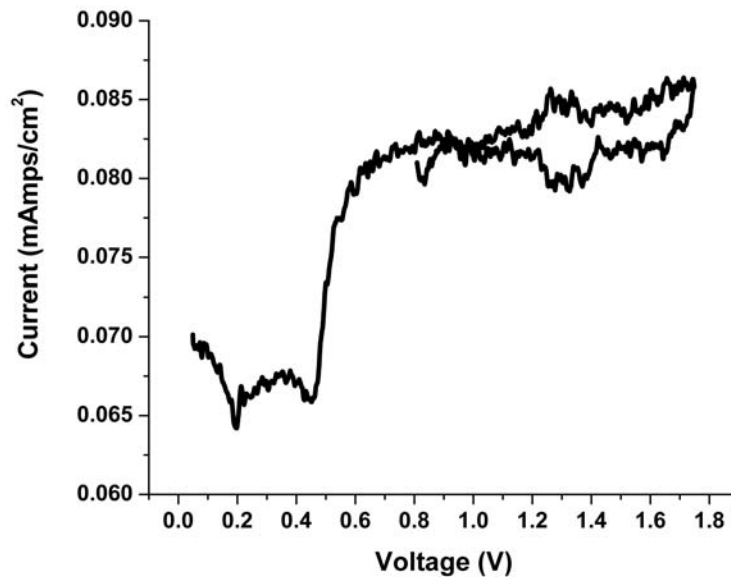


Figure 4- 36 Cyclic Voltamogram of lead deposition on gold (111) surface in 1.0 mM Pb (ClO_4) + 0.1 M HClO_4 . The voltage is cycled between 0.05 V and 1.75 V versus a platinum wire counter electrode. The cell is disconnected at a voltage of 0.05 V, leaving the lead monolayer on the surface.

This lead oxide surface is then mechanically tested. **Figure 4-37 (a)** and **(b)** are the before and after surface images for the load-displacement data shown in **(c)**. A representative indentation curve is again highlighted. The measured mechanical properties are also shown in **Figure 4-37 (d)**. The average yield loads, and thus the maximum shear stress, have increased considerably. For the plain gold surface the average yield load is 15.7 μN , or an average maximum shear stress of 1.87 GPa. The lead oxide layer increases the average yield load to 30.0 μN , or an average maximum shear stress of 2.34 GPa. The surface layer has increased the average maximum shear stress to initiate plastic deformation by 25.1 %. The presence of the lead oxide layer has also increased the average hardness from 0.779 GPa to 0.971 GPa, a 24.6 % increase.

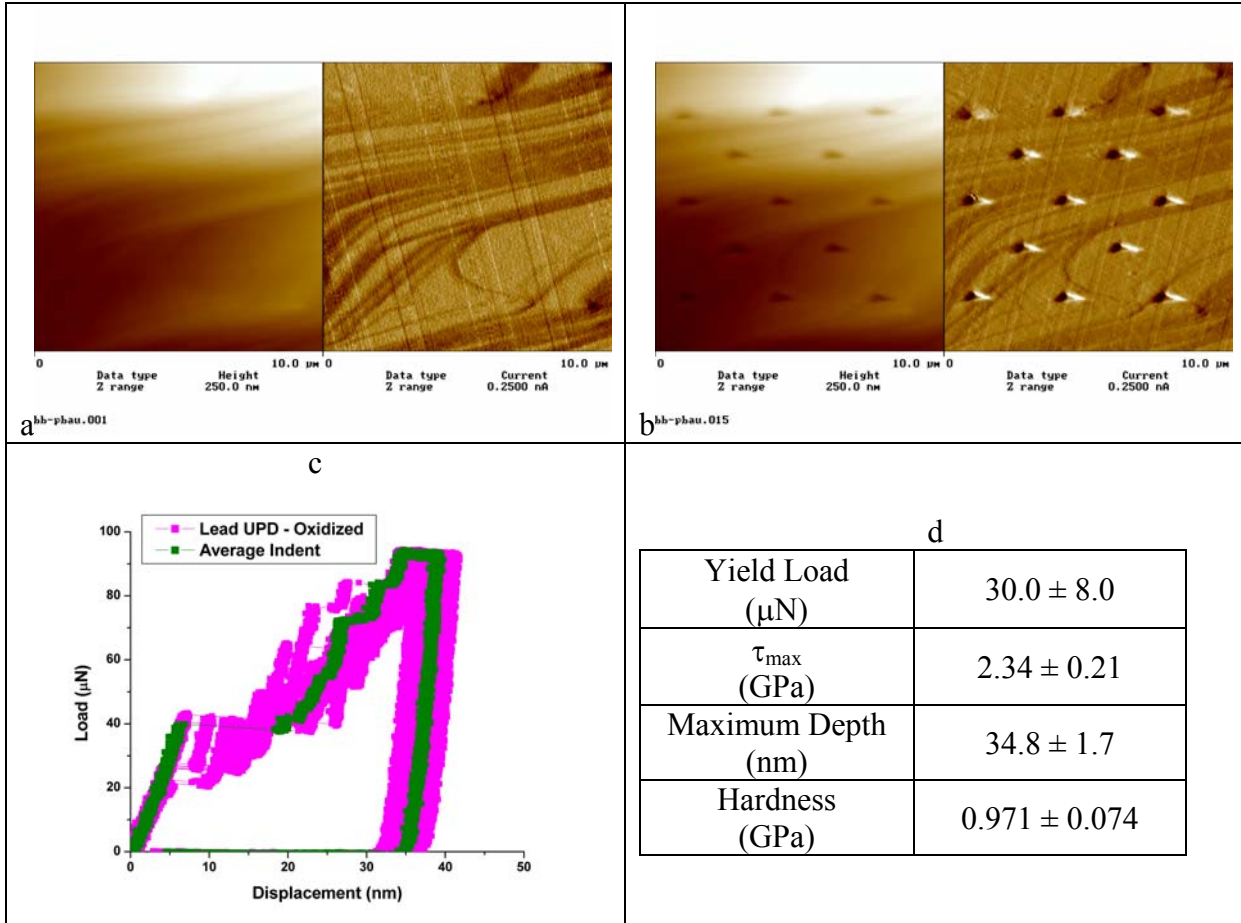


Figure 4- 37 Gold surface with a monolayer of lead on the surface that has been oxidized: a) Image before indentation testing b) Image after indentation testing c) Load displacement data for pictured indents d) average important property values for indentation tests.

For comparison the average indents for both surfaces are plotted together in **Figure 4-38 (a)**. Histograms of the hardness values and the yield load for each of the indentation tests on these two surfaces are given in **Figure 4-38 (b)** and **(c)**. The lead layer has significantly increased the measured hardness, and it no longer displays a Gaussian distribution. The presence of a lead oxide layer has also considerably increased the load necessary to initiate plastic deformation. This is again very surprising that such a thin surface layer could have such a dramatic influence over the measured mechanical properties. This contradicts many of the assumptions made throughout nanoindentation literature.

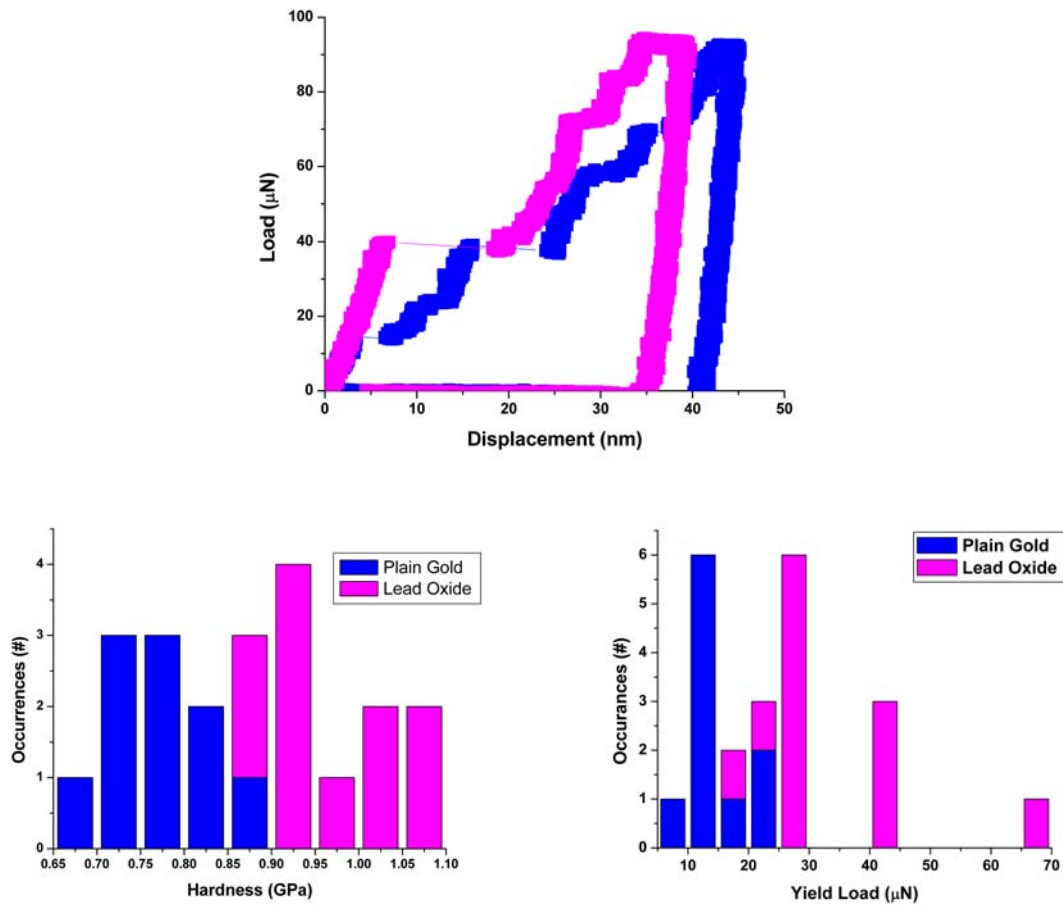


Figure 4- 38 a) Average indentation curve for plain gold surface, lead oxide surface. **b)** Histogram of hardness values measured under each of these conditions. **c)** Histogram of yield loads measured under each of these conditions.

The yield strength and hardness are both significantly influenced by the presence of a gold or lead oxide. They have a similar influence on the measured properties. **Figure 4-39 (a)** shows the average indents for the five surfaces previously discussed plotted together. **Figure 4-39 (b)** is a histogram of the hardness values for all five surfaces. The plain surfaces have very similar property measurements. The oxide layers increases the measured hardness but have much broader distributions. The histogram also shows that once the oxide layer is removed the properties again return to ones similar to the original surface. Very similar observations can be made about the yield load histogram in **Figure 4-39 (c)**. The oxide layers increase the load required to initiate plastic deformation. The distribution of this load required on oxide surfaces is quite sporadic, in contrast to the consistent values measured on the clean gold surfaces. The change in mechanical property measurements caused by the deposition of single atomic layers is quite dramatic.

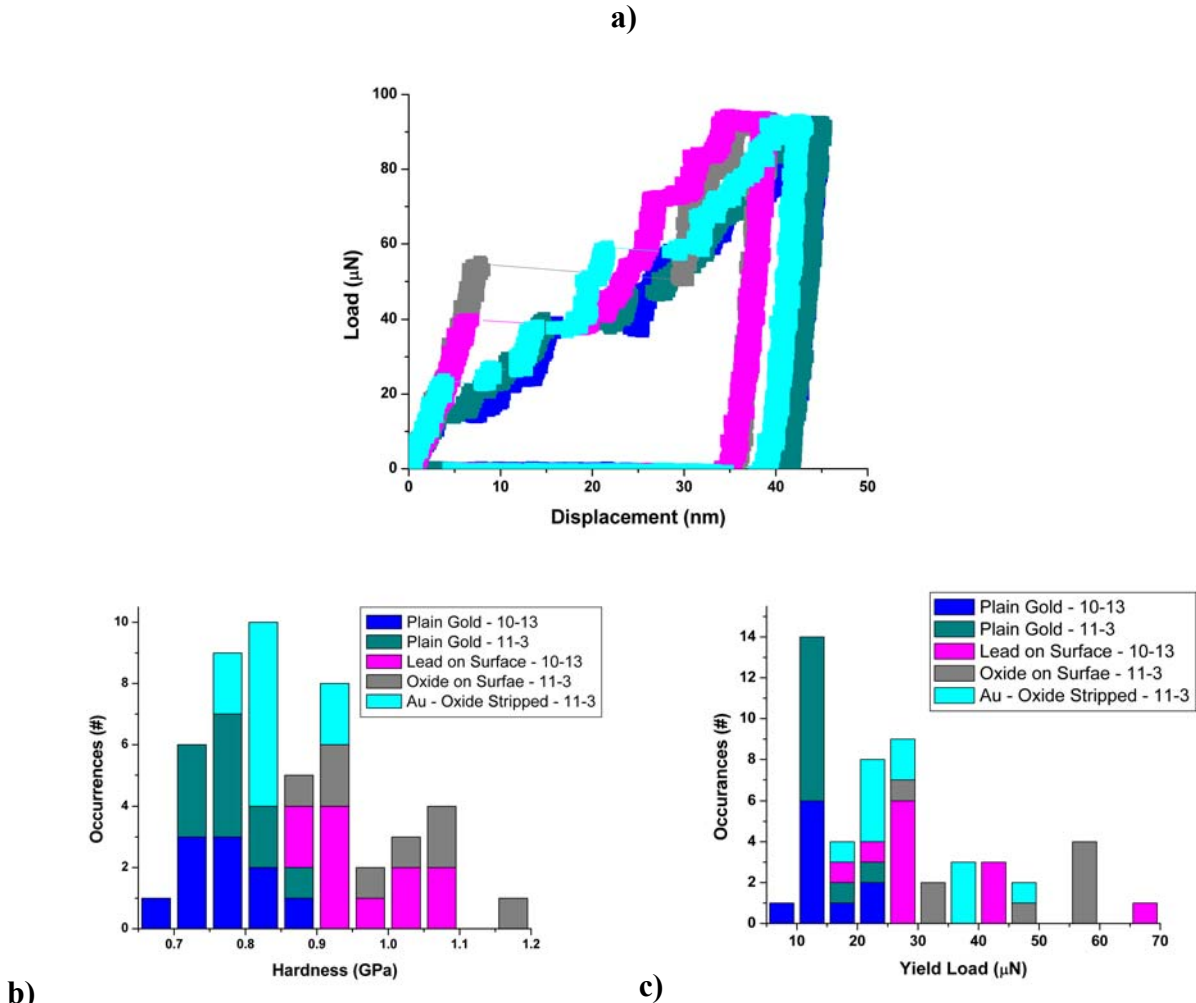


Figure 4- 39 a) Average indentation curve for all electrochemical testing. b) Histogram of hardness values measured under each condition. c) Histogram of yield loads measured under each of these conditions.

Change in measured property values due to monolayer surface changes has been discussed before by Corcoran et al [15]. These results are qualitatively similar, but it is difficult to make direct comparisons between the two sets of experiments for there are significant differences. The first is that those experiments were performed in-situ, meaning the gold surface was in an electrochemical environment during testing. This adds considerable complications due to the applied potential on the surface and increased tip drift from the evaporation of the electrolyte. The lead experiments are particularly hard to compare because the in-situ experiments looked at the influence of lead while our experiments tested lead oxide. The other significant difference is that their experiments were performed with a tungsten tip. They did do some experiments using a Berkovich indenter but found no significant change in the measured mechanical properties. Surface images were not reported in this prior study, so we do not know if the surface was damaged prior to testing. Diamond tips tend to be significantly sharper, and therefore more likely to scratch the surface. The subtle and complex aspects of taking accurate measurements using nanoindentation are exacerbated by contribution of electrolyte. For

example drift occurs more readily and to a greater extent and is therefore difficult to accurately monitor. It is very likely that the previously reported experiments on electrochemically modified surfaces, done with a Berkovich indenter, were performed on scratched surfaces. This would explain why the changes in surface layer have not altered the indentation data. The experiments done by Corcoran et al. and those we have performed both shows the surprising result that small surface changes can dramatically influence mechanical property measurements under certain conditions.

Simulations of indentation behavior indicate that initial dislocation activity occurs subsurface, but any subsequent deformation has a significant influence from the surface. Li et al [67] has used MD simulations to predict that initial deformation requires stresses on the order of gigapascals to initiate deformation. After dislocation loops are created stresses of megapascals are required to operate them, forming numerous dislocations near the surface. Depending upon the testing conditions, surfaces have been shown to both attract dislocations (removing them) and be a source for their nucleation. Feichtinger et al [70] sighted that free surfaces can have a similar affect to grain boundaries, attracting and absorbing many of the dislocations formed during indentation. The change in the surface layer may influence near surface dislocations, preventing their motion. This would significantly alter the measured mechanical properties.

The way in which the layers are deposited ensures that they are less than a nanometer in thickness. The indents have a minimum depth over 30 nanometers in depth. It is very surprising that such a small fraction of the overall indented volume could have such a dramatic influence on the mechanical properties. This demonstrates that surface layers no matter how thin should not be ignored.

CHAPTER 5: SUMMARY AND CONCLUSIONS

Nanoindentation was developed to extend the range of hardness testing to sizes beyond optical resolution to isolate the mechanical properties of thin films, whose dimensions are so small that it is difficult to separate their behavior from that of the substrate. The purpose of the mechanical testing is to assess the quality of a film and its ability to perform in the required environment. Often as scale is reduced materials begin to behave in ways not observed before, for the role of surfaces and defects has become more prominent as tests approach their dimensions.

Gold single crystals were chosen as a model system for surface modification studies because of the electrochemical advantages and the simple structure of the material. Gold is a noble metal, stable in electrolytes of a wide range of pH. The (111) surface is a close packed plane which facilitates the formation of sublattices. These sublattices are instrumental in the submonolayer deposition processes that occur prior to bulk deposition. The single crystal nature of the specimens not only facilitates the electrochemistry, it eliminates any influence due to grain size or grain boundaries. Another advantage to the gold system is the existence of a surface preparation routine that results in surfaces with atomically flat terraces on the order of 100s of micrometers in width.

Initial indentation tests performed with both tungsten and diamond probes displayed a surprising degree of variability for experiments performed on the same sample, only moments and microns apart. All indents displayed extensive elastic loading prior to deformation. The load at which plasticity begins in gold is often indicated by a jump in displacement. This yield load corresponds to a maximum shear stress required to initiate plasticity, which can be compared to the theoretical shear stress required to initiate deformation in a perfect lattice. The onset of plastic deformation in these tests is observed at stress levels on the order of theoretical requirements for dislocation nucleation. The hardness values also span an immense range of values, with the extremes differing by over a factor of two. Although both property values were highly variable they were not correlated, the depth of penetration was independent of this elastic-plastic transition.

There are a limited number of defects in a single crystal specimen of gold, especially on the length scale required to influence nearly every indentation experiment. If the defects are too close they influence every indentation test in an identical manner. If the defects are too far apart they are rarely included in an indented volume. The defect spacing must be on the order of 10s to 100s of micrometers in order to influence nearly every indentation test. We identified four potential defects: residual dislocations, surface structure, vacancies, and impurities.

The indents displayed yield loads on the order required to form a dislocation from a perfect lattice. Applied load falls off as the reciprocal of the distance from the point of contact, therefore a pre-existing dislocation that is further from the location of the probe requires more applied load to operate it. The location, size and interactions of any residual dislocations in the structure play an important role in the material's ability to deform. Surface features can significantly change the actual contact area from that

predicted by displacement, resulting in inaccurate hardness numbers. Structural features can also influence the energy requirements for dislocation formation, acting as barriers to deformation or sources for dislocations. Vacancies are another defect that we initially thought might be involved in the strange deformation behavior. The diffusivities of near surface vacancies are much faster than originally appreciated, and therefore supersaturation is unlikely. Stacking fault tetrahedra are known to exist in quenched gold single crystals so we can not say definitively they are not present in our crystals, depending upon the processing conditions. Our efforts to find such structures were unsuccessful due to difficulties in sample preparation. Impurities are another possible defect. The number and variety of impurity atoms in a sample depends upon the fabrication method and apparatus history. Through experimental means it is not possible to change impurity concentration or distribution and therefore we are unable to specifically identify their role, if any, in deformation behavior. These were the defects that we could readily identify as being able to exist in these samples and of the appropriate length scale, but that does not exclude the presence of others.

A test matrix was designed to change the concentrations of possible defects in a sample by altering some of the surface preparation parameters. In establishing a test matrix three factors were chosen, each at three levels. The levels were chosen based upon sample preparation parameters from the preliminary testing, material availability and the time each experiment would require. For flame annealing duration, the three levels were 5, 15 and 25 minutes. For cycles of electropolishing and flame annealing, the levels were 1, 4, and 8 cycles. The levels for cooling rate were quench, room cool, and furnace anneal. A Taguchi L-9 array was selected to reduce the number of experiments and to concentrate on the factors' influence on measurement variability. The orthogonal nature of the matrix facilitates statistical analysis upon completion of the experiments.

The test matrix results showed some trends in mechanical property values and in repeatability. For each of the matrix test conditions, we identified the five best indents. These were selected based upon the criteria that the surface had not been scratched prior to testing (as best could be determined) and the indent was placed on a relatively flat spot (meaning minimal step bunches involved in the deformed area). This was done in order to compare like surfaces. By selecting an equal number of like indents, the testing conditions are compared more fairly.

The results of these experiments were extremely consistent. The test matrix data demonstrated that under certain conditions the gold surface can have very reproducible results. The largest separation in average hardness between two different surface preparations was nearly 18%. The two extremes, Test 4 and Test 5, had the same duration of flame annealing, but a difference in the number of cycles of preparation. The harder surface had only received one electropolishing cycle. The residual deformation from the mechanical polishing cycle most likely caused this surface to work harden more quickly than others. Test 5 was subjected to the long furnace annealing process, reducing any non-equilibrium defects from the samples. While the difference between the average values is considerable, this appears to be the comparison of two extremes of the same population.

There were also different degrees of repeatability within a given surface condition. Most surfaces displayed very repeatable results. The only exception to this is Test 3, the preparation conditions for which are 5 minute flame-anneal duration, 8 cycles

of electropolishing and flame annealing, and a furnace anneal. The standard deviation was well over twice that of the second most variable surface. This was also the only surface that was able to sustain significant loads elastically. The average maximum shear stress at yield for this test was 2.05 GPa. This is over one and a half times higher than the next closest average. Test 3 was the only surface to sustain loads elastically in the range observed in preliminary tests. This indicates, that although yield point does not directly correlate to the depth of penetration, the general ability to sustain load elastically can cause an increase in variability. The images of the surface show a particularly flat surface with very wide terraces. The preparation parameters are such that the crystal has a significant amount of surface material removed and a considerable amount of time and thermal energy to relax. The high surface quality and the ability to bear load elastically indicate that an increase in variability can be linked to more idealized surface structure.

The Taguchi analysis utilizes a modified Mean Square Dividend (MSD) that is referred to as the signal/noise ratio (S/N). The S/N ratio is averaged for each test done at each factor level in order to identify trends in level influence. The duration of flame annealing increases the repeatability of the indentation tests. This is reasonable for the annealing allows the crystal to remove any non-equilibrium stresses. The number of cycles of electropolishing did not have a linear influence on the measured hardness values. The repeatability was initially increased by increasing the number of times the crystal was electropolished prior to testing. This is expected due to the evidence that not all of the damage caused by mechanical polishing is removed with a single electropolish. Continued electropolishing actually reduces the measurement consistency. The continued removal of material eliminates any long range influence caused by mechanical polishing. Both electropolishing and flame annealing work to smooth the surface. The flame annealing increases mobility to help eliminate non equilibrium defects. The increase in variability indicates that as structure quality improves the way in which that structure responds to loading becomes more variable. The cooling rate also did not display a linear relationship in controlling the variability of hardness measurements. The quenched samples were slightly more variable than the room cooled samples. The most significant influence on repeatability is the annealing of the crystal. Initially this was attributed to the fact that these were the only samples not cleaned immediately before testing. Other researchers have found that crystals left in the air for extend periods tend to absorb an organic layer on their surface, which results in variable hardness measurements [5]. Supplemental testing showed that the hardness was not influenced by the prolonged expose of the annealing process. The experiments also found that the crystal needed to be exposed for a time at least twice as long as the annealing cycle in order to show significant changes in the yield load. The extended duration of the annealing cycle gives non-equilibrium defects the opportunity to annihilate or move to the surface, increasing structure periodicity. The increase in variability with the furnace annealing step reiterates the trends indicated by the number of cycles of electropolishing and flame annealing, that repeatability decreases with structure quality in our system.

Another interesting point is that all of the test matrix results are on the soft side of the hardness spectrum measured in preliminary testing. The yield loads are also dramatically lower in the test matrix study. The changes in surface parameters had resulted in samples that are more easily deformed. This is surprising considering the extensive material removal and thermal history of some of these surfaces. The change in

behavior may be attributed to longer range influence of the mechanical polishing step. When you consider the preliminary testing from this perspective it indicates that the structure was probably closer to perfect, enabling deformation mechanisms that are masked by less ideal structures. We can speculate that conducting further electrochemical and flaming cycles would further increase the variability in measured hardness.

One of the benefits to having repeatable surface measurements is that there is now a reference point to which other tests can be compared. This allows us to investigate and even quantify the influence of surface differences. Surface features were initially investigated as part of both the preliminary experiments and the matrix tests. During initial testing, similar looking surfaces had widely different deformation behavior while similar results were recorded on surfaces with significant differences. It is interesting that unavoidable changes in contact area did not noticeably influence the depth of penetration in preliminary testing. Changes in contact area that were undetectable in preliminary results now demonstrate predictable shifts in hardness values. The matrix experiments showed an increase in distribution corresponding to the size of the feature. The relative placement (on the high or low side of a step bunch) of the indenter tip is crucial in the direction of change of the hardness value. In our analysis we broke the features into three categories, steps under a nanometer in height, steps between one nanometer and ten nanometers and surface features above ten nanometers in height. On flat surfaces the hardness distribution was quite tight. The smallest steps slightly increased the distribution, but still had a Gaussian distribution about approximately the same mean value. The intermediate size steps ($1 \text{ nm} < \text{step} < 10 \text{ nm}$) likewise had an additional spread in the hardness distribution but maintained a similar mean. The largest steps displayed a uniform distribution about approximately the same average value. As the feature became of a comparable size to the indent, the distance from the feature became increasingly important.

If an indent is placed at the top of a large feature, it will dramatically reduce the contact area from the predicted value. The load will be applied on a smaller region increasing the localized stress, causing the material to deform to a greater extent. The example in Chapter 4 comparing two indents made on the same surface displayed a hardness reduction of 12.7% for an indent made on top of steps. We found other examples on some slightly larger features that reduced the calculated hardness by over 25%. If an indent is placed on the bottom of a surface feature, the calculated hardness can be dramatically increased. The applied load is distributed over a larger area and the material appears not to deform as readily as it would if the location were flat. The example in Chapter 4 showed an 18% increase in calculated hardness compared to an indent done on a flat portion of the same surface. Other indents on the low side of a step bunch showed as high as a 60% reduction in the calculated hardness value for an indent with increased contact area due to a step.

An important part of depth-sensing indentation is establishing contact with the surface, which inherently must cause some deformation. Whether this deformation is elastic or plastic is material and instrument dependent. In the Hysitron system the site of initial contact is not the only the location of the indent, but the whole imaged area. Gold is very soft and scratches easily; it is sensitive to the imaging set point and the tip radius. Small transducer drifts often cause damage which at times is very subtle and hard to

distinguish. Only after a repeatable base line was established was it possible to identify the inaccurate measurements due to machine issues.

Once the contribution from small contact area changes was recognizable the ability to monitor and quantify the influence of surface modifications became possible. Original tests under electrochemical control yielded inconclusive results. The variability in the gold masked any influence caused by deposited layers. The test matrix proved that consistent measurements on gold were possible. The first step in determining if surface layers could influence mechanical properties was to leave the crystal exposed to air for a number of days. The difference in mechanical properties that was caused by a thin organic layer was the original inspiration for controlled surface modifications. When our samples were exposed to air they did not display the variability in hardness reported by previous investigators [5], but did show a significant change in yield behavior. The average yield load was increased by almost 32% simply by leaving the crystal out for six days.

This indicated that subtle surface changes could dramatically influence mechanical property measurements. Ex-situ electrochemical modifications enabled very controlled and subtle changes to a gold surface. We performed two experiments with different layers added to a gold surface. In each case initial indentations were done on a freshly cleaned gold surface. In one of the tests we grew a gold oxide layer on the surface. This layer was only a monolayer of oxide as evident by the total change in current density during the reaction. The oxide layer had a significant influence on both the yield load and the overall hardness. The maximum applied shear stress at yield was increased by nearly 52%. The hardness was increased by over 26%. This is a substantial difference for such a thin layer. The gold crystal was placed back in the electrochemical cell and the oxide was stripped and the crystal mechanically tested again. The load at yield was reduced by 43% and the hardness was reduced by 14%. The removal of the oxide layer returned the mechanical properties to values very similar to the plain gold surface. This further validates that the oxide layer was the cause of the significant change in mechanical property values.

A lead monolayer was also added to the gold surface. Gold and lead are a special combination of elements because they experience a phenomenon called under potential deposition. This is when lead ions in the electrolyte deposit on the surface of the gold working electrode at a potential that is above bulk deposition. This means that it is energetically favorable for the lead to cover the gold surface, but the applied potential is not sufficient for lead to deposit on itself. This means that only a single monolayer can be deposited. Mechanical testing inside an electrochemical cell was not possible because of the lack of an appropriate tip. The crystal had to be removed from the cell in order to be tested. Lead oxidizes in air, which means we were testing the influence of a lead oxide monolayer. The lead oxide layer increased the maximum shear stress at yield by 25% compared to measurements on a freshly cleaned gold surface. The hardness was also increased by over 24%. This is a considerable difference in deformation behavior caused by a very thin surface layer.

Often in nanoindentation literature experimentalists say that they have ignored the oxide or surface layer because it is so thin compared to the depth of indentation. It is surprising that layers < 0.5 nm in thickness would have such a dramatic influence on indentation tests at least 35 nm deep. The difference in dimension is nearly two orders of

magnitude, and yet the influence of the surface layer is dramatic. This behavior for comparable scaled films is not observed in microindentation testing. The dramatic influence of a single monolayer is an intriguing and powerful result unique to this scale. This demonstrates that just because a layer is thin it should not be ignored for its contribution to deformation behavior may be significant. This indicates that the mechanical properties of a material can be changed, and potentially tailored by small controlled deposits.

While we still have not identified the root cause of the variation initially observed, we have learned that such behavior only happens in certain circumstances which are difficult to define. If the material does behave in a consistent manner, small contact area changes are observable. Deposited monolayers have a significant influence on measured hardness. The dimensions of these dynamic tests create significant inherent complexity. Deformation mechanism can be discrete and not continuous. Dominant factors at this scale are not usually observable on the macroscale. In this mesoscopic regime there are significant influences from factors usually overlooked and interactions that are difficult to predict. As we continue to strive for smaller products, we must continue to tackle the questions of unknown mechanisms involved with material behavior.

REFERENCES

1. Bhushan, B., *Nanomechanical Properties of Solid Surfaces and Thin Films*, in *Handbook of Micro/Nano Tribology*, B. Bhushan, Editor. 1995, CRC Press, Inc.: Boca Raton, FL. p. 321-396.
2. Tabor, D., *The Hardness of Metals*. 1951, New York, NY: Oxford University Press. 175.
3. Lysaght, V.E., *Indentation Hardness Testing*. 1949, New York, NY: Reinhold Publishing Corp. 288.
4. Bahr, D.F., et al., *Yield Point Phenomena During Indentation*. *Mat. Res. Soc. Symp. Proc.*, 1998. **522**: p. 83-88.
5. Corcoran, S.G., et al., *Anomalous Plastic Deformation at Surfaces: Nanoindentation of Gold Single Crystals*. *Phys. Rev. B*, 1997. **55**(24): p. R16 057-060.
6. Kiely, J.D., Houston, J.E., *Nanomechanical properties of Au (111), (001), and (110) surfaces*. *Phys. Rev. B*, 1998. **57**(19): p. 12588.
7. Hay, J.C. and G.M. Pharr, *Experimental Investigations of the Sneddon Solution and an Improved Solution for the Analysis of Nanoindentation Data*. *Mat. Res. Soc. Symp. Proc.*, 1998. **522**: p. 39-44.
8. Johnson, K.L., K. Kendall, and A.D. Roberts, *Surface Energy and the Contact of Elastic Solids*. *Proc. R. Soc. Lond.*, 1971. **324**: p. 301-313.
9. Pharr, G.M. and W.C. Oliver, *Nanoindentation of Silver-Relations Between Hardness and Dislocation Structure*. *J. Mat. Res.*, 1989. **4**(1): p. 94-101.
10. Robertson, C.F. and M.C. Fivel, *A Study of the Submicron Indent-Induced Plastic Deformation*. *J. Mat. Res.*, 1999. **14**(6): p. 2251-2258.
11. Fivel, M.C., et al., *Three-Dimensional Modeling of Indent-Induced Plastic Zone at a Mesoscale*. *Acta mater.*, 1998. **46**(17): p. 6183-6194.
12. Grosskreutz, J.C., *Mechanical Properties of Metal oxide films*. *J. Electrochem. Soc.*, 1969. **116**(9): p. 1232-1237.
13. Westwood, A.R.C., Preece, C. M., and Goldheim, D. L., *Molecular Processes on Solid Surfaces*. 1968, New York: McGraw-Hill. 591-610.
14. Tambwe, M.F., Stone, D.S., Hirvonen, J.P., *Scripta Materialia*, 1997. **37**(9): p. 1421.
15. Corcoran, S.G., *Nanoindentation of Atomically Modified Surfaces*. *Materials Research Society Symposium Proceedings*, 1998. **505**: p. 77.
16. Johnson, K.J., *Contact Mechanics*. 1987: Cambridge University Press.
17. Hertz, H., *On contact of elastic solids*. *J. Reine Angew. Math.*, 1881. **92**: p. 156-171.
18. Boussinesq, J., *Application des Potentials a l'etude de l'equilibre et du mouvement des solides elastiques*. 1885, Paris: Gauthier-Villars.
19. Timoshenko, S.a.G., J. N., *Theory of Elasticity*. 1951, New York: McGraw-Mill.
20. Fischer-Cripps, A.C., *Nanoindentation*. First ed. *Mechanical Engineering Series*, ed. F.F. Ling. 2002, New York, NY: Springer-Verlag. 197.

21. Love, A.E.H., *Stress produced in a semi-infinite solid by pressure on part of the boundary*. Phil. Tans. Royal Society, 1929. **A228**: p. 377.
22. Hull, D. and D.J. Bacon, *Introduction to Dislocations*. third ed. International Series on Materials Science and Technology. Vol. 37. 1984, Boston: Butterworth Heinemann.
23. Hirth, J.P.a.L., *Theory of Dislocations*. 1930, New York: John Wiley & Sons.
24. Gane, N.a.B., F.P., J. Appl. Phys., 1968. **39**: p. 1432.
25. Baker, S.P. and N. Burnham. *Measuring Mechanical Properties in the Nanometer Range*. in *Materials Research Society - Tutorial*. 2000. Boston.
26. Tabor, S.a., *Elastic recovery of conical indentations*. Phys. Proc. Soc., 1961. **78(2)**: p. 169-179.
27. Armstrong and Robinson, *Combined elastic and plastic deformation behaviour from a continuous indentation hardness test*. New Zeland Journal of Science, 1974. **17**: p. 429-433.
28. Howes, L.a., *Elastic recovery at hardness indentations*. J. Mat. Sci., 1981. **16**: p. 2745-2752.
29. Bulychev, et al., *Determining Young's modulus from the indenter penetration diagram*., Zavod. Lab, 1975. **41**: p. 11137-11140.
30. Doerner, M.F., and Nix, W.D., J. Mat. Res., 1986. **1(4)**: p. 601.
31. Field, J.S., Swain, J. Mat. Res., 1992. **8(2)**: p. 297-306.
32. Fischer-Cripps, A.C., J. Mat. Res., 1993. **16(6)**: p. 1579-84.
33. Sneddon, I.N., Int. J. Engin. Sci., 1965. **3**: p. 47.
34. Oliver, W.C. and G.M. Pharr, *An improved technique for determining hardness and elastic modulus using load and displacement sensing indentation experiments*. J. Mater. Res., 1992. **7(6)**: p. 1564-1583.
35. *Triboscope Nanomechanical Test System User's Manual*, ed. H. Inc. 1996, Minneapolis, MN.
36. Pharr, G.M., Oliver, W. C., Brotzen, F.R., J. Mat. Res., 1992. **7**: p. 613.
37. Bolshakov, A. and G.M. Pharr, *Influence of Pileup on the Measurement of Mechanical Properties by Load and Depth Sensing Indentation Techniques*. 13, 1998. **4(1049-1058)**.
38. Tsui, T.Y., C.A. Ross, and G.M. Pharr, *Nanoindentation Hardness of Soft Films on Hard Substrates: Effects of the Substrate*. Mat. Res. Soc. Symp. Proc., 1997. **473**: p. 57-62.
39. Tayebi, N., A.A. Polycarpou, and T.F. Conry, *Effects of the substrate on the determination of hardness of thin films by the nanoscratch and nanoindentation techniques: A comparative study for the case of soft film on hard substrate and hard film on soft substrate*. Mat. Res. Soc. Symp. Proc., 2004. **In Press**.
40. Greenwood, J.A., Williamson, J.B.P., *Contact of Nominally Flat Surfaces*. Proc. R. Soc. Lond., 1966. **295(1442)**: p. 300-319.
41. Bobji, M.S., S.K. Biswas, and J.B. Pethica, *Effect of Roughness on the Measurement of Nanohardness- a Computer Simulation Study*. Appl. Phys. Lett., 1997. **71(8)**: p. 1059-1061.
42. Bobji, M.S. and S.K. Biswas, *Estimation of Hardness by Nanoindentation of Rough Surfaces*. J. Mat. Res., 1998. **13(11)**: p. 3227-3233.

43. Kiely, J.D., Bonnell, D. A., *Quantification of topographic structure by scanning probe microscopy*. J. Vac. Sci. Technol. B, 1997. **15**(4): p. 1483-1493.
44. Thomas, R.C., et al., *The Mechanical Response of Gold Substrates Passivated by Self-Assembling Monolayer Films*. Science, 2002. **259**(5103): p. 1883-1885.
45. Fuller, K.N.G. and D. Tabor, Proc. R. Soc. Lond., 1975. **345**: p. 327.
46. Maugis, D. and H.M. Pollock, Acta Metall. Mater., 1984. **32**: p. 1232.
47. Beake, B.D. and J.F. Smith, *High-temperature nanoindentation testing of fused silica and other materials*. Phil. Mag. A, 2002. **82**(10): p. 2179-2186.
48. Suresh, S., T.-G. Nieh, and B.W. Choi, Scripta Materialia, 1999. **41**(9): p. 951.
49. Gouldstone, A., et al., *Discrete and Continuous Deformation During Nanoindentation of thin Films*. Acta mater., 2000. **48**: p. 2277-2295.
50. Bahr, D.F., et al., J. Mat. Res., 1997. **12**(12): p. 3345.
51. Domnich, V., Y. Gogotsi, and S. Dub, Appl. Phys. Lett., 2000. **76**(16): p. 2214.
52. Domnich, V., Y. Gogotsi, and H.D. Hochheimer, NATO Sci. Series. II Math., 2001. **48**: p. 291.
53. Mann, A.B. and J.B. Pethica, *The role of atomic size asperities in the mechanical deformation of nanocontacts*. Appl. Phys. Lett., 1996. **69**(7): p. 907-909.
54. Page, T.F., W.C. Oliver, and C.J. McHargue, *The deformation behavior of ceramic crystals subjected to very low load (nano)indentations*. J. Mater. Res., 1992. **7**(2): p. 450-473.
55. Tromas, C., et al., *Study of the Low Stress Plasticity in Single-Crystal MgO by Nanoindentation and Atomic Force Microscopy*. J. Mat. Sci., 1999. **34**: p. 5337-5342.
56. Venkataraman, S.K., D.L. Kohlstedt, and W.W. Gerberich, J. Mat. Res., 1993. **8**(4): p. 685.
57. Gerberich, W.W., et al., Acta Metall. Mater., 1995. **43**(4): p. 1569.
58. Tangyunyong, P., et al., Phys. Rev. Letters, 1993. **71**(20): p. 3319.
59. Pethica, J.B., R. Hutchings, and W.C. Oliver, Phil. Mag. A, 1983. **48**: p. 593.
60. Bahr, D.F., D.E. Wilson, and D.A. Crowson, J. Mat. Res., 1999. **14**(6): p. 2269.
61. Asif, S. and J.B. Pethica, Phil. Mag. A, 1997. **76**: p. 1105.
62. Mann, A.B. and J.B. Pethica, *The effect of tip momentum on the contact stiffness and yielding during nanoindentation testing*. Philosophical Magazine A, 1999. **79**(3): p. 577-592.
63. Thomas, R.C., et al., Science, 1993. **259**: p. 1883.
64. Kiely, J.D. and J.E. Houston, *Indentation Modulus and Yield Point of Au (111), (001), and (110)*. Mat. Res. Soc. Symp. Proc., 1998. **522**: p. 125-131.
65. Kelchner, C.L., S.J. Plimpton, and J.C. Hamilton, *Dislocation Nucleation and Defect Structure During Surface Indentation*. Phys. Rev. B, 1998. **58**(17): p. 11085 - 11088.
66. Rodriguez de la Fuente, O., et al., *Dislocation Emission around Nanoindentations on a (001) fcc Metal Surface Studied by Scanning Tunneling Microscopy and Atomistic Simulations*. Phys. Rev. Letters, 2002. **88**(3): p. 6101.
67. Li, J., et al., *Atomic mechanisms governing elastic limit and incipient plasticity in crystals*. Nature, 2002. **418**: p. 307.

68. Lilleodden, E.T., et al., *Atomistic simulations of elastic deformation and dislocation nucleation during nanoindentation*. Journal of Mechanics and Physics of Solids, 2003. **51**: p. 901-920.
69. Lilleodden, E.T. and W.D. Nix, *A nanoindentation study of microstructural length-scale effects in gold thin films*. Phys. Rev. B, 2002.
70. Feichtinger, D., et al., *Atomistic simulations of spherical indentations in nanocrystalline gold*. Phys. Rev. B, 2003. **67**: p.4113
71. Kiely, J.D., R.Q. Hwang, and J.E. Houston, *Effect of Surface Steps on the Plastic Threshold in Nanoindentation*. Phys. Rev. Letters, 1998. **81**(20): p. 4424-4427.
72. Zimmerman, J.A., et al., *Surface Step Effects on Nanoindentation*. Phys. Rev. Letters, 2001. **87**(16): p. 165507-1 - 4.
73. Angerstein-Kozłowska, H., et al., *Elementary Steps of Electrochemical Oxidation of Single Crystal Planes of Au : Part 2 A Chemical and Structural Basis of Oxidation of the (111) Plane*. J. Electroanal.Chem., 1987. **228**: p. 429-453.
74. Reddy, A.K.N., M.A. Greshaw, and J.O.M. Bockris, J. Chem. Phys., 1969. **48**: p. 671.
75. Angerstein-Kozłowska, H., B.E. Conway, and W.B. Sharp, J. Electroanal. Chem., 1973. **43**: p. 9.
76. Cullity, B.D., *Elements of X-Ray Diffraction*. 1956, Reading: Addison-Wesley.
77. Kolb, D.M., *Physical and Electrochemical Properties of Metal Monolayers on Metallic Substrates*, in *Advances in Electrochemistry and Electrochemical Engineering*. 1978, John Wiley & Sons: New York, New York. p. 125-271.
78. Corcoran, S.G., *In Situ STM of Electrodeposition Processes*, in *Materials Science and Engineering*. 1994, Johns Hopkins University: Baltimore, MD.
79. Juttner, K. and W.J. Lorenz, *Underpotential Metal Deposition on Single Crystal Surfaces*. Zeitschrift für Physikalische Chemie Neue Folge, 1980. **122**: p. 163-185.
80. Corcoran, S.G., *Structures Class Notes*. 2003.
81. Gerberich, W.W., et al., *Indentation Induced Dislocation Nucleation: The Initial Yield Point*. Acta mater., 1996. **44**(9): p. 3585-3598.
82. Kunert, M., *Mechanical properties on nanometer scale and their relations to composition and microstructure*, 2000, Fakultät Chemie der Universität Stuttgart, Stuttgart, Germany.
83. Reed-Hill, R.E. and R. Abbaschian, *Physical Metallurgy Principles*. 1973, Boston, MA.
84. Askill, J., *Trace Diffusion Data for Metals, Alloys, and simple Oxides*. 1970, New York: Plenum.
85. Easterling and Porter, *Phase Transformations in Metals and Alloys*, 2003, Boca Raton Fl, CRC Press.
86. Cottrell, A.H., Phil. Mag., 1961. **6**, p. 1351
87. Black, L., Allen, G. C., *Nature of Lead Patination*, British Corrosion Journal, 1999. **34**(3): p. 192-197

VITA

Martha Mary McCann was born June 4, 1975 in Boston, MA. She grew-up in Belmont, MA, where she attended Belmont High School. After graduation in 1993, she entered the Johns Hopkins University. She received a Bachelor of Science degree in Materials Science and Engineer in May of 1997. After graduation she moved to Seattle WA, where she worked for the Boeing Company on a developmental aircraft called the High Speed Civil Transport. She worked in Manufacturing Research and Development, investigating the feasibility of implementing existing composite manufacturing methods on highly specialized polymer matrix materials. In the fall of 1999 she began graduate school at Virginia Polytechnic and State University. In December of 2001 she earned her Masters of Engineering from the Materials Science and Engineering department. During her time at Virginia Tech, Ms. McCann founded the University Chapter for the Materials Research Society.